SESSION

MEDICAL DEVICES AND SUPPORTING SYSTEMS

Chair(s)

TBA

Evaluation of Embedded ISAs for Smart Cardiac Pacemaker Workloads

Safwat Mostafa Noor and **Eugene John**
Department of Electrical and Computer Engineering, University of Texas at San Antonio
San Antonio, Texas

Abstract - *Embedding microprocessors in implantable cardiac pacemakers for analyzing data and executing pre-programmed behavior has always been a challenging task where achieving a suitable balance between power and performance is the main focus. The upcoming generation of pacemakers is expected to both diversify the processor workload and demand significantly increased computational capabilities. This paper investigates potential workloads for future cardiac pacemakers and evaluates the key challenges in the path of development. Relevant benchmark programs including heart signal processing, physical activity detection, security via encryption and cyclic redundancy check are simulated on commercial embedded processors for performance-power analysis. An insight into the appropriateness of current processors is achieved and key Instruction Set Architecture features that achieve benefit in the realm of pacemaker applications are identified. Correlations between instruction-mix and power consumption are visualized for different workloads. The simulation results are analyzed to understand requirements of implantable processors for future smart pacemakers.*

Keywords: Pacemaker, Smart Pacemaker, Implantable Processor, ImplantBench, ARM

1 Introduction

In the past few years commercial and consumer electronics has gone through vast changes due to the advent of embedded processors and ubiquitous mobile wireless connectivity [1]. It has become a trend to integrate smart computing capabilities into electronic devices, wherever it is deemed feasible. Not only has this revolutionized the way people connect with each other but it has also created a path for people to interact with the devices they own. This new realm of connectivity has immense potential for integration into biomedical or implantable electronics [2]. Examples of such approaches can already be seen on recent wearable monitoring devices such heart rate sensors or pedometers. However, to integrate the concept of smart computing and connectivity into critical application such as pacemakers requires higher degrees of security, combined with extreme power efficiency and reliability. This paper is intended to provide an insight into possible application workloads expected in next generation of secured smart pacemakers and evaluate the computational performance of current commercial embedded processor for such applications, including their power consumption analysis. The experiments conducted in this research helps to bring forward the desirable features in processor architectures that can benefit the development of future smart pacemakers.

The use of pacemakers has increased 55.6% between the years 1993 to 2009 with approximately 2.9 million patients receiving a pacemaker implant [3]. They are proven to be an effective and highly reliable treatment to complex heart conditions such as arrhythmia. Not many years ago, the functionality of a pacemaker was mostly limited to monitoring signals from the heart and assisting its operation via artificial pacing when any predefined abnormality was detected. In the recent years manufacturers started incorporating advance features to make the pacemaker smarter and more user-friendly [4]. These improvements not only include the refinement of the fundamental sensing and pacing procedure, but also adds convenient features such as data logging and configuration via wireless telemetry. Future smart pacemakers are expected to communicate seamlessly with the patient's smart-phone or integrate easily into a hospitals wireless network infrastructure. This is still not efficiently feasible using current pacemaker technology and can introduces serious security risks [5], [6]. In the mentioned future use cases, the pacemaker can be configured to automatically transmit alerts via the connected smart-phone or wireless network when life critical situations occur. Operational data can logged and viewed on the patient's smart-phone for easy monitoring. The possibilities depend on the innovativeness of the developer, given that a suitable and efficient programmable computing platform is provided to implement the required software stacks and security features. The major obstacle for realizing this goal is the limited computational ability available on processors used in pacemakers. The manufacturers are also often inclined towards ASIC based design for carrying out the demanding computation workloads. While choosing the ASIC approach provides the lowest power and highest performance for the application at hand, it does not provide freedom to the firmware developer for expanding its feature set. The solution to this situation lies in the development of application specific instruction-set processors (ASIP) or System on Chips (SoCs) that are able to provide adequate computational capability while adhering to the low power requirements; ensuring the flexibility needed for next generation pacemakers.

2 Background Study

The human heart consists of special conduction fibers and two primary nodes that make up its native pace-making system. The *Sinoatrial Node (SA Node)* acts to distribute electric impulses through the *Bachmann's Bundle* fibers and

the *Atrioventricular Node (A-V Node)* introduces an important synchronizing delay before distributing the impulses to the *Bundle branch* and *Purkinje fibers* [Figure.1]. The SA node and AV nodes are connected via *Internodal tracks* and the delay of the signal travelling from the SA node to the A-V node ensures the synchronization between the contraction/depolarization of the Atria and Ventricle chambers [7]. The movement of the chambers are driven by *myocardium muscles* and require a certain period of the impulse to fully activate. The impulses are often called action potentials. Described simply, the periodic pacing procedure of the heart is a synchronized flow of electric impulses through the conduction fibers followed by the contraction of the muscles. The whole process depends largely on the correct behavior of SA and A-V nodes.

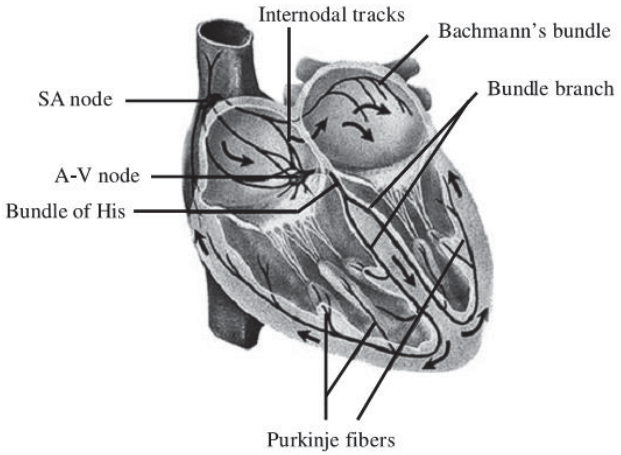

Figure.1. The Conduction System of the Heart [8]

Common cardiac diseases such as Arrhythmias are mainly caused by cardiac conduction problems resulting in abnormal heart rhythms. The hearts natural pacemaker may develop damaged conduction paths, blocked A-V node or failure to generate impulse. The artificial demand pacemaker monitors the impulses of the heart via Intracardiac electrogram (IECG) and determines the requirement of artificial pacing. Many modern rate responsive pacemakers take into account multiple other factors such as the activity level of the patient, body temperature, pH level of the blood etc. when sensing the heart signals to better regulate the artificial pacing in accordance with the patient's physical situation. The signal processing required in these operations involves FFT calculation of the ECG data and algorithms for pattern matching [10]. ASIC designs [11] are often the preferred implementations for processing these workloads as they run continuously during the pacemaker's operation lifetime. Although there have been attempts to use simpler 8-bit or 16-bit low power microcontrollers in the place of ASIC solutions [12] [13], these processors are expected to be overwhelmed by complex encryption workloads. Three workloads representing ECG signal processing, Activity detection and Heart pacing monitoring are included in the hardware performance analysis performed in this paper. The results serve as a feasibility study for using a 32-bit embedded processor for performing monitoring tasks.

The challenges in enabling wireless connectivity in critical implantable devices originate mainly in the form of security and power consumption. Security in Cardiac pacemakers with wireless connectivity is particularly important as the outcome of any security breach can be used to trigger lethal life threating attacks. Examples of such security compromises and risks have come up both in research [5] and in real life scenarios [6]. Better security requires stronger data encryption schemes which in turns translate to higher computational load and higher power consumption. In the current embedded industry, security protocols and standards such as WEP (IEEE Standard 802.11), Advanced Encryption Standard (AES), Internet Protocol Security (IPSec) and Secure Sockets Layer (SSL) are regularly used to secure the data services and transmission. While security protocols and cryptographic algorithms address security considerations from a "functional" perspective, implantable systems are constrained by the environments they operate in, and by the resources they possess. The computational load for implementing industry standard security protocols such as AES or SSL includes both cryptographic and non-cryptographic components [9]. Computational load is also contributed from the integrity checks such as Cyclic Redundancy Check (CRC), Message-Digest 5 (MD5) hash calculation that are involved in data transmission. Figure.2 shows a breakdown of SSL in percentage for a process of encryption and integrity check for varying size of data transaction.

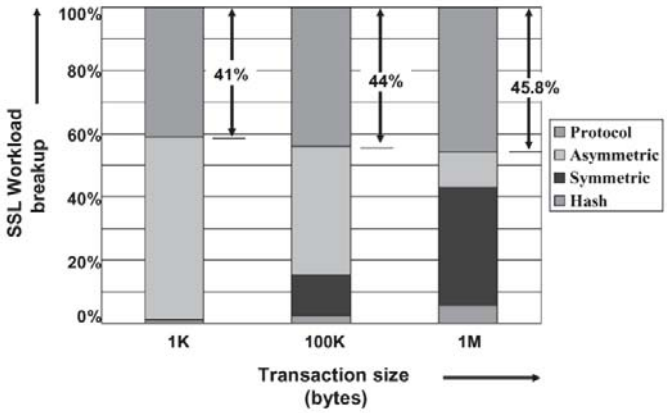

Figure.2. Breakup of SSL workload into cryptographic and non-cryptographic components [9]

It can be observed that the workload variation depends mostly on the data rate requirement of a certain encryption process. This indicates a need for a combined hardware and software based approach to deal with security in cardiac pacemakers. Further along in this paper we explore the hardware performance of encryption algorithms and data integrity calculations on embedded platforms.

The two Instruction Set Architecture (ISA) used for comparison are ARMv4 and the MIPS like PISA (Portable ISA) provided with SimpleScalar architectural simulator [14]. Since the PISA essentially implements a modern MIPS architecture; the simulation results will effectively compare the ARM and MIPS ISA. The ARM architecture is currently one of the most

popular embedded architectures and has ubiquitous use in many different fields. It is typically a 32 bit RISC machine with a Von Neumann architecture and was first developed in 1980 by Acron Computers. The ISA currently has multiple micro-architectures ranging from real time high performance implementations to low power microcontroller solutions [15]. The MIPS ISA was developed in 1981 by MIPS Computer Systems. The version used in this research is largely similar to the MIPS1 ISA which is the 32 bit version with a Floating Point (FP) unit [14]. The benchmarks were selected from Implantbench [16] which was released in 2008 by A. Cheng in the hope of enabling implantable nano-scale computing ImplantBench is the only major benchmark suite that provides the required set of programs to simulate and study future implantable devices. Although ImplantBench has been used for multiple different research [17], [18] focusing on benchmark analysis, actual analysis of the programs running on real world hardware models are not abundant.

3 Research Description

We utilize architectural simulations to generate statistics on performance for executing workloads of a smart pacemaker. Table I shows the simulation configurations that were used.

TABLE I
Configuration for simulation

ARM Processor	MIPS Processor
ARMv4 Architecture	MIPS-I Architecture
ARM ISA	MIPS32 ISA
Dual-issue, out-of-order, 7 stage pipeline 16KB i-cache and d-cache 4 way associative	dual-issue, out-of-order, 5 stage pipeline 16KB i-cache and d-cache 4 way associative
Single Hardware Thread	Single Hardware Thread
100MhZ at 1.1V	100MhZ at 1.1V

Supporting components such as cache, NoCs and memory systems were included in the simulation. However, the study tries to focus mostly on the performance of the pipeline and the components that are closely related to it. Therefore performance of NoCs and memory systems are taken out of the discussion and statistics originating only from the Out Of Order (O3) pipeline and cache are discussed in most detail. We explore three major types of workloads using five different benchmarks from ImplantBench. The Five benchmark programs represents Heartbeat monitoring, Physical activity monitoring, Security (Encryption), and Redundancy (CRC). The selected programs and adopted method for simulation are discussed in the next section.

3.1 Benchmark and Methodology

ImplantBench includes dedicated programs for heart activity and physiological monitoring as well as CRC and encryption.

A. Heart Activity and Physiology

The three selected benchmarks in this category are “Activity”, “AFVP”, and “ECGSYN”. Modern pacemakers allows for variable pacing schemes based on the patients physical activity level. The Activity [19] benchmark is such a program that uses mean heart rate data to derive an activity index that reflect the level of physical activity of the patient. The primary task of a pacemaker is to sense electric signal in one or more heart chamber and follow the pre-configured scheme for pacing. The AFVP [20] (Atrial Fibrillation and Ventricular Pacing) benchmark provides a realistic ventricular rhythm model of atrial fibrillation (AF), generating a synthesized beat-to-beat interval sequence of ventricular excitations with a realistic structure. Finally, the ECGSYN [21] program generates a synthesized ECG signal from a few user configurable parameters like mean heart rate, beat count, duration of P,Q,R,S, and T waves etc. This ECG model allows reproduction of many features of the human ECG such as respiratory sinus arrhythmia, QT dependency on heart rate and R-peak amplitude modulation.

B. Reliability (CRC)

CRC [22] is a simple hash function that detects errors in data streams. The CRC benchmark in ImplantBench implements the CRC-CCIT algorithm which is a standard for many communication mediums including telephone, Bluetooth etc. CRC calculations are commonly used in reliably storing and retrieving and also to ensure error free transmission of data.

C. Security (Encryption - khazad)

Future pacemakers will have streamlined wireless communication with external monitoring devices. This requires stringent encryption and security requirement, mostly due the dangers involved in a pacemaker hack [5]. Current day pacemakers which rely on a proprietary protocols and weak encryption schemes are susceptible to intrusion and can turn fatal. Industry standard encryption schemes can provide robust security that can be simulated via the khazad [23] program. Khazad implements an iterated 64-bit block cipher using 128-bit keys. The algorithm is similar to that of the more popular AES encryption and can represent similar workloads for the target.

The SimpleScalar tool set [14] is an infrastructure for modeling microprocessor architecture and simulating application performance. SimpleScalar has support for Alpha, PISA, ARM and x86 instructions. The ARM implementation includes an out-of-order pipeline used in Intel's StrongARM SA-11xx series processors which runs ARMv4 instruction set. The simulator is able to provide up to 96% accuracy compared to real hardware. The PISA instruction set is a simple MIPS-like ISA with more addressing modes and no delay slots. Similar to ARM the ISA has both little and big endian support to match host endianness. The benchmarks where compiled with optimization turned off and were executed with the default data set attached with the benchmarking suit.

McPAT [24] is an integrated power area and timing simulation tool. Although it was originally created for simulating multicore architectures, it does allow flexible configuration and can be made to simulate single core architectures. The technology node and operating voltage can be configured and was set to a 45nm 1.1V process.

4 Results and Analysis

The first part of the analysis is based on the instruction profiling data extracted from SimpleScalar and the second part looks at performance statistics and power consumption data from McPAT. The instruction profile of the benchmarks is a good starting point for examining the differences generated due to the ISA. Figure.3. (a) (b) shows the instruction mix for ARM and MIPS. Almost all benchmarks exhibit noticeable difference in their instruction footprint between the two platforms. This is summarized in Figure.3. (c) as a plot of the difference in percentage of major instruction types in MIPS with reference to ARM.

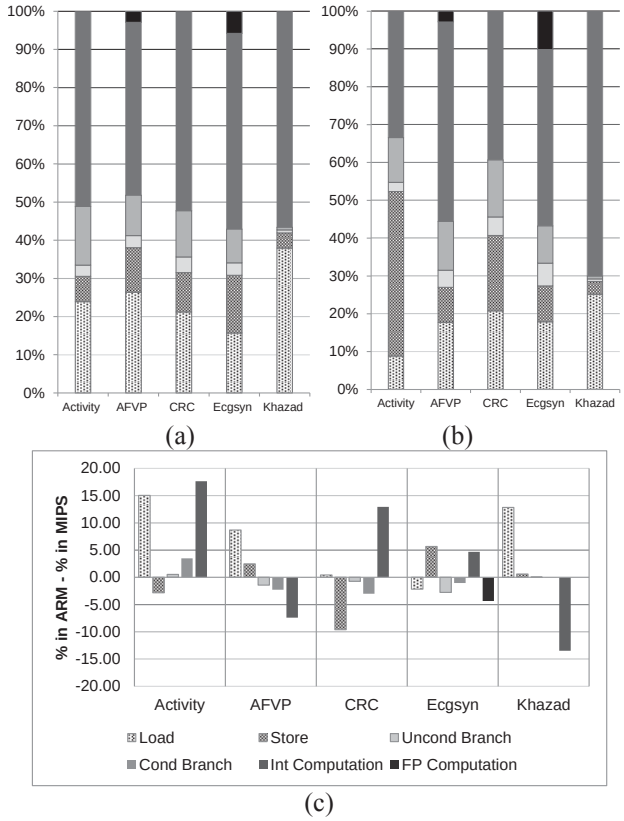

Figure.3. (a) Instruction mix for ARM, (b) Instruction mix for MIPS. (c) Difference in % of instruction type

Prominent differences are seen in the Load, Store and Integer computation categories across all benchmarks. The ARM compiler consistently uses a higher number of Load instructions in Activity, AFVP and Khazad. Initial speculations point towards the lower physical register count in the ARM as an explanation to this phenomenon. The ARM compiler only has 16 general purpose registers to work with and therefore is forced to use more load instructions. Other noticeable differences occur in the Instruction Count for integer computation in Activity, CRC and Khazad and STORE instructions count in CRC and Ecgsyn. These dissimilarities in instruction mix are expected to reflect their effect in the simulated performance statistics and power calculation. The performance statistics results are generated from the out-of-order simulator provides a detailed summary that list various access counts and rates for all the components of the simulated processor. Figure.4. shows the Instruction Per Cycle (IPC) on the two platforms. The ARM architecture leads in all but the Khazad benchmark. A negative correlation is observed between IPC

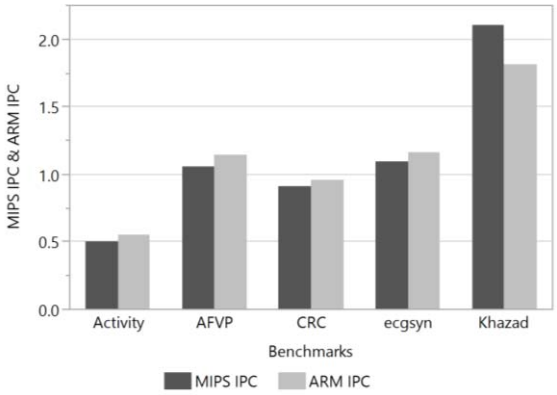

Figure.4. IPC comparison for five benchmarks

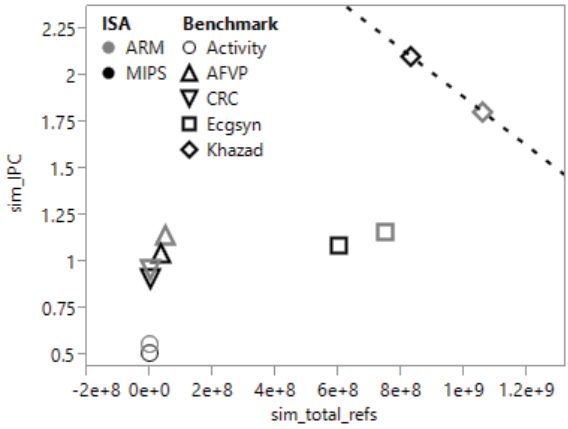

Figure.5. Correlation between IPC and memory reference.

and cumulative LOAD/STORE access count in Figure.5. This can be anticipated by analyzing Figure.3. (a) where the khazad is seen to have the highest number of load instructions on ARM. The khazad benchmark and many other encryption benchmarks are likely to exhibit the requirement of higher load operation due to the existence of a cipher key that needs to be repetitively loaded and used in the encryption algorithm [25]. These are considered non-cryptographic part of the algorithm and are directly proportional with the data rate of the encryption process. Therefore, an ISA with higher general purpose registers is likely to provide better performance for this purpose. However, the effect of having a larger register file will also affect the power consumption of the pipeline execution unit, requiring a tradeoff between performance and

power. Figure.6. shows the energy consumption of the major components of the pipeline computed by McPAT.

The execution unit consumes the most energy among other pipeline components. Interestingly, better IPC performance in ARM does not consistently result back to better energy efficiency. The execution unit of ARM must cater for conditional execution and operand shifting and the hardware for implementing these features contributes to the energy envelope even if they are not utilized in a given program. The overall energy consumption for executing Ecgsyn and AFVP benchmarks are in the same order of magnitude as that of the encryption benchmarks, indicating that the use of 32-bit general purpose processors for heart signal monitoring is not a feasible solution in the context of cardiac pacemakers. Energy required (400 mJ to 6.5 J) by these two benchmarks also indicate towards the need for ASIC or coprocessor based approaches. In the remaining benchmarks of interest, the MIPS (PISA) microarchitecture yields better results in power consumption mostly due to a simpler ISA design and higher register count. The overall energy consumption of the workloads range from sub mJ to a maximum of 8J. The power budget of a typical pacemakers is limited to 1.2 Ah [26], [27] which would need a significantly lower average consumption throughout the workloads to last 7-10 years of expected lifetime. Achieving such numbers without the use of dedicated coprocessor is unlikely and the experimental results here shows the magnitude of the improvement that is required in this field.

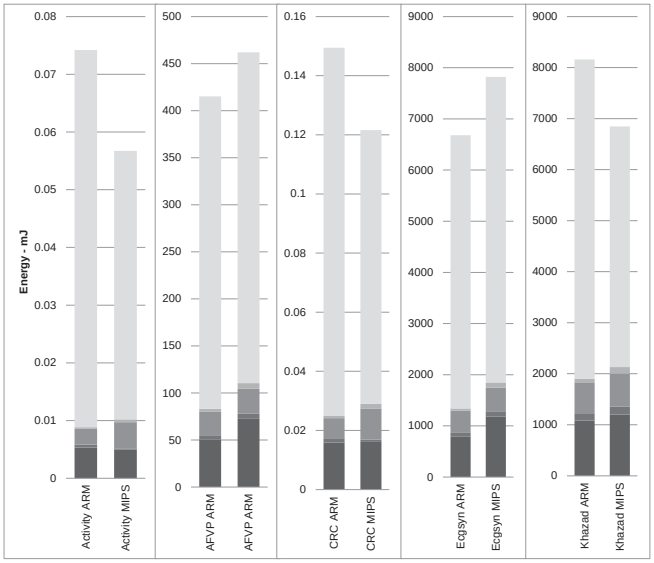

Figure.6. Energy consumption breakdown

5 Conclusions

The analysis of different workloads and their impact through the internals of a commercial embedded processor portray the various factors that can contribute to the power consumption scenario. The results obtained from the comparison of two ISAs point towards the development of Application Specific Instruction-set Processors (ASIP) for achieving low power operation while providing functionalities of the future cardiac pacemaker. Primary requirements for such an ISA and microarchitecture can be identified from the study conducted in this paper. Cardiac pacemaker tasks such as encryption and heart rate monitoring benefits from higher register count and the circuitry for instruction fetch unit needs to be power efficient for longer battery life. The nature of the cardiac pacemaker programs are heavily repetitive, therefore, the instructions for program flow control should not introduce integer/logical computations in the execution unit and have dedicated execution elements. The effects of such implementation are visible in the ARM ISA which includes conditional execution bits for most instructions. Due to this feature, all of the benchmarks exhibit generally low integer computational load in the ARM platform, which is desirable. Lastly, the IPC and power consumption analysis presented in this research helps to target tasks such as AFVP and Khazad that can benefit from both ASIP and the development of specific or generic calculation coprocessor.

6 Acknowledgement

Research reported in this paper was supported in part by National Institute of General Medical Sciences of the National Institutes of Health under award number 1SC3GM096937-01A1. The content is solely the responsibility of the authors and does not necessarily represent the official views of the National Institutes of Health

7 References

[1] ABI Research, "Over 5 Billion Wireless Connectivity Chips Will Ship in 2013," [Online]. Available: http://www.businesswire.com/news/home/20121221005461/en/5-Billion-Wireless-Connectivity-Chips-Ship-2013

[2] E. Jovanov and A. Milenkovic, "Body Area Networks for ubiquitous healthcare applications: opportunities and challenges.," *J. Med. Syst.*, vol. 35, no. 5, pp. 1245–54, Oct. 2011.

[3] A. J. Greenspon et al., "Trends in permanent pacemaker implantation in the United States from 1993 to 2009: increasing complexity of patients and procedures." J. Am. Coll. Cardiol., vol. 60, no. 16, pp. 1540–5, Oct. 2012.

[4] ST. Jude Medical, "Pacemaker and ICD Developments Fact Sheet," 2011. [Online]. Available: http://www.sjm.com/ corporate/media-room/~/media/SJM/corporate/AboutUs/PDFs

[5] D. Halperin et al., "Pacemakers and Implantable Cardiac Defibrillators: Software Radio Attacks and Zero-Power Defenses," 2008 IEEE Symp. Secur. Priv. (sp 2008), pp. 129–142, May 2008.

[6] K. SEBELIUS, "One-on-One With Kathleen Sebelius; The Heart of Dick Cheney," October 27, 2013. [Online]. Available: http://edition.cnn.com/TRANSCRIPTS/1310/27/hcsg.01.html.

[7] A. C. Guyton and J. E. Hall, Textbook of Medical Physiology, 9th edn, W. B. Saunders, Toronto, January 1996.

[8] R. Sutton and I. Bourgeois, The Foundations of Cardiac Pacing. Part I, Futura Publishing Company, Mount Kisco, NY, 1991.
[9] S. Ravi, A. Raghunathan, P. Kocher, and S. Hattangady, "Security in Embedded Systems: Design Challenges," ACM Trans. Embed. Comput. Syst., vol. 3, no. 3, pp. 461–491, Aug. 2004.
[10] S. P. Haddad and W. Serdijn, "Wavelet versus Fourier Analysis," in Ultra Low-Power Biomedical Signal Processing SE - 3, Springer Netherlands, 2009, pp. 33–50.
[11] L.-F. Cheng, T.-C. Chen, and L.-G. Chen, "Architecture design of the multi-functional wavelet-based ECG microprocessor for realtime detection of abnormal cardiac events.," Conf. Proc. IEEE Eng. Med. Biol. Soc., vol. 2012, pp. 4466–9, Jan. 2012.
[12] L. Xu, H. Zhang, and K. Yao, "The analysis and design of diphasic pacemaker pulse system based on microcontroller," *Proc. 10th World Congr. Intell. Control Autom.*, pp. 1192–1195, Jul. 2012.
[13] S. Chede and K. Kulat, "Design Overview of Processor Based Implantable Pacemaker," vol. 3, no. 8, pp. 49–57, 2008.
[14] D. Burger, W. D. Street, and T. M. Austin, "The SimpleScalar Tool Set , Version 2 . 0," no. C, 1997.
[15] ARM, "Cortex-A Comparisons," 2013. [Online]. Available: http://www.arm.com/products/processors/cortex-a/.
[16] Z. Jin and A. C. Cheng, "ImplantBench: Characterizing and Projecting Representative Benchmarks for Emerging Bioimplantable Computing," IEEE Micro, vol. 28, no. 4, pp. 71–91, Jul. 2008.
[17] Z. Jin and A. C. Cheng, "Improve Simulation Efficiency Using Statistical Bench- mark Subsetting - An ImplantBench Case Study," pp. 970–973, 2000.
[18] K. Ganesan, J. Jo, and L. K. John, "Synthesizing memory-level parallelism aware miniature clones for SPEC CPU2006 and ImplantBench workloads," *2010 IEEE Int. Symp. Perform. Anal. Syst. Softw.*, pp. 33–44, Mar. 2010.
[19] G.B. Moody, ''ECG-Based Indices of Physical Activity,'' Computers in Cardiology, IEEE Press, 1992, pp. 403-406.
[20] J. Lian, D. Mussig, and V. Lang, ''Computer Modeling of Ventricular Rhythm During Atrial Fibrillation and Ventricular Pacing,'' IEEE Trans. Biomedical Engineering, vol. 53, no. 8, Aug. 2006, pp. 1512-1520.
[21] P.E. McSharry et al., ''A Dynamical Model for Generating Synthetic Electrocardiogram Signals, '' IEEE Trans. Biomedical Engineering, vol. 50, no. 3, Mar. 2003, pp. 289-294
[22] R.N. Williams, A Painless Guide to CRC Error Detection Algorithms, 1993. [Online]. Available: http://read.pudn. com/downloads137/doc/585979/crc-Ross.pdf
[23] P. Barreto and V. Rijmen, ''The Khazad Legacy-Level Block Cipher,'' 1st Open NESSIE Workshop 2000, pp. 13-14; https://www.cosic.esat.kuleuven.be/nessie/ workshop
[24] S. Li, "McPAT : An Integrated Power , Area , and Timing Modeling Framework for Multicore and Manycore Architectures," no. c, 2009
[25] B. Schneier, J. Kelsey, D. Whiting, D. Wagner, and C. Hall, "Performance Comparison of the AES Submissions Key Length Performance on 32-bit CPUs," 1999.
[26] ST. Jude Medical, "AccentTM Pacemaker Specs." April 19, 2013 [Online]. Available: http://professional.sjm.com/ products/crm/pacemakers/dual-and-single-chamber/ accent#overview.
[27] Medtronic. Inc, "Adapta With MVP Pacing System" September 22, 2010. [Online]. Available: http://www.medtronic.com/for-healthcare-professionals/products-therapies/cardiac-rhythm/pacemakers/adapta-with-mvp-pacing-system

A Recording System to Eavesdrop on Marmosets

C. Casebeer[1], E. Newlon[1], K. Callahan[1], C. Miller[2], and R.K. Snider[1]
[1]Electrical and Computer Engineering, Montana State University, Bozeman, MT, USA
[2]Department of Psychology, University of California, San Diego, CA, USA

Abstract - *A small light weight recording system is being developed to record vocalizations, spatial locations, and behaviorally related movements – the behavioral acoustic biome – in a wild social troop of marmosets. The system will enable data to be taken that will characterize communication networks in primates living in their natural habitat for the first time. The system will include microphones to record animal vocalizations and other external sounds, an inertial measurement unit (IMU) for local behaviorally related motion data, and a global positioning unit (GPS) to provide position data and absolute time. Data will be stored locally on a microSD flash card. The system is being designed in a modular fashion to allow sensors to be added for future data recording capabilities.*

Keywords: Recording System, Vocalizations, Behavioral Acoustic Biome

1 Introduction

This paper describes efforts underway to develop a collar mounted measurement system that will record vocalizations, spatial locations, and behaviorally related movements – *the behavioral acoustic biome* – in a wild social troop of marmosets. Animal behaviorists are interested in communication networks, which are likely fundamental to how vertebrate species convey meaningful information with conspecifics. Rather than communication being limited to vocal exchanges between dyads (the typical model of animal communication), pertinent information has been hypothesized to be communicated along several dimensions of ongoing interactions between multiple animals. Despite the potential significance of these multidimensional communication networks, there is little recorded data on the topic. Until recently, technological advances had not reached a point where developing a system capable of recording and quantifying communication networks in vertebrates was logistically feasible. However, due to the miniature electronic devices that have been developed for the smartphone industry, it is now feasible to develop such a system. The system that is being developed will record acoustic data from microphones, positional data from a GPS receiver, and local movements from a MEMS motion sensor, which will all be saved to a microSD flash card. It is envisioned that the system will be eventually extended with the capability to record auditory neural responses, allowing neuroscientists to study the primate auditory cortex in a natural behaving context.

2 Recording System Capabilities

2.1 System Overview

The collar system will collect sensor data from multiple integrated circuit and microelectromechanical system (MEMS) sensors and then store the data to a microSD flash card. The sensors include digital microphones to record animal vocalizations and other external sounds, an inertial measurement unit (IMU) for local behaviorally related motion data, and a global positioning unit (GPS) to provide position and absolute time data. The system is powered by a battery and is initially power limited. The system will need to recharge the battery via solar cells before any subsequent recordings can occur. As a result, the power usage of all parts of the system has been considered in their selection. One design choice that has a significant impact on the design and power consumption of the system has been the use of an FPGA and CPLD for the digital system controller. These devices were chosen for their development ease and flexibility, both for the current system as well as for future capabilities. We have made this design choice knowing we take a power hit doing so. For the current prototype system board we are testing, we have added power measurement capabilities for all active devices in the system. These will be removed in the final system board.

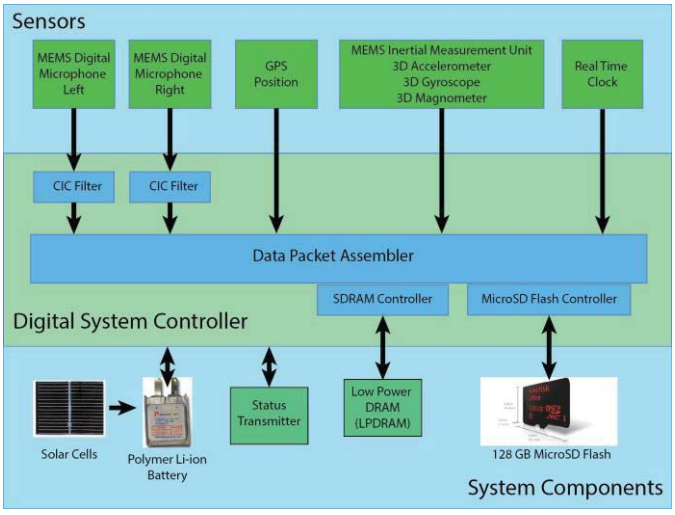

Figure 1. System Overview.

2.2 Field Programmable Gate Array and Complex Programmable Logic Device

Central to the design is an Altera Cyclone V Field Programmable Gate Array (FPGA) and a Max V Complex Programmable Logic Device (CPLD). A hardware description language (HDL), VHDL in this instance, is being used to define the embedded logic in the FPGA, which is comprised of interconnected logic elements. Logic elements are the basic building blocks of FPGAs and are typically implemented as small memories that act as functional lookup tables, which also contain D flip-flops to capture the outputs. These logic elements are connected together at synthesis by the toolchain that maps the VHDL functionality to a combination of these logic elements. Building up large numbers of these interconnects and logic elements define the runtime function of the FPGA. Architectures described by the VHDL language allow specific tasks to be accomplished and can also be changed at will during the design process. Unlike microprocessors with fixed instruction sets, FPGAs allow custom architectures and operations to be specifically developed for a targeted application. The FPGA and CPLD function in much the same way, with the CPLD having much less resources available to the user but is also developed with VHDL code defining the interconnect of the logical blocks. Both technologies allow building architectures that target specific applications. Given the large amount of Input/Output (IO) pins of the CPLD and FPGA, the auxiliary resources available to the FPGA such as memory blocks, multipliers, and phase locked loops, designers are given great flexibility in determining how to create an optimal architecture for the required design. The FPGA functions at the center of the marmoset collar and controls the sensors and peripherals. The CPLD functions as a system power controller concerned mostly with boot-up and turning on and off peripherals and sensors. These devices are ideal for their flexibility in developing the optimal custom computer architecture needed for collecting and processing sensor data. The tradeoff is the increase in power consumption that is greater than using low-power microcontrollers. However, microcontrollers limit design flexibility and would be difficult to use with low power SDRAM for example.

2.3 MEMS Microphone Use and Development

The microphone being used is the InvenSense ADMP621 (InvenSense bought Analog Device's microphone product line). It is a microphone based on MEMS process technology and comes in a 4 x 3 x 1 mm package. The microphone lends itself well to digital development as the output has already been digitized into a pulse density modulated (PDM) [1] single bit stream. For a PDM signal, the density of the pulses encodes the amplitude of the continuous signal. The frequency response of the microphone runs from 45Hz to 20kHz, which allows recording of the marmoset's vocalizations. Use of a cascaded integrator-comb (CIC) filter [2] allows the PDM bits streamed from the microphone to be stored in microSD flash as signed pulse-code modulation (PCM) [3] word values. The CIC filter is computationally efficient as it requires no multiplies. The FPGA's flexibility allows implementation of the CIC filter using filter design tools available in Matlab. The InvenSense microphone allows sampling up to 3.6Mhz and this is the clock rate we supply to the microphone. The audio data is stored as PCM values, as this is the traditional data type of computers and compact discs whereby the amplitude of the signal is encoded as a signed 16-bit value. The stored PCM word values are then read from the microSD card using a Matlab script and further processed or played back. A PCM 16-bit word sampling rate of 56kHz has been achieved with this system.

The audio samples are time stamped, which is done through use of the GPS time mark functionality. Microphones mounted on an entire troop of marmosets, which have been time stamped with absolute time information, will allow for beamforming to be conducted on the data set once recovered from the SD cards. Direction of sounds relative to the marmoset troop can be ascertained through array processing techniques to steer sensitivity of the microphone array in different directions. An estimate of external sound directions related to the troop of marmosets can thus be obtained.

2.4 Data Storage: MicroSD and Low Power SDRAM

MicroSD flash technology allows large data storage capacity (currently up to 200 GB) in a compact form factor and is one of the recent technologies that have enabled this project. MicroSD cards have a form factor of 15 x 11 x 1 mm and weigh 0.5 grams. MicroSD is rated at speeds up to 208Mhz and theoretically can achieve data throughput up to 104MB/s. Initialization and data write operations to the SD card involve a series of commands sent by the host (FGPA) with responses from the SD card, all of which need to be formed and timed correctly. Commands guide the microSD card through initialization and ready it for data transfer. Data transfer includes sending data to the card, reading data from the card, and retrieving SD card registers. The SD Group's SD Specifications provided the framework for writing the VHDL SD communication interface for the microSD card. [4]

A VHDL entity and associated architecture comprised of state machines has been developed to guide the microSD card from power on, through initialization and mode changes, to a state whereby data can be transferred to the card successfully at high throughput. Mode changes include changing the card to a 50Mhz operating state as well as changing the SD card to transmit data over all four of its data lines, as the SD card initially defaults to a one bit data transmission. Other mode changes include the change to a 1.8V signaling mode from the default 3.3V signaling mode. Communications signaling indicates the voltage levels at which the binary data transmissions occur to and from the microSD card. A change to 1.8V signaling enables the card to transmit data at frequencies faster than 50Mhz, speeds which are not currently

targeted in this implementation. The minimal addressable piece of data of newer microSD cards is termed a block and is 512 bytes. The microSD VHDL design includes an internal buffer made from FPGA internal memory. This buffer serves as a block aligned pool from which data can quickly be sent from and is within the control of the microSD VHDL controller. This allows the controller to hold blocks in buffer to make sure they pass data transmission error checks performed by the SD card. This protects against lost data blocks and adds the functionality to resend data blocks which were not received successfully by the SD card. SD commands and data sent between host and card are protected with cyclic redundancy check hashes which allow sensing transmission errors. CRC engines are included in the VHDL design and are implemented to calculate hashes for commands and data sets.

The microSD development has achieved a VHDL component that can write data successfully to the microSD card. The current implementation targets sequential writes to the microSD card utilizing the SD communication protocol. Functionality such as reads and high level abstractions such as a file system have not been implemented. This implementation is concerned primarily with data logging, which saves data sequentially to the microSD card in binary form. Throughput to the SD card on average has been measured to be much greater than the input data rates from the sensors. Throughput has been recorded at speeds of approximately 10MB/s on average per 1MB of data on writes, which exceeds the speeds at which data is assembled.

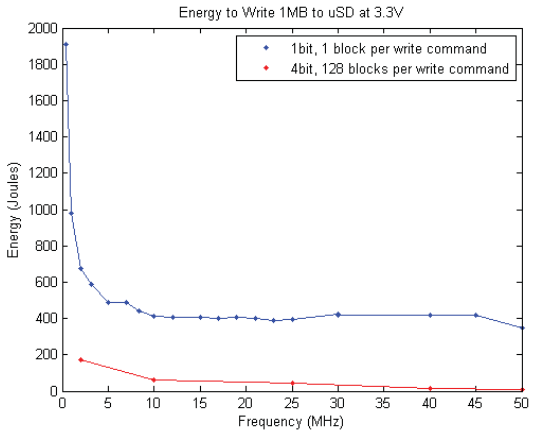

Figure 2. Initial microSD Energy Measurements. This shows that using all four data lines and larger streams is significantly more energy efficient than using a one bit single block data interface. 11.5 joules are used to write 1MB in 4bit 128 block mode at 50MHz.

Initial power studies of the microSD writing patterns showed that buffering data before sending it to the microSD card resulted in significant energy savings. The savings in energy can be seen as the difference between upper and lower curves shown in Figure 2. The energy to write 64KB of buffered data to the microSD card versus writing the same 64KB of data using 512 byte blocks in series required approximately one quarter the energy. The difference in these transfers involves the amount of data streamed without additional interleaved commands. A combination of both writing to the card at high frequency and streaming longer sets of data to the card increases throughput to the card and allows less time spent in an active write state. This reduces the energy needed to write large amounts of data. Current usage by the microSD card while writing has been recorded at 40-50mA, while less than 1mA when not writing. Getting data to the card in large fast chunks saves energy. A low power buffering strategy was found to aide this power design goal. A Micron low power 64MB SDRAM functioning in a self-refresh mode can sustain data in memory at less than 700uA. Buffering larger data sets in low power SDRAM and then writing large chunks of data as fast as possible to microSD flash reduces overhead on the microSD card allowing lower energy expenditure per data block write. The duty cycle of data write is less than 2% when considering data throughput of 10MB/s and input data rate of the microphone. Thus buffering allows much less time spent in a higher energy state where the SD card is actively writing data. Engaging the microSD card with larger data sets requiring less energy to write and allows the microSD card to remain dormant for longer periods of time. The write strategy involves filling a large buffer in low power SDRAM and subsequently writing this buffer to SD flash as quickly as possible, which is currently implemented at a 50Mhz data clock rate with maximum bus width of 4 bits.

While the average achieved throughput of the microSD card has been recorded at 10MB/s, the microSD card automatically implements wear leveling operations which can cause internal data relocations. Wear leveling operations can be seen in power graphs as longer higher current periods. These internal wear leveling operations cause significant decrease in data throughput on a block by block basis temporarily. Use of the SDRAM allows for a large buffer space to store data for writes to the microSD card and avoid small decreases in microSD throughput and associated possible buffer overflow. Buffering data on the FPGA itself would require large amounts of limited FPGA memory blocks, all of which consume more power than the low power SDRAM and take away resources which could be used for other areas of the design.

To enable faster data rates, the SD protocol allows changing communication signaling voltages from 3.3V to a 1.8V signaling level by using a command response sequence and then changing the level voltages. A level translator chip, the Texas Instruments TXB0106, was selected to switch the line voltages and explore 1.8V signaling. Power studies of the total system showed that the level translator chip selected actively uses power. The level translated system was found to use on average 20mW more total system power during data write. The level translation functionality is still present in the VHDL microSD controller system for future high speed designs (>50 MHz) but will not be used in the current design

for power considerations. Future designs targeting higher clock frequency and data throughput (writing only) can make use of the currently designed VHDL interface.

2.5 Inertial Measurement Unit

The Inertial Measurement Unit (IMU) being used is the ST Microelectronics LSM9DS1. This IMU features an accelerometer, gyroscope, and magnetometer in a 3 x 3.5 x 1 mm package for a total of 9 sensing axes. Register configurability of the device allows different full scales for the sensors lending to different sensitivities as well as programmable sampling rates. A VHDL design has been developed for this IMU to initialize the IMU into a functioning state and retrieve data from the IMU overs its SPI interface buses. Matlab functions have been written to create the setup files needed to initialize the IMU to the desired non-default state. The functions generate initialization files for a ROM programmed in the FPGA. At startup the IMU VHDL core, utilizing the SPI communications transmits the non-default register definitions to the IMU. Flexible scripting of the IMU register startup values allows many configurations of the IMU to be tested quickly. This allows for power studies based on IMU axis sampling rate and device configuration. Interrupt pins on the IMU are programmed to represent each of the unique data types that the IMU can produce; acceleration, rotation, and magnetic orientation. Each single axis of the IMU outputs a 16-bit two's complement word. The total data size of the 9 axes is thus 18 bytes. The IMU VHDL component makes use of an FPGA system time counter to time stamp all interrupts and thus all data samples. The IMU component time stamps any word values presented by the IMU at the exact time that the IMU interrupt indicates new data present. These axes words are then presented along with the time stamp to the data forming component of the FPGA system for eventual storage on the microSD card. Enabled axes, sampling rates, and filtering operations can all be changed to conserve power while targeting a particular data type and level of precision.

2.6 Global Positioning System

A GPS VHDL component has been developed for the U-blox Max 7Q GPS receiver. The VHDL component utilizes a Universal Asynchronous Receiver/Transmitter (UART) protocol and bus structure to communicate with the GPS receiver. A specific communication protocol developed by U-blox termed the UBX protocol is utilized in this design. A system has been developed to exercise both the accurate time stamp functionality of the GPS as well as retrieving position data. The Max 7Q allows an interrupt provided by the FPGA to be accurately time stamped. Utilizing the UART bus and UBX protocol, the time that this rising edge was asserted can be retrieved from the GPS. This time is then read using the UBX protocol which gives a microsecond timing precision at which the rising edge occurred. The current VHDL GPS core issues an interrupt and parses the time stamp to periodically log 1μs absolute time accuracy time checks against internal 50 MHz counters.

The contents of the UBX navigation solution packet, which includes latitude and longitude information, are retrieved from the GPS transceiver upon adequate satellite acquisition by the receiver. The navigation solution and associated packet include position information and accuracy estimates. The position values are stored into assembled microSD data blocks as ECEF coordinates along with the GPS provided accuracy estimates.

It is the timing functionality of the Max 7Q which allows the collar to insert GPS time stamps into the data stream being sent to microSD flash. An internal FPGA time is also maintained by the FPGA utilizing the system 50 Mhz clock. This counter is also assembled into the data stream being sent to the microSD card. Making use of both the GPS time mark at intervals and the internal FPGA counter allows calculation of when any piece of information is recorded into the system. This time marking allows the various data stream elements to be related to each other temporally and allows recorded sounds and other data across multiple animals to be time synced with each other.

2.7 Data Assembler

A data assembler VHDL system has been created to assemble the incoming data from multiple sensors, each with different data types and sizes, and package the information into 512 byte blocks, a block being the addressable data size of the microSD card. Sub compartments of the block are termed segments and each segment is given an identifier. Data assembled into these segments become available at different rates and thus the data assembler needs to prioritize certain data segments, which typically is data with faster sample rates, such as the microphone data. Segments defined allow all incoming sensor data to be assembled into their respective segment type. Audio is the fastest incoming sensor data currently at 56 kHz per microphone. Its associated segment is continually left open and built as data is captured. The audio segments are only closed when other pieces of data are captured and another segment is built. Circular buffers are implemented for the sensor data to allow closing a segment and processing another segment where no data is lost in the process. Block sequence numbers allow for missing blocks to be accounted for, as well as sequenced. Segment trailer numbers identify the amount of data in any segment and the type and structure of that data. Invalid data can be determined from an invalid segment trailer at the end of a block. This system aims to be robust and flexible enough to create a highly parseable data stream and allow the addition of new segments for new sensors to be easily added in the future. Using the defined segment types, a Matlab parser separates out data streams and associates times with data samples. This provides the basis for further analysis of the data once extracted from the collar system.

2.8 RF Transceiver

An RF transceiver chip has been identified which will allow remote communication with the collar. Data such as the microSD card write level, battery level, and GPS coordinates will be subassembled by the data assembler and passed to the transceiver for transmission. Periodic transmission will occur at user defined (5-10 minute) intervals and base stations will record the transmitted data allowing researchers to monitor recording activity across a marmoset colony. The transceiver is a bidirectional system and thus researchers will also be able to issue commands to the collar. Current commands targeted include a drop collar functionality allowing researchers to more easily recover logged data from a marmoset. The transceiver selected makes use of a SPI communication bus allowing implementation via the VHDL SPI component.

2.9 Energy Systems

The energy system to power the collar targets a rechargeable battery and multiple solar cells. The battery chosen is a 550mAh Lithium Manganese Oxide cylindrical type. Selected solar cells manufactured by Spectrolab are rated up to 31mA in full illumination. Collar geometry will dictate final solar cell arrangement. Control and investigation of the energy system is handled by two integrated circuits. A Linear Technology DC/DC converter allows solar cell output voltage to be stepped to battery recharge voltages. The solar cells connected to the DC/DC converter can be operated at their maximum power point through setting the targeted input voltage to the solar controller. Output of the solar controller can also be stepped and maintained to the optimum battery recharge voltage. A Texas Instruments battery fuel gauge IC has been implemented on the development board. Through use of its associated Inter-Integrated Circuit (I2C) bus, information about the battery such as capacity, available energy, and time to empty can all be ascertained. The energy subsystem requires further characterization and development, but the functionality to provide advanced power cycling is present in the current development board.

3 Design Considerations

3.1 CPLD Power Management

A CPLD was chosen specifically to handle powering on and off active devices and implement system control in the case when the FPGA is powered off. The CPLD has control of enable lines of all power rails on the collar. It thus has the ability to turn on and off the FPGA and all connected sensors and peripherals. Switches attached to the power rails of sensors and peripherals allow partial system shut down. This allows finer system control and power utilization. While the CPLD has control of the enable line tied to all system switches, it is not the processing unit which decides which sensors and peripherals turn on. For this the FPGA transmits a control register over an SPI bus implemented between the FPGA and CPLD. While the control register is transferred to the CPLD, the CPLD returns status information about the system to the FPGA. These status bits include status pin levels of the battery monitor and solar controller as well as power rail conditions. This allows system management by the FPGA based on the returned status bits.

3.2 FPGA Flexibility

The FPGA architecture allows for great flexibility in system design. An abundance of IO pins allows for devices to be selected at will, some with high pin counts such as the SDRAM memory. Use of a microcontroller or chained microcontroller system may provide a smaller power footprint but would hamper design decisions given the limited IO and hardened off chip communications of microcontrollers. We have selected the sensors and peripherals utilizing varying communication protocols and buses which target the experiment at hand. The flexibility of design and peripheral choice will extend to daughter board design as well, increasing the usability and pertinence of the platform. Current and future DSP operations are possible with the FPGA that would be impossible using a microcontroller.

3.3 Real Time Clock and Persistence

Powered down persistence of the system dictated several design decisions. The FPGA loses its programming upon loss of power and this configuration must be stored. A flash memory retains the FPGA bit stream for reprogramming the FPGA upon power on. This flash memory is programmed before deployment to the field and contains the FPGA's runtime architecture. Reprogramming of the FPGA from the flash memory is initiated by the CPLD whose responsibilities also include interpreting when the system can be powered on given the battery level of the system.

To maintain persistence, pieces of data are necessary to be stored between power cycles for continued operation of the collar. A four megabit magneto resistive random access memory (MRAM) has been selected. Data retention of the part is specified at 20 years with unlimited writes. Critical data include the write pointer to the microSD flash as well as other data such as if the last shutdown was completed successfully. The handling of this persistent data requires VHDL components concerned with persistence of their data to update their respectively defined fields in a double buffered FPGA memory block. The developed magnetic memory VHDL controller functions in either updating this dual port ram from magnetic memory or updating the fields in the physical magnetic memory. At startup, for example, the magnetic memory controller will retrieve the last successfully written microSD address. This becomes the start SD write address for newly assembled blocks. As data is written to the microSD card, the last successfully written block is updated in the double buffered ram. During run time the magnetic memory controller refreshes the appropriate buffer of the dual port ram into magnetic memory over the SPI bus. In this

fashion, persistence between complete power loss events is obtained.

A real time clock (RTC) has been selected for the design utilizing an I2C communication bus and a 32 bit second counter. The RTC's programmable register set allows alarms to be triggered to the CPLD at specific intervals. This functionality is important as in this power limited design the system can wake to target animal activity associated with a specific time. For example, marmosets are vocally active at 6:00 am and 6:00 pm and not active during the heat of the day. This means we will want to record at times when we can expect the best data and not waste power at unproductive recording times. An alarm can trigger the CPLD to power on the FPGA, sensors, and data systems to begin recording behavioral data. As the CPLD is the system power controller, it interfaces directly with the RTC to watch for wake times. This functionality allows the limited power budget to target specific animal behavior at specific preset times.

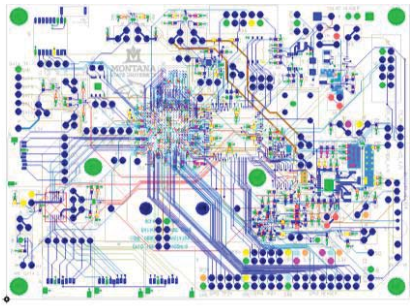

Figure 3. Development PCB which is 4.75x3.50 inches.

3.4 Miniaturization and Final Form Factor

Fitting the development board to the marmoset requires miniaturization as well as 3D printing of a collar which will both house the electronics and reduce the effect of the system and collar on the behavioral study. The prototype development board for making power measurements of all active parts is shown in Figure 3. This development board has been miniaturized and broken into subsystems for the system which will fit the final collar. The working core PCB design has been migrated to a smaller form factor. The final form factor created is a 1.36" by 1.18" PCB board utilizing 10 total layers for signal routing, power and ground. This base PCB board has been fabricated and parts mounted. This board houses the core of the design which includes the FPGA, CPLD, power regulators, and SDRAM. Sensors, peripherals, and further functions will be placed on a daughter board, which interfaces with the main board via two 50 pin miniature connectors. The daughter board will house the sensor functionality. The sensors already being developed on the initial larger development board will be migrated to the daughter board. This design decision allows the main board to be the expensive and time intensive components in terms of PCB place and routing, while add-on daughter boards can be designed quickly and relatively cheaply compared to the main board. Future daughter boards will add further sensors apart from those initially targeted and developed.

3.5 Initial Power Measurements

To monitor system power usage, an analog to digital converter (ADC) has been selected and used through development to help characterize the system. The current ADC used is the Texas Instruments ADS131E08, which is an 8 channel ADC capable of sampling up to 16,000 samples per second using the provided software and development board. Power monitoring points have been added to all sensors and component rails so that an active component's power footprint can be monitored with the given ADC. Using two of the ADC channels, one can measure voltage at and current through a sense resistor to characterize power utilization of a sensor or component. Measurements up to this point have targeted microSD power characteristics as well as total system power and current draw.

One system configuration which tested writes to the SD card used 120mA when not actively writing to the microSD card. At this draw the system will have approximately a 4 hour window of recording time given one of the currently specified batteries. Another minimal FPGA design utilizing close to no FPGA fabric has shown a system current usage of 90mA. This suggests a 6 hour activity window using the most recent power measurements. This gives an approximate upper bound of the recording window given the current system. CPLD alone functionality has been recorded at 9mW of power usage, a current draw of 2mA.

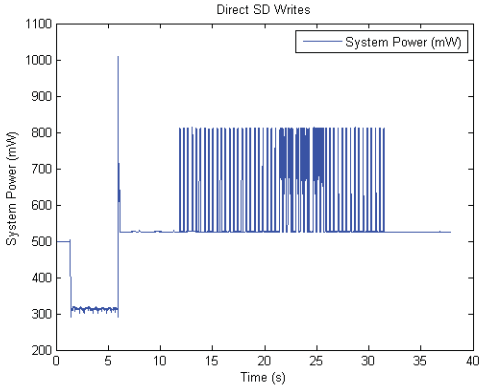

Figure 4. Total System Power Writing 50MB to microSD.

Figure 4 shows a power curve of the entire development system as it writes 50MB to the SD card. The drop in power near the beginning of the curve is when the FPGA is programmed by the CPLD. These power measurements are early estimates that do not include all sensors or peripherals. Power usage will increase as more functionality is added to the design, more resources are added to the FPGA, and other devices are brought online. Further efforts will go into

utilizing the power reduction pathways built into the FPGA toolsets as well as implementing low power HDL design practices. Selection of a lower power FPGA is also being actively considered. We are exploring the use Microsemi's Igloo2 FPGAs due to their low power capability.

4 Future Directions

The platform thus far allows for many future experiments and extensions of the base system. While the current platform is initially power limited due to the size of the target animal, future animal studies might target larger animals. A larger animal and thus larger power budget will increase recording time and also allow the addition of additional sensors to the daughter boards. Experiments targeting a lab setting would be less sensitive to power limitations since researchers could simply exchange batteries between experiments.

FPGAs lend themselves very well to real-time DSP processing, allowing real-time filtering operations to be performed. This platform is also in the process of being targeted as a cochlear implant preprocessor where it will be performing real-time frequency shifting. This platform will map a marmoset's hearing range to the frequencies which a human cochlear processor is designed for, allowing off-the-shelf human cochlear processors to be used. The processors send excitation to the implanted cochlear electrodes to excite the auditory nerve. These signal processing frequency shift operations can be done in real-time utilizing the FPGA. Filtering operations done upon the microphone data can be altered through DSP operations in the FPGA or stored to microSD flash. This is just one example of further projects very well suited to this recording platform.

It is envisioned that neural recording functionality be eventually added to the recording system. Intan's biomonitoring systems [5] allow neural signals to be digitized where the data is sent via a SPI bus for data acquisition. These small biosense amplifier ASICs could record the neural activity in the auditory cortex of a marmoset via 64 implanted electrodes. Correlation between acoustic patterns and neural activity would allow neuroscientists to study the primate auditory cortex in a natural behaving context. Other targeted applicable sensors include MEMS ultrasonic transducers. Adding this sensor would allow characterization of the auditory scene above 20 kHz and the full range of marmoset hearing.

Finally, as the design of the collar system has been done in a hardware descriptor language, a design could be hardened into an application specific integrated circuit (ASIC). Doing so would reduce power consumption considerably if an ASIC targeting a specific usage scenario is warranted.

5 Conclusions

We are developing a powerful and flexible system for recording a significant amount of data on a platform small enough to be used on small primates. Furthermore, the system allows real-time processing of signals that opens new experimental paradigms to be considered. While the system is power limited, it provides enough recording time and processing power to be useful. The power budget and feasibility of collecting data given the FPGA centric system was one of the collar project's initial questions. Development and verification have proven many vital components within the system, given a specific power window. This system allows data to be taken in a scientific domain needing the data to confirm current hypotheses. Initial power measurements indicate a usable window of recording time and so feasibility of the system has been demonstrated. Further optimization of the system power consumption along with verification of other sensors and peripherals will provide more functionality, allowing for behavioral and communication studies of the marmoset.

6 References

[1] InvenSense, "Wide Dynamic Range Microphone with PDM Digital Output," 21 November 2013. [Online]. Available: Wide Dynamic Range Microphone with PDM Digital Output.

[2] R. Lyons, "Understanding Cascaded Integrator-Comb Filters," Embedded Systems Programming, p. 14, 2005.

[3] W. Stallings, "Digital signaling techniques," Communications Magazine, IEEE, vol. 22, no. 12, pp. 21-25, December 1984.

[4] SD Group, SD Specifications Part 1 Physical Layer Simplified Specification Version 3.01, 2010.

[5] Intan Technologies, "Digital Electrophysiology Interface Chips," 12 November 2012. [Online]. Available: http://www.intantech.com/files/Intan_RHD2000_series_datasheet.pdf.

Acknowledgements

This work is being funded by NSF Award No. DBI-1254309.

Real Heart Valve Model for Different Severity Level of Mitral Regurgitation

Carolina Rosas-Huerta[1], **and Jorge Fco. Martinez-Carballido**[1]
[1]Electronics Department, National Institute of Astrophysics, Optics and Electronics, Luis Enrique Erro 1, Santa María Tonantzintla, Puebla, México.

Abstract - *The purpose of Electrical based Cardiovascular System Modeling is to study pressure signals at the vascular level. This work proposes a model to study abnormal heart valve conditions, which are diagnosed using blood flow velocity profiles, leading us to a dynamic model using the 3 phases of a real valve operation; quick opening, slow closing, and quick closing. The model is used for mitral valve regurgitation conditions and tested three severity conditions. For testing purposes the model was implemented in VHDL-AMS for the electrical analog circuit of the valves, for mitral valve regurgitation, giving the corresponding pressure signals. Our dynamic blood flow model was implemented in VENSIM, which allows for generation of blood flow velocity profiles and volumes; thus allowing medical personnel to simulate several conditions in regurgitation and observe the ultrasound derived blood flow velocity profile for severity level of regurgitation.*

Keywords: *Cardiovascular system, Mitral valve, Regurgitation, Model, Cardiac cycle*

1 Introduction

Cardiovascular system analysis started with the modeling of arterial flow using Windkessel model. This was subsequently expanded to cover the modeling of other organs such as the heart, heart valves, and veins [1]. Cardiovascular system models using electrical systems have two limitations: using diodes to represent heart valves, and not including a representation for chambers. Using VHDL-AMS heart valves can be replaced using model of real heart valve operation [2] and observe blood flow and blood pressure. For the case of abnormal valve with regurgitation the electrical model does not provide a way to observe chamber volume and velocity profile that are used to diagnose regurgitation. This led us to develop a dynamic model for the cardiovascular system that does allow for chamber volume and velocity profile observation. The velocity profile is commonly used for the calculation of the severity of this kind of diseases from an echocardiogram [3], and by observing the E and A waves; it is possible to observe abnormal performance of the valves.

Models offer parameters in order to experiment physiological dynamics with different purposes, i.e. improving the diagnosis by simulating some abnormal states for the modeled region of the human body, in this case the heart. The heart is composed by 4 chambers and 4 valves, the valves control de blood flow through the heart when it pumps [3].

The design of a functional valve model helps to improve the understanding of its dynamics given that valves dysfunctions are important heart abnormalities [4]; such as, the ischemic mitral insufficiency, mitral regurgitation, that can be defined as the backflow of blood into the left atria, when the ventricle contracts. This abnormality was represented by the abnormal closing of the mitral valve [5].

Use of the hydraulic-electric analogy to model the cardiovascular system dynamics is a common one [6] [2] [7] [8] [9], in these models, the representation of the heart valve is a diode with a resistance, this analogy describes the ideal flow through the valve, but it is no possible to simulate the backflow for a dysfunction as the regurgitation. In order to show the valves' function there are studies focused in modeling the valves and heart dynamics, Moorheada et al. [10], use a non-linear rotational spring model for the dynamics of the mitral valve, that incorporates into a cardiovascular model, can be used to investigate the hemodynamic repercussions of several pathological conditions; Paeme et al. [11], present a cardiovascular model that includes the mitral valve dynamics, this model was designed with the purpose of studying the Ischemic mitral insufficiency, but it has a large number of parameters, the author mentions the need for new minimal and more physiologically relevant mitral valve models, our study works toward a simpler model.

This work proposes a valve model that uses cardiac cycle phases and the flow control in order to model a closer representation of their operation based on its shape and values of the blood flow through the valve in order to study some dysfunctions such as mitral regurgitation and how these affect the cardiovascular dynamics.

2 Valve's Model

The valve's model used in this paper, see Fig. 1, is based in the 7 phases of cardiac cycle for timing control, depending on the heart rate Fig. 2. From [12] three distinct phases of aortic valve operation were observed: a rapid valve opening, a slow systolic closure, and a rapid valve closing operations. Our model has three stages for representing the valves'

operation as well, these are: quick opening, slow closing and quick closing for each valve.

The opening and closing stages are synchronized with the heart rate and the flow shape of the valve aperture is given by,

$$f_{MV}(t) = \frac{f_M}{1 + \rho_{MV}^{-(t_S * f_M)}} \quad (1)$$

Where, $f_{MV}(t)$ is the blood flow function through the valve, f_M is the transmitral flow, ρ_{MV} gives slope of the opening function, t_s is the stage time of the valve, this parameter is given by the cardiac cycle phases. The slow closing stage is the period of time that the valve reaches the fully open state and starts to closing. Using this valve's model allows to represent mitral regurgitation by changing some of its parameters.

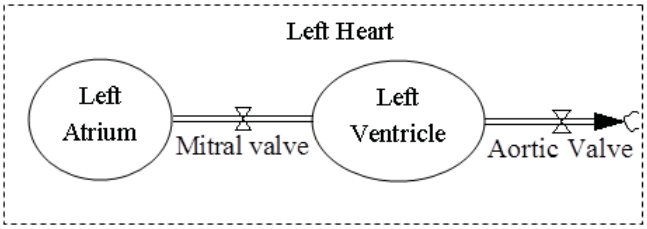

Fig. 1 Schematic representation of valves and left chambers.

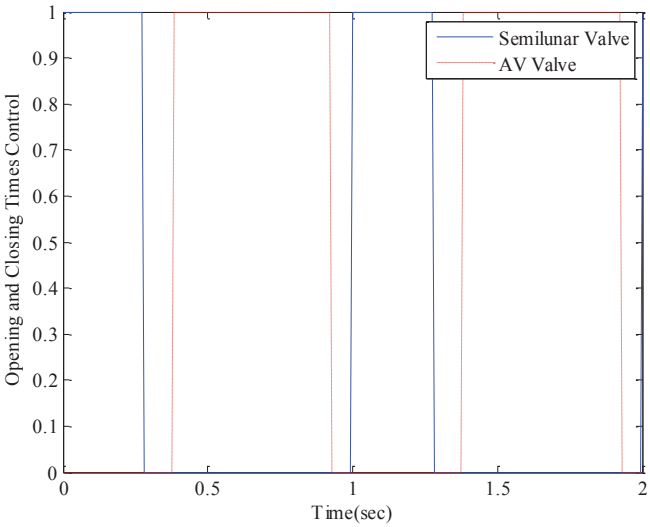

Fig. 2 Semilunar an atrioventricular valves timing.

2.1 Valve's Replacement

From the cardiovascular system study and literature review is clear that real valve operation to allow blood flow is a more complex procedure than a simple change of status between open and closed as described by the idealized diode model [1].

This model represents the operation of the valve by using three stages, based on real opening and closing characteristics [13].

The ideal diode in [6] was replaced with the proposed model and the performance of the cardiovascular model was tested, the original model is in Fig. 3 .

Fig. 4 shows the replacement of diodes by modules with proposed design. With the purpose to demonstrate the functionality of this model, the cardiovascular model from [2] was used and the ideal valve model of valves was replaced with the proposed design, as illustrated in Fig. 4.

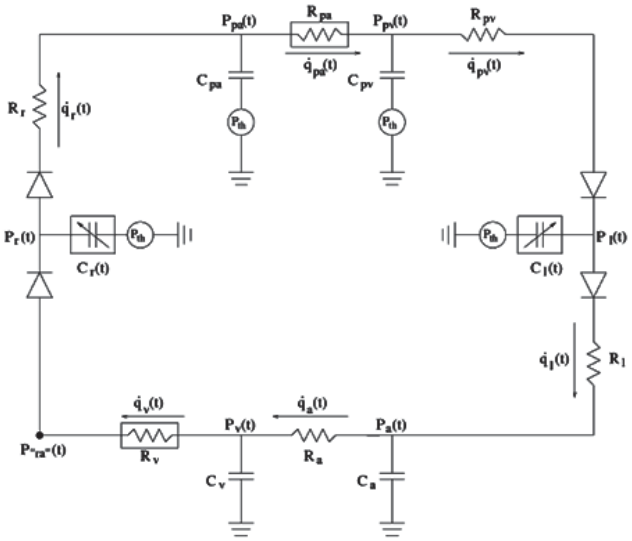

Fig. 3 Electrical circuit analog of the human cardiovascular system. Figure extracted from [2].

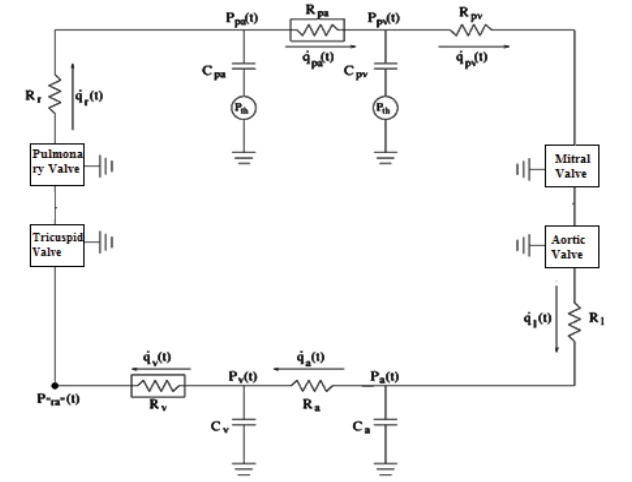

Fig. 4 Electrical circuit analog of the human cardiovascular system with valve replacement. Figure adapted from [2].

2.2 Valve's Modules in VHDL-AMS

With the purpose to test our model in an electrical model of the cardiovascular system, and due to its nature, it became necessary to choose a platform to implement it and replace the diodes of the common cardiovascular system model of an electrical. VHDL-AMS was a convenient choice, because of the facility to develop parameterized modules, as well as flexibility in modifying the design and the components connection, that comes with the VHDL environment.

Two modules were developed: one for each type of valve (AV valve and Semilunar Valve) and each one was parameterized depending on the heart valve replaced. The modules are designed as electrical components with the functions previously presented that model real heart valve operation, and are controlled by the timing given by the cardiac cycle phases; this model definition is in Listing 1. The design has one module per component: a capacitor, a resistor, an inductor, a diode. The connection of the electrical model is in Listing 2, including the designed model for the valves. The aortic pressure waveforms are shown in Fig. 5.

```
-- Atrio-ventricular valve.
ENTITY AV_valve IS
GENERIC (   Fa : REAL     :=0.65;
--Valve Parameters
            HB : REAL     :=150.0;
            Base : REAL     := 3.0;
            period: real := 1.0;
      -- Cardiac Cycle phases
      A: real:=0.14;
      C: real:=0.12;
      D: real:=0.16;
      E: real:=0.1;
      F: real:=0.15;
      G: real:=0.26);
    PORT(TERMINAL p,m: ELECTRICAL;SIGNAL
input1,input2: in bit); --Interface ports.
END AV_valve;

-- Semilunar valve.
ENTITY Sem_valve IS
GENERIC (    Fa : REAL     := 1.5; --Valve
parameters
             HB : REAL     := 150.0;
             Va: REAL  := 1.96;
             Base : REAL     := 3.0;
             period: real := 1.0; -- HR control
      -- Cardiac cycle phases
      A: real:=0.14;
      C: real:=0.12;
      D: real:=0.16;
      E: real:=0.1;
      F: real:=0.15;
      G: real:=0.26);
    PORT(TERMINAL p,m: ELECTRICAL;SIGNAL
input1,input2: in bit); --Interface ports.
END Sem-valve;
```

Listing 1. VHDL-AMS Valves Module definition

Once the replacement was done, we noticed that was not possible to illustrate the regurgitation with the signals obtained from the electric analog model, so a cardiovascular model based on blood flow and volume dynamics was designed due to the main purpose of this work is to study the mitral regurgitation effects and these are not notorious in this kind of models.

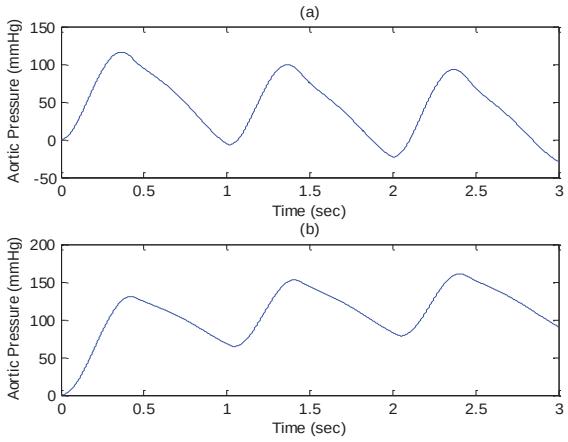

Fig. 5 Aortic Pressure waveform from [2], (b) Aortic Pressure waveform with our valve model.

2.3 Cardiovascular blood flow dynamics model in Vensim

The heart is formed by four chambers, two atria and two ventricles. The atria receive blood from lungs and body and pass it into the ventricles. During each cardiac cycle, the atria contract first, ejecting blood into their respective ventricles, then the ventricles contract, ejecting blood into the pulmonary and systemic circuits [3].

It is important to mention that the two ventricles contract at the same time and eject equal volumes of blood to the lungs and body.

Our proposed model subdivides the human cardiovascular system into six blocks or compartments, four of these compartments are the heart chambers representation; the remaining two are for pulmonary's and body's vascular systems, see Fig. 6. All compartments are inter-connected and hold to the volume conservation law.

Each cardiac chamber is described by volume and blood flow dynamics and cardiac cycle phases. Four chambers (right atria, left atria, right ventricle and left ventricle) are modeled as container compartments. Each one has an initial volume value, which is given by the user, depending on the heart's size. Their dynamics are regulated by the opening, slow closing, and quick closing times for valves, in turn controlled by the cardiac cycle phases.

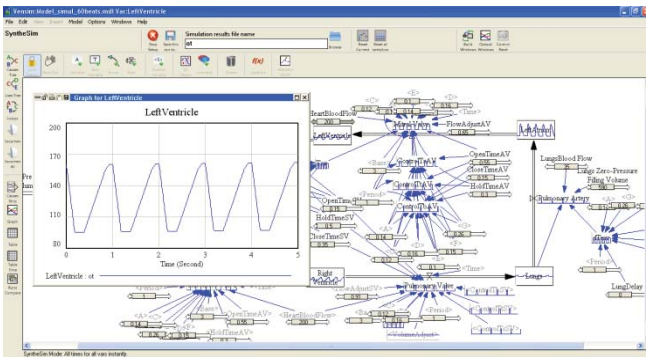

Fig. 6 Proposed cardiovascular model in Vensim [14].

Each chamber has two valves controlling input and output blood flow; these valves allow the diastole (filling) and systole (draining) for each chamber, these actions (diastole and systole) represent the complete cardiac cycle and are used to estimate the stroke volume; that is, the volume of blood pumped from one ventricle of the heart for each beat. Its value is obtained by subtracting end-systolic volume (ESV) from end-diastolic volume (EDV) for a given ventricle [3].

$$SV = EDV - ESV \tag{2}$$

The cardiac output (CO) as the volume of blood being pumped by the heart in one minute, either the left or right ventricle, is given by the following formula

$$CO = SV * HR \tag{3}$$

Where HR is the heart rate and SV is the stroke volume. These values are used for the volume analysis, and are used to verify that the model is working properly.
As previously mentioned before the volume in each chamber is controlled by their input and output valves. The chamber volume is the accumulation of the difference of blood flow through the valves.

3 Mitral Regurgitation Modeling

The mitral regurgitation is modeled by introducing to the normal valve's model different parameters and timing control (reversed opening and closing times, in order to hold the valve partially open (during closing stage), when the mitral valve has to be fully closed, we introduce a backflow into the atria that represents the regurgitation flow.
From (1), the f_M parameter, can be changed by a regurgitant blood flow as is shown in Fig. 7.

```
LIBRARY DISCIPLINES;
USE DISCIPLINES.ELECTROMAGNETIC_SYSTEM.ALL;

ENTITY cardioVas4  IS
END;

ARCHITECTURE behav OF cardioVas4  IS
    TERMINAL n1,n2,n3,n4,n5,n6,n7,n8,n9,n10,n11,n12:
ELECTRICAL;
  SIGNAL S1,S2,S3,S4: BIT;
BEGIN
    -- Circuit conections
rpu:ENTITY resistor(behav) GENERIC MAP (0.006) PORT
MAP (n1, n2);
rp:ENTITY resistor(behav) GENERIC MAP (0.07)PORT MAP
(n2, n3);
rm:ENTITY  resistor(behav)  GENERIC  MAP  (0.006)PORT
MAP (n3, n4);
rv:ENTITY resistor(behav) GENERIC MAP (0.04)PORT MAP
(n7, n8);
rs:ENTITY resistor(behav) GENERIC MAP (1.0)PORT MAP
(n8, n9);
ra:ENTITY  resistor(behav)  GENERIC  MAP  (0.006)PORT
MAP (n9, n10);
   -- Capacitors
cpu: ENTITY c (behav) GENERIC MAP (9.0)PORT MAP (n2,
electrical_ground);
cpa: ENTITY c (behav) GENERIC MAP (7.7)PORT MAP (n3,
electrical_ground);
cv:  ENTITY  c  (behav)  GENERIC  MAP  (100.0)PORT  MAP
(n8, electrical_ground);
cs: ENTITY c (behav) GENERIC MAP (2.0)PORT MAP (n9,
electrical_ground);
      -- Valves replacement
rx: ENTITY resistor (behav) GENERIC MAP (1.0) PORT
MAP (n4, n5);
ry: ENTITY resistor (behav) GENERIC MAP (1.0) PORT
MAP (n6, n7);
rz: ENTITY resistor (behav) GENERIC MAP (1.0) PORT
MAP (n10, n11);
rw: ENTITY resistor (behav) GENERIC MAP (1.0) PORT
MAP (n12, n1);
rxx:ENTITY resistor (behav) GENERIC MAP (1.0) PORT
MAP (n11, n12);
ryy:ENTITY resistor (behav) GENERIC MAP (1.0) PORT
MAP (n5, n6);
 --Valves
ao:    ENTITY    sem_valve    (behav)    PORT    MAP
(n11,electrical_ground,S1,S2);
mit:       ENTITY    Av_valve    (behav)    PORT    MAP
(n12,electrical_ground,S3,S4);
pul:    ENTITY    sem_valve    (behav)    PORT    MAP
(n5,electrical_ground,S1,S2);
tric:       ENTITY    Av_valve    (behav)    PORT    MAP
(n6,electrical_ground,S3,S4);

FF:   ENTITY FlipFlop_s_ao   (behav) PORT MAP (S1);
FF1:   ENTITY FlipFlop_b_ao   (behav) PORT MAP (S2);
FF2:   ENTITY FlipFlop_su   (behav) PORT MAP (S3);
FF3:   ENTITY FlipFlop_b   (behav) PORT MAP (S4);

END behav;
```

Listing 2. Cardiovascular system for Fig. 2.

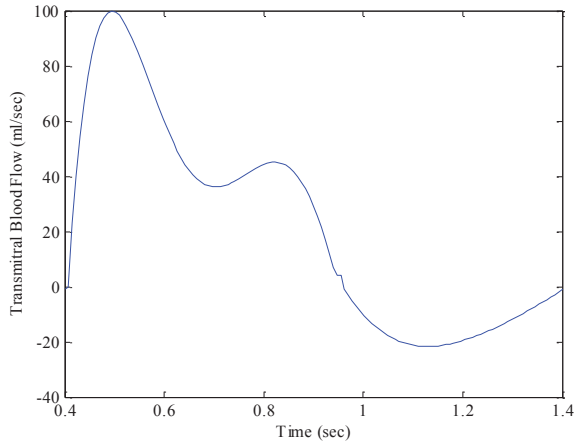

Fig. 7 Transmitral blood flow with regurgitation

The velocity profile was calculated by using the aperture area, and the regurgitant blood flow; these parameters are customizable in order to modify the severity of the regurgitation, the relation used for the velocity is given,

$$\frac{dv}{dt} = \frac{f_{MV}(t)}{A} \tag{4}$$

Where, v is the velocity, $f_{MV}(t)$ is the blood flow through the valve, and A is the aperture area of the valve.
To compute the regurgitant volume, we use the Proximal Isovelocity Surface Area or PISA method where the regurgitant volume is given by,

$$Rvol = EROA \times MR\_VTI \tag{5}$$

Where *Rvol* is the regurgitant volume, *EROA* is the Effective Regurgitant Orifice Area and *MR_VTI* is the Velocity Time Integral of the regurgitation. Model's parameters are given in Table 1.

Table 1: Model Parameters

General Parameters		
Parameter	**Normal sample value**	**Test range**
Heart rate (HR) (bpm)	60	60–180
$V_{RV}(t_0)$ (ml)	160	100-160
$V_{LV}(t_0)$ (ml)	165	100-165
$V_{RA}(t_0)$ (ml)	34	14-56
$V_{LA}(t_0)$ (ml)	35	15-58
Valve Parameters		
f_M (ml/sec)	100	50-100
ρ_{MV}	3	0-5
MR TVI (m)	0	10-500
EROA (m)	0	0-2

4 Simulations and Results

Simulations were made for different severity levels of the regurgitation, mild, moderate and severe regurgitation [15]. The parameter modified for the simulations is the EROA.

The TVI was measured using the velocity profile obtained for each simulation, by calculating the integral of the regurgitant velocity. These values were used to calculate the regurgitant volume using (5). The results are given in Table 2.

Table 2: Simulation parameters and results

Severity	**EROA (cm2)**	**TVI (cm)**	**Rvol (ml/beat)**
Mild	0.05	188	9.4
	0.1	141	14.1
	0.15	147	22.1
	0.18	166	29.9
Moderate	0.2	165	33
	0.25	170	42.5
	0.3	168	50.4
	0.35	166	58.1
Severe	0.5	125	62.5
	0.8	88	70.4
	1	79	79
	1.2	72	86.4

Fig. 8, shows the velocity profile for a mild, moderate and severe regurgitations, these graphs were used to calculate the TVI from the baseline to the velocity peak wave.

From the results it is observable that the velocity decreases when the EROA increases, this is due to the relation that exists between the area and transmitral blood flow. Validation of the Rvol corresponds with the standard values for the severity classification of mitral regurgitation given in, 2014 AHA/ACC Guideline for the Management of Patients With Valvular Heart Disease [16].

5 Conclusions

Our model was implemented in VHDL-AMS, to check its functionality with an electrical model of the cardiovascular system. These models do not represent chambers. This type of model does not provide blood flow velocity profile; thus, we provide aortic pressure to observe the real valve operation.

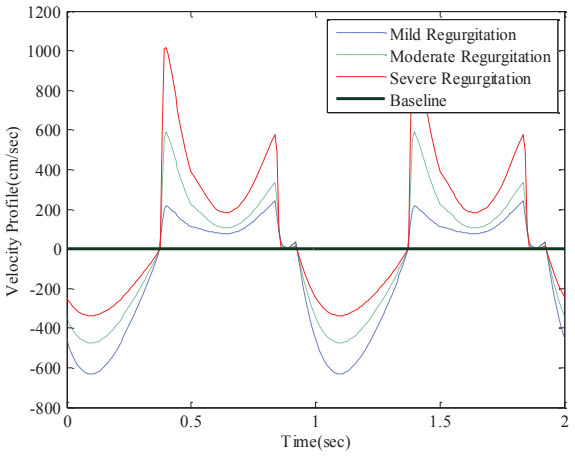

Fig. 8 Velocity profile with mitral regurgitation levels.

To provide blood flow, and volume information that will enable visualization of velocity profiles, the valve model was implemented, simulated and presented results that are consistent with medical diagnosis techniques of some abnormal conditions in valves. For this we used Vensim from Ventana Systems, Inc.

This valve model can represent a variety of abnormal valve's operations by using parameters. Models based on electrical analogs use diodes as valves, and then valves' dynamics does not closely represented and do not offer abnormal functioning. Valves were designed in its three real stages; opening, slow closing and quick closing, and each one have a parameterized function for their operation. The valves' parameters control shape and time; this enables representation for mitral regurgitation. This disease is represented by the changes in the velocity profile calculated by the model. It is possible to represent the different levels of severity for the regurgitation by changing some of the available parameters of the model.

6 References

[1] Y. Shi, P. Lawford and R. Hose, "Review of Zero-D and 1-D Models of Blood Flow in the Cardiovascular System," *Biomedical Engineering Online,* vol. 10, no. 33, 2011.

[2] R. Mukkamala and R. J. Cohen, "A forward model-based validation of cardiovascular system identification," *American Journal of Physiology - Heart and Circulatory Physiology,* vol. 281, p. H2714–H2730, 2001.

[3] F. H. Martini, Anatomy & Physiology, San Francisco CA: Pearson Education, 2005.

[4] K. B. Chandran, "Role of Computational Simulations in Heart Valve Dynamics and Design of Valvular Prostheses," *Cardiovascular Engineering and Technology,* vol. 1, no. 1, p. 18–38, 2010.

[5] X. Zeng, T. C. Tan, D. M. Dudzinski and J. Hung, "Echocardiography of the Mitral Valve," *Progress in Cardiovascular Diseases,* 2014.

[6] K. Lu, J. W. Clark Jr., F. H. Ghorbel and D. L. Ware, "A human cardiopulmonary system model applied to the analysis of the Valsalva maneuver," *American Journal of Physiology - Heart and Circulatory Physiology,* vol. 281, p. H2661–H2679, 2001.

[7] R. T. Cole, C. L. Lucas, W. E. Cascio and T. Johnson, "A LabVIEWTM Model Incorporating an Open-Loop Arterial Impedance and a Closed-Loop Circulatory System," *Annals of Biomedical Engineering,* vol. 33, no. 11, p. 1555–1573, 2005.

[8] S. A. Stevens and W. D. Lakinb, "A mathematical model of the systemic circulatory system with logistically defined nervous system regulatory mechanisms.," *Mathematical and Computer Modelling of Dynamical Systems: Methods, Tools and Applications in Engineering and Related Sciences,* vol. 12, no. 6, pp. 555-576, 2006.

[9] M. Abdolrazaghi, M. Navidbakhsh and K. Hassani, "Mathematical modelling and electrical analog equivalentof the human cardiovascular system," *Cardiovascular Engineering,* vol. 10, no. 2, pp. 45-51, 2010.

[10] K. Moorheada, S. Paemea, J. Chaseb, P. Kolha, L. Pierarda, C. Hannc, P. Daubya and T. Desaive, "A simplified model for mitral valve dynamics," *Computer Methods and Programs in Biomedicine,* pp. 190-196, 2013.

[11] S. Paeme, K. T. Moorhead, J. G. Chase, B. Lambermont, P. Kolh, V. D'orio, L. Pierard, M. Moonen, P. Lancellott, P. C. Dauby and T. Desaive, "Mathematical multi-scale model of the cardiovascular system including mitral valve dynamics. Application to ischemic mitral," *Biomedical Engineering Online,* vol. 10, no. 86, 2011.

[12] R. G. Leyh, C. Schmidtke, H.-H. Sievers and M. H. Yacoub, "Opening and closing characteristics of the

aortic valve after different types of valve-preserving surgery.," *Circulation,* vol. 100, no. 21, pp. 2153-2160, 1999.

[13] S. Arjunon, S. Rathan, H. Jo and A. P. Yoganathan, "Aortic Valve: Mechanical Environment and Mechanobiology," *Annals of Biomedical Engineering,* vol. 41, no. 7, p. 1331–1346, 2013.

[14] Vensim, "Vensim," Ventana Systems, Inc, [Online]. Available: htttp://vensim.com. [Accessed 10th April 2015].

[15] Y. Topilsky, F. Grigioni and M. Enriquez-Sarano, "Quantitation of Mitral Regurgitation," *Seminars in Thoracic and Cardiovascular Surgery,* vol. 23, pp. 106-114, 2011.

[16] R. A. Nishimura, C. M. Otto, R. O. Bonow, B. A. Carabello, J. P. Erwin III, R. A. Guyton, C. E. O'Gara PT, N. J. Skubas, P. Sorajja, T. M. Sundt III and J. D. Thomas, "2014 AHA/ACC Guideline for the Management of Patients With Valvular Heart Disease," *Journal of the American College of Cardiology,* vol. 63, no. 22, 2014.

State of the Art Mock Circulation Loop and a Proposed Novel Design

T. Batuhan Baturalp and A. Ertas
Department of Mechanical Engineering, Texas Tech University, Lubbock, TX, USA

Abstract – *A novel fully-automated systemic mock human circulation loop (MCL) design is proposed with a wide literature review of MCL and left ventricular (LV) form and function. Drawbacks and strengths of current MCLs and their pumping systems are investigated and an inference has been made for requirements of a novel MCL design. It has been found that proposed MCL design should not only capable of replicating wide range of cardiac operating scenarios, but also pumping system should better represent LV for simulating various cardiovascular diseases particularly muscular dysfunctions. Also, the proposed MCL design should be fully-automated that controls essential MCL parameters such as compliance, resistance. Medical papers showed that LV has principal functionalities such as elastance, torsional and twisting motion of ventricular wall, which play important role on motion and contraction of LV. These features are implemented on a proposed pneumatic muscle actuated LV.*

Keywords: MCL, Mock circulation loops, Mock circulatory systems, Pneumatic Mock Left Ventricle

1 Introduction

Heart disease is agreed as the highest cause of death in the world by most of the health organizations. Heart disease and stroke statistics of American Heart Association [1] states that, on basis of 2009 death rate data, cardiovascular disease was the reason for one of every three deaths in the United States. According to other sources, 2150 Americans die because of cardiovascular disease each day which is an average of one death every 40 seconds. Heart failure can be treated by medications, medical devices and surgery. With respect to another source [2], approximately 4000 cases each year require a heart transplant, however only less than half of them can receive one. Currently, there are about 5 million Americans who suffer because of heart failure, and over 500,000 patients are diagnosing each year [3]. The increasing donor shortage and limited heart transplant waiting time generates a need for a temporary solution such as an assistive device to keep the patient alive while a donor is being found. Most of the cardiac failures happen in the left side of the heart which is the part of the heart that pumps blood to the body. Left Ventricular Assistive Devices (LVADs) have been developed to increase the cardiac flow output of the LV chamber.

While LVADs provide a solution for patients who suffer from cardiac insufficiency, Valvular Heart Disease (VHD) is widely accepted as another significant portion of heart diseases. Valvular heart disease involves problems on one or more of the valves of the heart (the aortic and mitral valves on the left and the pulmonary and tricuspid valves on the right). It can be treated by medication and generally with valve repair or artificial heart valve replacement. In 2003, over 290,000 heart valve operations were performed worldwide with an increase of 10 to 12% per year. Thus, a rough estimation can be made that it will exceed 850,000 in 2050 [4]. Another study [5] shows that VHD covers a percentage between 10% and 20% of all cardiac surgical procedures in the United States. Up to the present, over 4 million people across the world have received an Artificial Heart Valve (AHV) [6]. Replacement of artificial heart valves have been done in last six decades, since the first replacement performed in 1952. During the last six decades more than 50 artificial heart valves have been designed developed [7].

MCLs play an essential role not only in vitro testing (not in a body) and development of LVADs and AHVs, but also other circulation related devices such as total artificial hearts, artificial lungs, vascular grafts, bioreactors for tissue engineered heart valves and intra-aortic balloon pumps. Cardiac device design procedures generally adopt MCLs before advancing to animal or clinical trials which are much more troublesome and expensive. With respect to standards of The American Society for Artificial Internal Organs (ASAIO) and the Society of Thoracic Surgeons (STS), experimental flow loops should correctly represent significant parameters of the human circulatory system under normal and worst-case physiologic conditions [8]. Also, Clemente et al. [9] published an article which conducts the setup of technical standard for mechanical heart assist devices and approach to problems related to technical standards for biomedical devices. Various physiological cardiac failure or operating scenarios needs to be replicated in the MCL for testing, including but not limited to LVADs and heart pumps. These different scenarios require a fully-automated MCL which can reproduce the necessary conditions precisely and switch between them without trouble. Based on listed essential MCL functionalities, not only MCL actuator parameters such as geometry, different movement trajectories and elastance of ventricular wall, but also versatility of the MCL parameters such as resistance and compliance are critical and needed to be developed for imitating different scenarios of human circulation on an experimental setup.

The aim of this study is to propose a novel MCL design which is fully automated, and capable of replicating wide range of cardiac operating and failure scenarios including

mimicking the movements of left ventricular chamber of heart. The novel design of a new MCL should include some several important factors. A wide literature review is presented in this paper to seek these factors on MCLs. These factors can be listed as versatility of the hemodynamic parameters like resistance and compliance. In addition, the pump of the MCL should be more realistic than the ones in the literature, since the state of art pulsatile blood pumps are not capable to mimic torsion and wringing action of the LV, muscular dysfunctions of the heart and more realistic shape of the chamber.

1.1 Background

Mock circulatory loops in the literature, can be categorized into two main groups with respect to their flow types: non-pulsatile and pulsatile systems. Generally, flow type is defined by the pump or actuator of MCL. Non-pulsatile flow MCLs uses continuous pumps such as centrifugal or axial pumps, while pulsatile MCLs are equipped with various pumps (piston, cam driven, diaphragm based pumps, and pneumatically and hydraulically operated pressure chambers) in the literature. Recent developments showed that normal physiological cardiac conditions can be reproduced by using slaughterhouse pig hearts which are used for their morphological and physiological similarities to human hearts.

The initial MCLs were mainly used on testing artificial hearts. One of the earliest MCL was built by Kolff et al. [10] in 1959. It was including both systemic and pulmonary circulation loops, and the ventricles were activated by use of compressed air chambers. The biggest incomplete side of this design was resistance, because no resistance valve is used in this study. Another early in vitro test setup was developed by Bjork et al. [11] in 1962 to examine prosthetic mitral and aortic valves. The study claims that developed system was capable of accurately simulate various physiological conditions. The system consisted of interconnected valve testing chambers, aortic analogue, peripheral resistance, and left atrium analogue. Peripheral resistance and vertical position of the reservoir were adjustable. Main contribution of this study was usage of collapsible molded rubber sac LV. A good example for initial MCL designs with flexible tubing and cam driven ventricle was Reul et al.'s [12] design in 1974. Their study was also one of the leading studies that used Windkessel chamber with adjustable air volume for compliance. The downside of this study was lacking of suitable connection to connect VADs. Pennsylvania State University mock circulation system is another example to remarkable MCL designs which is developed by Rosenberg et al. [13] in 1981. The MCL consisted of resistance, compliance, inertia, systemic and pulmonary circulation, VAD connections, and adjustable cardiac conditions. While the MCL represented acceptable results and provided a proper in vitro testing setup for artificial hearts, inertia values were incorrectly assumed to be equal for systemic and pulmonary circulations.

As stated previously, MCL can be categorized into two main groups as pulsatile and non-pulsatile with respect to their flow generation types. Since there are many studies in the literature about MCLs, this categorization can be widened regarding to type of mock circulation system's pumps. Many different pumping and actuation systems are used on MCLs but they can be categorized into four principal groups such as: biological, piston, VAD, and pressure chamber based pump systems.

1.1.1 MCLs with Biological Pump Systems

In recent years, biological pumps systems were started to use in MCLs in order to create more realistic simulations. In most of the studies in the literature, entire explanted hearts were integrated into in vitro setups. The reason behind this approach is allowing a better preservation of the anatomical structures and at the same time not including all the physiological complexities of animal models. Other advantages of using explanted hearts are, enabling the potential applications of new experimental apparatus, or surgical procedures since the environment is more familiar to surgeons to operate and analyze their hemodynamic effects.

Since the use of entire explanted hearts is inconvenient due to the required protocols, complexity and cost, it had been suggested by Richards et al. [14] to use the explanted hearts as a passive structure which means pressurizing the blood from another source and using the chamber feature of the heart. An external pulsatile pump was used in this study, and results were found to be not optimal especially in terms of flow rates and the pressure wave forms. This study was followed by Leopaldi et al. [15] by using an entire explanted porcine heart, whose LV is pressurized by an external pumping system. Electrically conditioned latissimus dorsi muscles are also used for actuation in various studies [17 - 20].

Most of the whole heart mock loop designs were accomplished to maintain cardiac contractility ex-vivo. The explanted working-heart models were capable of reproducing the physiological ventricle pressure-volume relationship with state of art mimicking the shape and motion of the real heart, although the complexity and costs of the related experimental protocols represented serious drawbacks. The PhysioHeart platform was developed by Hart et al. [20] to overcome some gaps in the study of comprehensive cardiac mechanics, hemodynamics, and device interaction of MCLs. Cardiac performance of the MCL was controlled and kept at normal levels of hemodynamic performance for up to four hours. Cardiac changes and performance of an entire heart during an explantation into the developed in vitro apparatus are investigated by Chinchoy et al. [21]. Similarly, left ventricular ejection function of ex resuscitated pig hearts was examined by Rosenstrauch et al. [22]. Left ventricular function was restored and maintained in all six hearts for 30 min in this circuit. Although usage of explanted whole hearts has great advantages such as reproducing the ventricular wall motion,

geometry, and contraction, they have a major drawback on duration of experimentation since they don't contract more than six hours. This drawback makes fatigue and long-term testing of cardiovascular devices impossible which are crucial on validation of these devices.

1.1.2 MCLs with VAD Pumps

VADs are used in MCLs not only as a testing device, but also as the main or driving pump. Naturally, those pumps are already tested and usually already available in the market. In this section, brief information will be given about MCLs that use ventricular assistive devices as the main pump.

One of the pioneer studies that utilize a VAD as the major pump of the MCL is researched by Schima et al. [23] who sought for simple and inexpensive solutions for common problems of MCLs. Another study that measures the performance of artificial blood pumps by using them as pump in a MCL is conducted by Knierbein et al. [24]. Also LVADs were used to simulate left ventricular function and aortic flow by Papaioannou et al. [25].

1.1.3 MCLs with Piston Pumps

Piston pumps are advantageous with their mechanical simplicity, reliability, and ease measurement of the variables of interest such as ventricular pressure and volume. They are also more controllable compared to other pumps. Downside of the piston pumps can be pointed as hard to mimic the pulsatile flow and elastic nature of the heart and always has to be in a cylindrical shape which is not similar to real left ventricular shape. In this section, MCLs from selected papers in the literature which are equipped with piston pump as the main pump of the loop will be introduced.

In vitro reproduction of the LV and arterial tree in a mock circulatory system and interaction of them with a left ventricular assist device was examined by Ferrari et al. [26]. In another study of Ferrari et al. [27], an elastance model is used to mimic the Frank Starling's law for reproducing more realistic hemodynamic values. Singh et al. [28] was developed a pulsatile MCL in order to test robustness artificial heart valves and their effects on the parameters associated with the circulatory system. In LVAD studies, not only the design of the device is important but also the control of the device is essential. On this purpose, Vaes et al. [29] was designed and developed a MCL which was capable of featuring the properties of the (diseased) heart and mimicking the baroflex response of the heart.

1.1.4 MCLs with Pressurized Chambers

The need for better elastance, ventricular shape, pulsatile flow and simulating the Frank Starling law led the authors surface the idea of using pressurized chambers for representing the ventricles of the heart. Both pneumatic and hydraulic pressurized chambers were used in the literature. In this section, a brief survey on MCLs that uses pressurized chambers as heart ventricles will be introduced.

A systemic MCL was established to investigate the movements of the heart valves during pulses of the heart by Verdonck et al. [30]. In this study, atria and LV were represented by an elastic bag made of latex in a hydraulic type (water) chamber. Pantalos et al. [31] developed a MCL which was equipped with a pneumatic chamber and flexing polymer sac for testing VADs under normal, heart failure, and partial recovery test conditions. Another pneumatic pressurized chamber type driven systemic MCL was built by Patel et al. [32] to validate LVADs under congestive heart failure, exercise and normal conditions. Arrhythmias and diastolic function problems were focused by Mouret et al. [33] who has constructed a new systemic MCL that was driven by the dual activation simulator. Pantalos et al. [34] developed a mock circulation that behaves differently under altered physiologic conditions for testing cardiac devices. The purpose of the study was to assess the ability of the mock ventricle to mimic the Frank Starling response of normal, heart failure, and cardiac recovery conditions. As seen in the literature of pressurized chamber pump type MCLs, versatility for creating operating conditions and replicating ventricular geometry shines out among features of MCLs. On the other hand, there is still room for development on features like mimicking ventricular wall motion, contraction, and muscle fiber orientation and also operating conditions like muscle dysfunctions which is one of the most common cardiovascular diseases.

2 Novel Design of MCL

A wide literature review has been conducted on MCL designs to investigate the needs to be improved on a novel MCL design. First of all, capability of mock LVs needs to be improved for replicating human LV chamber's movements and physiological parameters for different scenarios such as healthy-rest, healthy-exercise, various cardiovascular diseases and failure states. Additionally, a fully-automated and controllable circulation system is needed in the literature since controllable MCLs has been started to introduce to literature, recently. One example to this kind of studies was conducted by Legendre et al. [35] which was equipped with an engine like mechanism pump system that simulates the LV. Pump system uses a piston to push a diaphragm which enables to create an unsteady flow. Normal healthy and pathologic state patient conditions were simulated in the tests, and their results were compared to results in the literature. The system was found as accurate to simulate in vivo conditions. By current technological developments on the sensors and data acquisition systems, a fully automated and controllable MCL can be built that utilizes controllable valves for resistance, controlled air pressurized compliance chambers for compliance (also known as the reciprocal of elastance) and inertiance can be controlled by the geometry of the tubes and properties of system fluid which has reasonably stable value in human circulation. These parameters will be adjusted to

simulate different cardiovascular states in addition to pump of the system. The pump of the system should be more realistic than the ones in the literature, since the pulsatile blood pumps are not capable to mimic torsion action of the LV, muscular dysfunctions of the heart and more realistic shape of the chamber. An in vitro beating heart simulator should be developed which has seen in the literature as needed for reducing the required time to develop, test, and refine of cardiovascular instruments such as heart valves and assistive devices in general.

Ideal pulsatile pump of a MCL was defined by Knierbein et al. [24] that it should be capable to replicate dynamic properties of the physiological load as close as possible for generating physiological flows and pressures at the intersection between pump and mock loop. Resistances and volumes must be variable in a range which for different pump sizes and different circulatory conditions approximates physiological conditions. Handling of the system must be simple and reliable in order to facilitate reproducibility of test parameters.

The fully-automated systemic MCL was designed in Computer Aided Design (CAD) environment which can be seen in Figure 1.

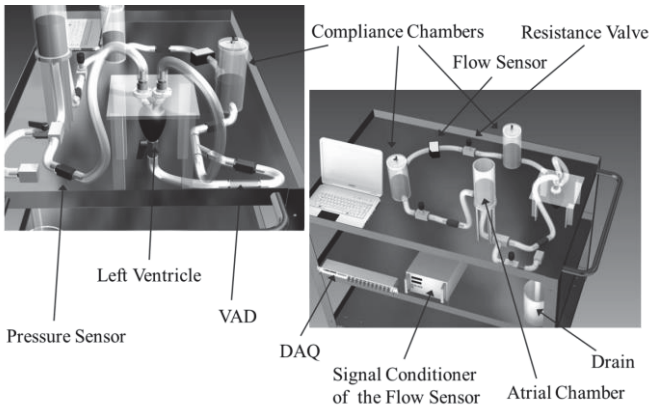

Figure 1 Developed MCL with Annotations.

The developed MCL consists of two compliance chambers for systemic and aortic compliance values. The left ventricular simulator, pressure and flow sensors, resistance valves, a drain container for resetting the system, signal conditioner for the flow sensor, a data acquisition device to digitize outputs of the sensors, and atrial chamber as open air container with adjustable height to generate constant pressure are the other components of developed MCL. Clear tygon tubing with different diameters were used in the system and integrated to the CAD environment with respect to bending radius of the selected tubing. A steel cart was used to add mobility to the design. A bypass tubing from bottom of the left ventricular simulator to aorta was made for mounting the LVADs to the system. This bypass tubing was considered and designed as optional by adding a valve to the bottom of the left ventricular simulator. A pressure sensor was also added to the output of the left ventricular assistive device to evaluate its performance. Clamp-on tubing type flow meters were investigated in the literature for ease of use and non-invasive features to the system, since no physical contact is required with the fluid media. Only one ultrasonic flow sensor (Transonic, ME20PXL) was selected because it is easy to relocate the flow sensor for obtaining measurements from different locations. A stand for left ventricular simulator was also designed to support it while not constraining its contractive motion. Another function of this stand was holding the artificial heart valves and making easier assemble/disassemble process to test different types of heart valves.

Measurement of pressure from various locations in a MCL is essential. Main locations to measure pressure in a systemic MCL are upstream and downstream of the compliance chambers, outlets of atrium and left ventricular chamber and ventricular assistive device. Since compliance chambers are designed with air pressure based adjustment, air pressure transducers are also required.

Human circulatory system has two main resistances which are the systemic and pulmonary. The developing MCL has only systemic circulation and resistances in the sections of MCLs are dependent on the length and cross-sectional area of the pipe. Thus, proportional control valve to adjust level of systemic resistance is crucial in mock circulatory loop design. A computer-controlled proportional valve (Hass Manufacturing Company, Model EPV-375B) was chosen which operates between 1-5 V DC control signal and this valve represents the total peripheral resistance of the circulatory system.

When the blood pressure in a blood vessel increases, it reacts with expanding its volume. This characteristic of the blood vessels is called compliance. It can be considered as inverse of the stiffness since compliance value increases with increasing flexibility. Therefore, compliance should be considered as a controlled parameter in a fully-automated MCL. On this purpose, two pressurized air type compliance chamber were included which represents compliance of pulmonary artery and aorta. These compliance chambers were equipped with computer controlled air regulator to enable the automation of MCL.

2.1 Pump Design of MCL

Developing a realistic mock left ventricular chamber that mimics shape and wall movements of a real LV requires a wide investigation on not only shape and motion of LV, but also orientation and contraction of myocardial fibres. The transformation of the heart shape during the beating is found to be directly related to the pumping performance of the heart. Thus, the motion of the LV wall is essential on replication of the pumping function of the LV. In this section, some studies about left ventricular shape, motion, myocardial fiber orientation and torsion will be introduced and a prototyped pneumatic left ventricular pump will be demonstrated.

Left ventricular form and geometry and impact on its function and efficiency investigated by Buckberg et al. [36] and Sengupta et al. [37]. The effect of myocardial fiber orientation on contractility and helical ventricular myocardial band concept are revealed by Torrent-Guasp [38]. Helical ventricular myocardial band concept was an innovative new concept for understanding three dimensional, global, and functional structure of the ventricular myocardium. Another important aspect for wall motion of LV is the twisting movement of the ventricle during systole which was investigated in detail first time by Streeter et al. [39]. Accepted opinion [40, 41] on cause of the torsional movement of the LV is possible due to the helical orientation of myocardial fibres and the promising opinion on function is creation of a suction effect to assist the diastolic filling. Additionally, the systolic twisting motion stores energy which is to be used during diastole for ventricular filling [42].

In the context of gathered information about architecture of LV, a pneumatic muscle actuated mock LV prototype was manufactured. The geometry was created by lofting cross-sectional representations of left ventricular chamber and it was inverted in CAD environment to obtain mold geometry. The mold consists of three different parts as seen in Figure 2 and it was prototyped by using a 3D printer. While two components of the mold were used to create the outer layer of the LV, the part in the middle creates the inner layer.

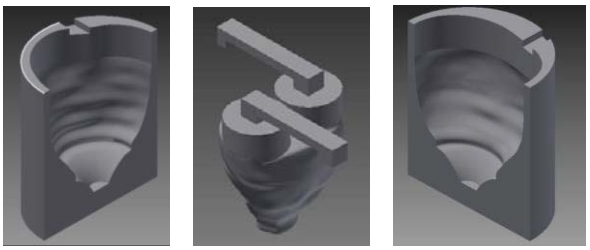

Figure 2 3D Printed Mold of the LV

The printed mold was filled with "Dragon Skin" brand high performance silicone which is reasonably strong and elastic. Additionally, a second mold was designed for forming one solid band in which the custom pneumatic muscles were placed in the desired formation. After the pneumatic muscle band is created by placing three pneumatic muscle fibers together (Figure 3), the band is inserted into the main mold in a helical formation as seen in Figure 4 which shows the completed LV chamber. The pneumatic muscle strips are connected to a series of pressure regulators that contract the ventricle to produce the same effect as that of a real left ventricle. The custom made pneumatic muscles are made from rubber tubing and black pneumatic mesh. While one end of the muscle was folded over and sealed, an inflation needle was inserted at the other end.

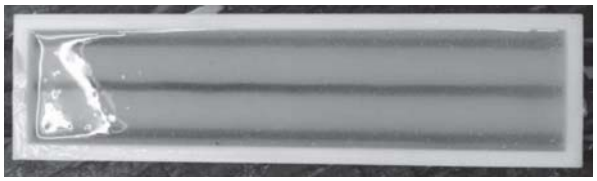

Figure 3 Pneumatic Muscle Band Includes three Pneumatic Muscles and a Strip of Dragon Skin

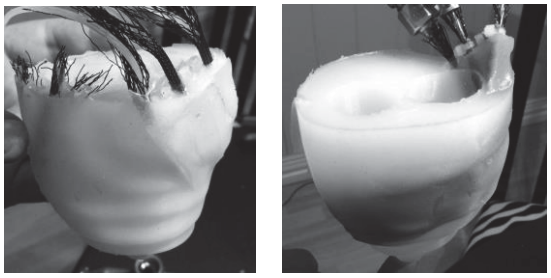

Figure 4 Silicone Molded LV Chamber

The result of the initial tests showed that silicon tissue structurally strong enough since no tears or rips were seen. On the other hand, silicon LV did not deform enough due to high thickness of the LV wall. Contraction was found to be insufficient because of air leaks on custom made pneumatic muscles and thickness of the tissue. However the proof of concept is considered as successful since mock LV wall motion resembles the real LV wall motion. Sufficient contraction can be reached by improvements on thickness of the tissue and performance of pneumatic muscles.

3 Conclusions

Design of a novel fully-automated systemic MCL was proposed in this paper. A wide review on current MCLs and physiological features of LV was conducted and presented. In the light of literature review findings, computer controlled MCL design which is capable of replicating various cardiac operating conditions and able to switch between them smoothly was proposed. Additionally, geometry and wall motion of the real LV was attempted to be implemented on actuator of proposed MCL by prototyping a pneumatically actuated mock LV. The prototyped LV was found to be insufficient in terms of contraction but the reasons of insufficiency were found and improvements are on the way.

4 References

[1] Go, Alan S., Dariush Mozaffarian, Véronique L. Roger, Emelia J. Benjamin, Jarett D. Berry, William B. Borden, Dawn M. Bravata et al. "Executive Summary: Heart Disease and Stroke Statistics: 2013 Update: A Report From the American Heart Association"; Circulation, 127, 1, 143-146, 2013.

[2] Rose, Eric A., Annetine C. Gelijns, Alan J. Moskowitz, Daniel F. Heitjan, Lynne W. Stevenson, Walter Dembitsky, James W. Long et al. "Long-term use of a left ventricular

assist device for end-stage heart failure"; New England Journal of Medicine, 345, 20, 1435-1443, 2001.

[3] Spoor, Martinus T., and Steven F. Bolling. "Valve pathology in heart failure: which valves can be fixed?"; Heart failure clinics, 3, 3, 289-298, 2007.

[4] Yacoub, M. H., and J. J. M. Takkenberg. "Will heart valve tissue engineering change the world?"; Nature clinical practice cardiovascular medicine, 2, 2, 60-61, 2005.

[5] Maganti, Kameswari, Vera H. Rigolin, Maurice Enriquez Sarano, and Robert O. Bonow. "Valvular heart disease: diagnosis and management"; Mayo Clinic Proceedings, 85, 5, 483-500, 2010.

[6] Sun, Jack CJ, Michael J. Davidson, Andre Lamy, and John W. Eikelboom. "Antithrombotic management of patients with prosthetic heart valves: current evidence and future trends"; The Lancet, 374, 9689, 565-576, 2009.

[7] Dasi, Lakshmi P., Helene A. Simon, Philippe Sucosky, and Ajit P. Yoganathan. "Fluid mechanics of artificial heart valves"; Clinical and experimental pharmacology and physiology, 36, 2, 225-237, 2009.

[8] Pantalos, George M., Frank Altieri, Alan Berson, Harvey Borovetz, Ken Butler, Glenn Byrd, Arthur A. Ciarkowski et al. "Long-term mechanical circulatory support system reliability recommendation: American Society for Artificial Internal Organs and The Society of Thoracic Surgeons: long-term mechanical circulatory support system reliability recommendation"; The Annals of thoracic surgery, 66, 5, 1852-1859, 1998.

[9] Clemente, Fabrizio, Gian Franco Ferrari, Claudio De Lazzari, and Giancarlo Tosti. "Technical standards for medical devices. Assisted circulation devices"; Technology and Health Care, 5, 6, 449-459, 1997.

[10] Kolff, Willem J. "Mock circulation to test pumps designed for permanent replacement of damaged hearts" Cleveland Clinic Quarterly, 26, 4, 223-226, 1959.

[11] Björk, V. O., F. Intonti, and A. Meissl. "A mechanical pulse duplicator for testing prosthetic mitral and aortic valves"; Thorax, 17, 3, 280-283, 1962.

[12] Reul, H., B. Tesch, J. Schoenmackers, and S. Effert. "Hydromechanical simulation of systemic circulation"; Medical and biological engineering, 12, 4, 431-436, 1974.

[13] Rosenberg, G., Winfred M. Phillips, Donald L. Landis, and W. S. Pierce. "Design and evaluation of the Pennsylvania State University mock circulatory system"; ASAIO J, 4, 2, 41-49, 1981.

[14] Richards, Andrew L., Richard C. Cook, Gil Bolotin, and Gregory D. Buckner. "A dynamic heart system to facilitate the development of mitral valve repair techniques"; Annals of biomedical engineering, 37, 4, 651-660, 2009.

[15] Leopaldi, A. M., R. Vismara, M. Lemma, L. Valerio, M. Cervo, A. Mangini, M. Contino, A. Redaelli, C. Antona, and G. B. Fiore. "In vitro hemodynamics and valve imaging in passive beating hearts"; Journal of biomechanics, 45, 7, 1133-1139, 2012.

[16] Guldner, Norbert W., Peter Klapproth, Martin Großherr, Andreas Brügge, Abdolhamid Sheikhzadeh, Ralph Tölg, Elisabeth Rumpel, Ralf Noel, and Hans-H. Sievers. "Biomechanical Hearts Muscular Blood Pumps, Performed in a 1-Step Operation, and Trained Under Support of Clenbuterol"; Circulation, 104, 6, 717-722, 2001.

[17] Pochettino, A., D. R. Anderson, R. L. Hammond, A. D. Spanta, E. Hohenhaus, H. Niinami, L. Huiping, R. Ruggiero, T. L. Hooper, and M. Baars. "Skeletal muscle ventricles: a promising treatment option for heart failure"; Journal of cardiac surgery, 6, 1, 145-153, 1991.

[18] Mizuhara, Hisao, Takaaki Koshiji, Kazunobu Nishimura, Shin-ichi Nomoto, Katsuhiko Matsuda, and Toshihiko Ban. "Evaluation of a compressive-type skeletal muscle pump for cardiac assistance"; The Annals of thoracic surgery, 67, 1, 105-111, 1999.

[19] Geddes, L. A., S. F. Badylak, W. A. Tacker, and W. Janas. "Output power and metabolic input power of skeletal muscle contracting linearly to compress a pouch in a mock circulatory system"; The Journal of thoracic and cardiovascular surgery, 104, 5, 1435-1442, 1992.

[20] de Hart, Jurgen, Arend de Weger, Sjoerd van Tuijl, J. M. Stijnen, Chantal N. van den Broek, M. C. Rutten, and Bas A. de Mol. "An ex vivo platform to simulate cardiac physiology: a new dimension for therapy development and assessment"; The International journal of artificial organs, 34, 6, 495-505, 2011.

[21] Chinchoy, Edward, Charles L. Soule, Andrew J. Houlton, William J. Gallagher, Mark A. Hjelle, Timothy G. Laske, Josee Morissette, and Paul A. Iaizzo. "Isolated four-chamber working swine heart model"; The Annals of thoracic surgery, 70, 5, 1607-1614, 2000.

[22] Rosenstrauch, Doreen, Hakan M. Akay, Hakki Bolukoglu, Lars Behrens, Laura Bryant, Peter Herrera, Kazuhiro Eya et al. "Ex vivo resuscitation of adult pig hearts"; Texas Heart Institute Journal, 30, 2, 121-127, 2003.

[23] Schima, H., H. Baumgartner, F. Spitaler, P. Kuhn, and E. Wolner. "A modular mock circulation for hydromechanical studies on valves, stenoses, vascular grafts and cardiac assist

devices"; The International journal of artificial organs, 15, 7, 417-421, 1992.

[24] Knierbein, B., H. Reul, R. Eilers, M. Lange, R. Kaufmann, and G. Rau. "Compact mock loops of the systemic and pulmonary circulation for blood pump testing"; The International journal of artificial organs, 15, 1, 40-48, 1992.

[25] Papaioannou, T. G., D. S. Mathioulakis, and S. G. Tsangaris. "Simulation of systolic and diastolic left ventricular dysfunction in a mock circulation: the effect of arterial compliance"; Journal of medical engineering & technology, 27, 2, 85-89, 2003.

[26] Ferrari, G., C. De Lazzari, R. Mimmo, and DG Ambrosi Tosti. "Mock circulatory system for in vitro reproduction of the left ventricle, the arterial tree and their interaction with a left ventricular assist device"; Journal of medical engineering & technology, 18, 3, 87-95, 1994.

[27] Ferrari, G., C. De Lazzari, R. Mimmo, G. Tosti, D. Ambrosi, and K. Gorczynska. "A computer controlled mock circulatory system for mono-and biventricular assist device testing"; The International journal of artificial organs, 21, 1, 26-36, 1998.

[28] Singh, Dhruv, and Abhishek Singhal. "Design and Fabrication of a Mock Circulatory System for Reliability Tests on Aortic Heart Valves"; In ASME 2007 Summer Bioengineering Conference, American Society of Mechanical Engineers, 753-754, 2007.

[29] Vaes, Mark, Marcel Rutten, René van de Molengraft, and Frans van de Vosse. "Left ventricular assist device evaluation with a model-controlled mock circulation"; In ASME 2007 Summer Bioengineering Conference, ASME, 723-724, 2007.

[30] Verdonck, Pascal, A. Kleven, Ronny Verhoeven, B. Angelsen, and J. Vandenbogaerde. "Computer-controlledin vitro model of the human left heart"; Medical and Biological Engineering and Computing, 30, 6, 656-659, 1992.

[31] Pantalos, G. M., S. C. Koenig, K. J. Gillars, and D. L. Ewert. "Mock circulatory system for testing cardiovascular devices"; In Engineering in Medicine and Biology, 2, 1597-1598, 2002.

[32] Patel, S., Paul E. Allaire, Houston G. Wood, J. Milton Adams, and Don Olsen. "Design and construction of a mock human circulatory system"; In Summer Bioengineering Conference, Sonesta Beach Resort, Florida. 2003.

[33] Mouret, F., V. Garitey, T. Gandelheid, J. Fuseri, and R. Rieu. "A new dual activation simulator of the left heart that reproduces physiological and pathological conditions"; Medical and Biological Engineering and Computing, 38, 5, 558-561, 2000.

[34] Pantalos, George M., Steven C. Koenig, Kevin J. Gillars, Guruprasad A. Giridharan, and Dan L. Ewert. "Characterization of an adult mock circulation for testing cardiac support devices"; ASAIO journal, 50, 1, 37-46, 2004.

[35] Legendre, Daniel, Jeison Fonseca, Aron Andrade, José Francisco Biscegli, Ricardo Manrique, Domingos Guerrino, Akash Kuzhiparambil Prakasan, Jaime Pinto Ortiz, and Julio Cesar Lucchi. "Mock circulatory system for the evaluation of left ventricular assist devices, endoluminal prostheses, and vascular diseases"; Artificial organs, 32, 6, 461-467, 2008.

[36] Buckberg, Gerald, Julien IE Hoffman, Aman Mahajan, Saleh Saleh, and Cecil Coghlan. "Cardiac mechanics revisited the relationship of cardiac architecture to ventricular function." *Circulation* 118, no. 24 (2008): 2571-2587.

[37] Sengupta, Partho P., Vijay K. Krishnamoorthy, Josef Korinek, Jagat Narula, Mani A. Vannan, Steven J. Lester, Jamil A. Tajik, James B. Seward, Bijoy K. Khandheria, and Marek Belohlavek. "Left ventricular form and function revisited: applied translational science to cardiovascular ultrasound imaging"; Journal of the American Society of Echocardiography, 20, 5, 539-551, 2007.

[38] Kocica, Mladen J., Antonio F. Corno, Francesc Carreras-Costa, Manel Ballester-Rodes, Mark C. Moghbel, Clotario NC Cueva, Vesna Lackovic, Vladimir I. Kanjuh, and Francisco Torrent-Guasp. "The helical ventricular myocardial band: global, three-dimensional, functional architecture of the ventricular myocardium"; European journal of cardio-thoracic surgery, 29, 1, 21-40, 2006.

[39] Streeter, Daniel D., Henry M. Spotnitz, Dali P. Patel, John Ross, and Edmund H. Sonnenblick. "Fiber orientation in the canine left ventricle during diastole and systole"; Circulation research, 24, 3, 339-347, 1969.

[40] Rüssel, Iris K., Marco JW Götte, Jean G. Bronzwaer, Paul Knaapen, Walter J. Paulus, and Albert C. van Rossum. "Left ventricular torsion: an expanding role in the analysis of myocardial dysfunction"; JACC: Cardiovascular Imaging, 2, 5 648-655, 2009.

[41] Shaw, Steven M., David J. Fox, and Simon G. Williams. "The development of left ventricular torsion and its clinical relevance"; International journal of cardiology, 130, 3, 319-325, 2008.

[42] Rothfeld, Jeffrey M., Martin M. LeWinter, and Marc D. Tischler. "Left ventricular systolic torsion and early diastolic filling by echocardiography in normal humans"; The American journal of cardiology, 81, 12, 1465-1469, 1998.

SESSION

COMPUTATIONAL BIOLOGY: NOVEL ALGORITHMS AND APPLICATIONS

Chair(s)

TBA

A System for estimating Spatio-Temporal Gait Parameters and Pelvis Kinematics

M.V. Avolio[1], S. Mammolito[2] and G. Spingola[2]
[1]TD Group S.p.a. Palermo, Italy,
[2]E.I. Solutions S.r.l, Palermo, Italy

Abstract

The estimation of the spatio-temporal Gait Parameters (GP) and Pelvis Kinematics (PK) is of primary importance in both physical activity monitoring and clinical contexts. It becomes ever more necessary to have low-cost and user-friendly tools that enable this type of analysis. In this work, we present a waist-worn system created with an inertial measurement units (IMU), comprising a 3D accelerometer and gyroscope, which uses an innovative Bluetooth 4.0 protocol communication system. The algorithm which permits the functioning is based on the interpretation of accelerations and angular rate of the body trunk (waist) in order to estimate the GP, such as: duration and length the step, and kinematics of the pelvis during straight-line walking, by using the same single sensor on the same location. The measurements obtained with this system (device-algorithms) were compared with a Gait Analysis Inertial Platform used in medical laboratories. Moreover, the system has been tested on healthy subjects, where obtained results have resulted comparable with the reference tables regarding the height, gender and age.

Keywords: Gait Analysis, Pelvis Kinematics, Accelerometer, Gyroscopes, Inertial sensor, Bluetooth 4.0.

1 Introduction

Walking is one of the most common human physical activities. Estimate of time and distance parameters during walking is helpful in measuring abnormal gait and is essential for assessment the quantitative evaluation of treatment outcomes for quantify improvement resulting from interventions [1]. Indeed, the amplitude, variability and asymmetry of step length (SL) can be representative of the compensatory mechanisms adopted in pathological walking ([2], [3]). Although already in the 1970s the use of sensors for an analysis of human movement was suggested [4], it is only recently that a number of studies have reported Gait Analyses (GA) based upon the use of accelerometers on trunk, thigh, shank or foot ([5], [6]). A lot techniques have been widely used for research purposes: Hirokawa and Matsumara [7] for instance suggested a system based on camera and walkway with implanted sensors, but this method required considerable time and costs that have hindered their use in clinical practice. Abu-Faraj et al. [8] used pressure sensors attached to the sole to monitor temporal parameters. This technique unfortunately has had limitations, in fact several problems, such as shuffling gait, mechanical failure, or patient acceptance limit their applicability; moreover, such system required the support of a dedicated laboratory. To bypass these limitations, less invasive systems which also permit outdoor measurement (i.e., not only in the laboratory) have been developed, using innovative technologies, such as a powerful microcontroller, miniature sensors, high capacity memory and small batteries. Sparks et al., [9] have introduced the use of miniature kinematic sensors such as accelerometers and angular rate (gyroscopes) sensors with integrated conditioning and calibrating module. The use of Inertial Measurement Units (IMU) containing 3-D axis accelerometers and gyroscopes [10] has proven to be an alternative technique for GA ([11], [12]). They are a strong candidates for the valuation of spatial-temporal GP in open environment, thus overcoming the typical limitations of measurements in indoor laboratory settings ([13], [14]).

The exact scope of this paper is to presents an advanced Multi-Inertial Sensor Platform (Gait Sensor, GS) and to evaluate the performance of a technique based on a sensing device for the analysis of human movement exploiting the potential of short-range communications for data transmission (the Bluetooth standard version 4.0). This last feature differs greatly our work with others that are found in the literature, which have adapted, for example, a ZigBee radio communication type [15].

Therefore, all involved sensors in the our developed Sensor Platform, both commercial or ad-hoc, are non-invasive, Bluetooth based and battery-powered. They required to be used or weared only for the duration of the measurement, avoiding long-term installation on the patient's body. The system has been designed, in fact, to allow the automatic, transparent and safe flow of clinical information, readily acquired by professional caregivers during a visits. Another feature not to be underestimated is the cost down that such a platform has.

The measurements obtained with this system, combined with an suitable algorithm, were compared with corresponding ones obtained by a GA Inertial Platform (GAP) [15] used in the considered medical laboratory. Moreover, the present study was directed at investigating whether the same single sensor on the same location can reliably provide also PK during straight-line walking.

In the following, we report the technical descriptions and the adopted algorithm. Subsequently, experimental results are shown, while conclusions and outcomes described at the end of the paper.

2 Architecture of the Gait Sensor

The new portable Gait Sensor (GS), used for human movement analysis, consists of the device's board (21x26mm), a custom ABS case and a Li-Po rechargeable battery. The device is designed for the low power, low cost, and high performance and integration requirements of latest electronics equipment. The main board is based on an Invensense 9-DOF IMU, which contains three MEMS into a single package (SiP): a 3-axis gyroscope (full scale ±2000 deg/s), a 3-axis accelerometer (max range ±8·g) and a digital compass. Moreover, the SiP contains a dedicated Motion Processor that allows run-time calibration and sensor fusion algorithms. Hence, all sensors on this device are triaxial and an appropriate run-time algorithm allows a perfect space calibration and realignment to solve the typical problem that affects these particular devices. The combination of these three MEMS showed a promising strategy for the extraction of spatio-temporal parameters related to GA.

In addition, we find on board the core and radio transceiver, the power and battery management subsystem, a micro-USB connector for firmware upgrade and battery recharge, an RGB led and a push button, all in a miniaturized fashion. The device uses an ARM Cortex-M0 32-bit microcontroller for embedded applications requiring a high level of integration and low power dissipation, and is powered with a single 250mAh Li-Po battery. Communication with the gateway is achieved with a Laird Technologies Bluetooth 4.0 LE module, integrated into the board. The aspect of the sensor board is shown in Figure 1. First tests of the device showed a battery life (with all sensors active, algorithms running continuously and radio interface in active mode) of about 24 hours.

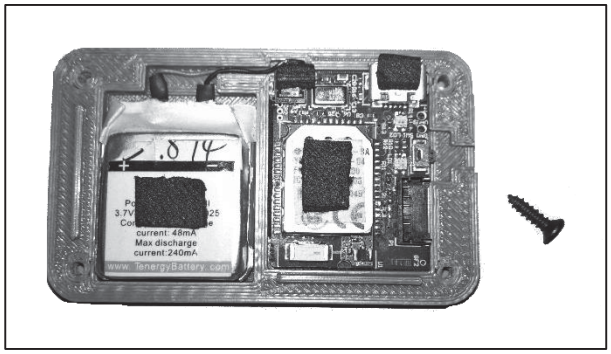

Fig. 1: The GS movement sensor board

3 The Gait Cycle

Temporal and spatial measures examine global aspects of gait. Because gait is a cyclical activity, the basic assumption is that one step is essentially the same as the next. Thus, a parameter such as stride length is expected to be characteristic of the person's overall walking performance, not just the measured step(s). The traditional terminology describes gait in terms of discreet, momentary events, such as heel strike (HS) and toe-off (TO).

A Gait Cycle (GC) begins when a foot hits the ground (HS) and ends when the next HS of the same foot occurs. The GC is a repetitive pattern involving steps and strides. A stride is a whole gait cycle. The step time is the time from one foot hitting the floor to the other foot hitting the floor. The GC involves two main phases: the stance phase and the swing phase (Figure 2). The stance phase occupies 60% of the GC while the swing phase occupies only 40% of it [3]. The stance phase begins with the HS (or Initial Contact IC): this is the moment when the heel begins to touch the ground, and the toes does not yet touch. When the stance phase ends, the swing phase begins. This phase is the phase between the TO phase and the HS phase. The GC involves movement in each part of the leg (and the body). In the pelvic region there is an anterior-posterior displacement, which alternates from left to right (Figure 2). This displacement facilitates anterior movement of the leg. At each side, there is an anterior-posterior displacement of 4-5°.

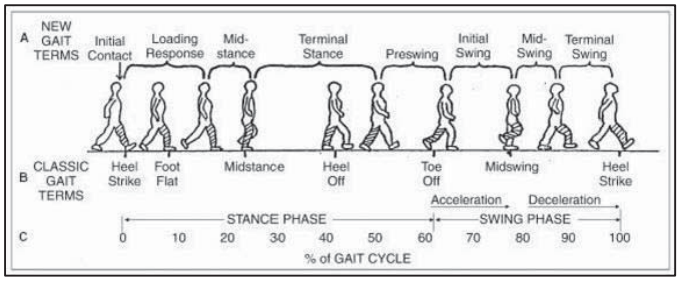

Fig. 2: Usually Classification of the Gait Cycle

3.1 Gait Sensor Algorithm

The algorithm developed in this work deals to determine spatio-temporal GP and kinematics of the pelvis from trunk acceleration and angular data [15]. Zijlstra and Hof [16] suggested that during walking a basic pattern of trunk accelerations with fixed relationships to spatio-temporal gait parameters can be expected.

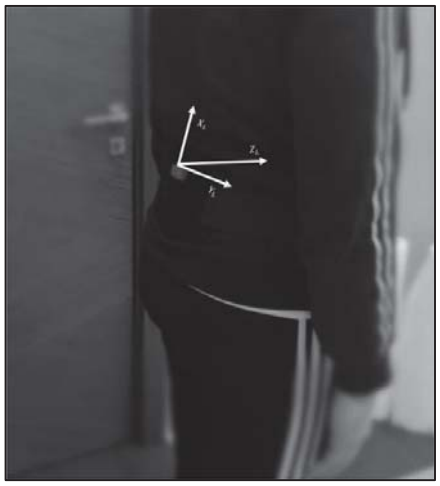

Fig. 3: The IMU location. The IMU attached to the belt and positioned at the center of waist of the subject pelvis and relevant LF.

Therefore, the GS is attached to the subject's waist with a semi-elastic belt, covering the L4-L5 inter-vertebral space with X_L, Z_L and Y_L axes pointing upward, forward, and to the right,

respectively (Figure 3). In the following, the GS Algorithm that solves the following issues is described:

- The identification of gait events;
- The determination of pelvis displacement;
- Pelvis kinematics.

3.2 Identification of Gait Events

The algorithm is applied to the physical quantities from each sensor of the IMU [17] and are measured with respect to the axes of a Local Frame (LF) aligned to the edges of the unit housing. To estimate the IMU acceleration, the orientation of the LF has been aligned with respect to the Global Frame (GF). The GF was defined as follows: the X_G axis coinciding with the direction of gravity, the Z_G axis coinciding with the acceleration component in the direction of progression during level straight walking, and the Y_G axis resulting from the cross product between X_G and Z_G. The orientation of the LF with respect to the GF at the i_{th} instant of time was expressed using the orientation quaternion $qL(i_{th})$. For this purpose, let $a^L(i_{th})$ be the vector obtained from the accelerometer signals (expressed in the LF) at the i_{th} instant of time, then the acceleration vector $a^G(i_{th})$ expressed in the GF can be computed as:

$$a^G(i_{th}) = \begin{pmatrix} a_x(i) \\ a_y(i) \\ a_z(i) \end{pmatrix}^G = \begin{pmatrix} -g \\ 0 \\ 0 \end{pmatrix} + qL(i_{th})a^L(i_{th}) \qquad (1)$$

From the collected acceleration and gyroscope signals, the typical spatial-temporal GP, such as stride duration, swing duration, stance duration, cadence, etc, during a GC [18] are then obtained (see Figure 3), and to compute them it is necessary and sufficient to determine for each leg the precise moments of HS and TO during the considered GC. These events are well distinguished in the anterior-posterior (Z_G-axis) accelerometer signal of GS [15] (Figure 4). To successfully achieve this task, we filtered the signal by a first order Butterworth low-pass filter with a cut off frequency of 2 Hz. The motion analysis was performed with a sampling frequency of 50 Hz. From the clean signal (Figure 4), are extracted the maximum (HS) and minimum (TO) peak and their positions within the GC (Figure 6).

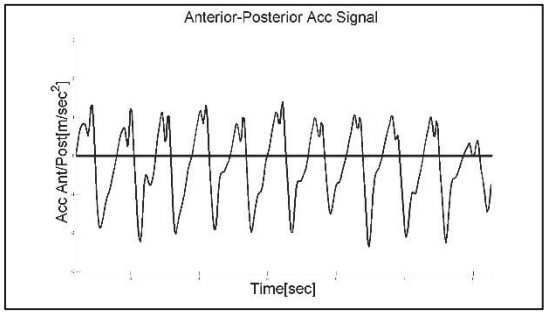

Fig. 4: Antero-posterior acceleration signal from the GS in a representative subject during a straight-line walking, after Butterworth low-pass filtering. Peaks for heel strike are pointed up, peaks for toe-off are pointed down.

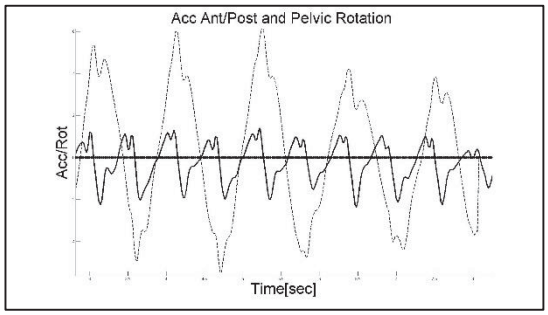

Fig. 5: Antero-posterior acceleration signal (accelerometer Z-axis) and the axial rotation with positive angular values for rotation to the right side.

Antero-posterior acceleration at L5 (Figure 4) was found cyclic, with two close positive peaks (the second positive peak is associated to HS) and a single negative peak (associated to TO). Each step was identified between two consecutives of these peaks. Moreover, to automatically discriminate between left and right steps, the axial rotation with positive angular values for rotation to the right side was analysed (Figure 5). The time-history of GC was then normalized in time by re-sampling these values over 100 samples; in this way, the abscissae axis reports the percentage of duration of Gait Cycle (Figure 6). Based on this identification, the spatial-temporal parameters were determined. The curve in Figure 6 shows that the maximum peak is located about at 50% of the cycle, in correspondence of the heel contact of the contralateral foot. Minimum peaks are at about 10% and 60%, in correspondence of the toe-off events. The values obtained were consistent over the considered subjects, in the range of physiological gait. In particular, results are in line with corresponding values from GA, i.e. the Gait Analysis Inertial Platform (GAP) used in the considered medical laboratory – cf. Table 1.

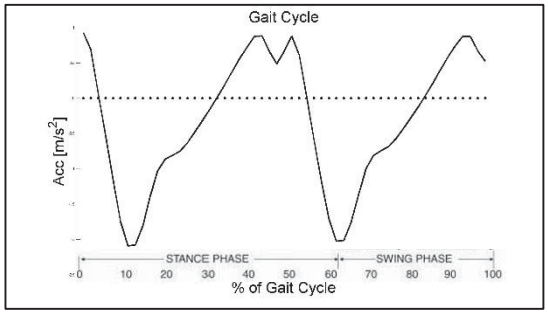

Fig. 6: A representative subject during a straight-line walking. Anterior-Posterior acceleration over the normalized cycle (0 - 100%) of the right leg; the cycle taken was the one observed also by GAP.

To verify the validity of the results we have examined tests performed on subjects of the Mantia Rehabilitation Center of Palermo (Italy). Specifically, the raw data collected by the center's system were also executed on the GS: one of GP values obtained from all subjects are provided in Table 1.

Step Duration [s]			
Subject	**GAP**	**GS**	**Error**
#1	1,12	1,10	1,79%
#2	1,26	1,25	0,79%
#3	1,25	1,19	4,80%
#4	1,19	1,21	1,68%
#5	1,09	1,09	0,00%
#6	1,17	1,17	0,00%
#7	1,21	1,22	0,83%
#8	1,17	1,18	0,85%

Table 1: Comparison of estimates of Step Duration using a GAP and GS.

3.3 Estimation of the Pelvis Displacement

Some studies [16] demonstrated that the displacements of the lower trunk during walking can be well predicted by an inverted pendulum model of the body's centre of mass (CoM) trajectory (Figure 7). Such a model has been described to estimate step length using vertical displacement of the centre of mass [19]. For IMUs worn at the waist, the length of step can be estimated by measuring the vertical displacement of the CoM after double integration of vertical acceleration. This estimation is based on the assumption that the vertical movement of CoM during a step, delimited by two consecutive IC events, is equal to that described by a point mass suspended at the end of an inverted pendulum.

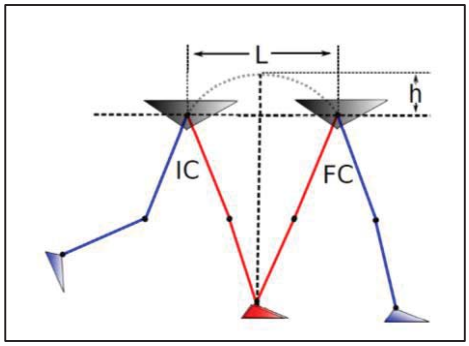

Fig. 7: Motion of the pelvis during a step

The step cycle is divided into two phases: double stance (from IC contact to contralateral Final Contact FC) and single stance (from contralateral FC to next IC). The inverted pendulum model is the step length estimator during this time. The algorithm needs the subject's length, *L*, measured from the external malleolus to trochanter major (L5) and the vertical acceleration signal of the step, from the previous IC event of the contralateral foot to the following IC event of the reference foot. Then, the antero-posterior displacement *d* can be related to vertical displacement according to equation:

$$d = 2\sqrt{2Lh - h^2} \qquad (2)$$

being *h* the vertical displacement of the CoM during the single stance, computed by a double integration of the waist vertical acceleration. This can cause drift errors that accumulate and grow unbounded in time. In this case, we have to implement a zero velocity update (ZUPT) [20] strategy to faults. The ZUPT is performed in the IC event, which defines the step start.

3.4 Estimation of Pelvis Kinematics

Pelvic Kinematics is usually investigated in GA laboratories through a number of different marker sets, but more recently it has been also analyzed by inertial sensors [21],[22]. Such systems can also support the orthopaedist to verify the correct alignment of the pelvis in amputees and in any lower limb intervention, currently assessed only through clinical observations. This would be possible with the minimum encumbrance for the patient and very low costs for the health-care service. The present study was aimed at investigating whether a single inertial sensor on the waist can provide reliable PK during straight-line walking. From the three-axis gyroscope processed signals, the pelvic angles on the three anatomical planes were obtained, which are Tilt (sagittal plane), Obliquity (frontal plane) and Rotation (transverse plane). Pelvic Kinematics was calculated e compared with GAP reference angles [22]. As reported, a good correlation between GS and GAP reference angles was found (Figure 8).

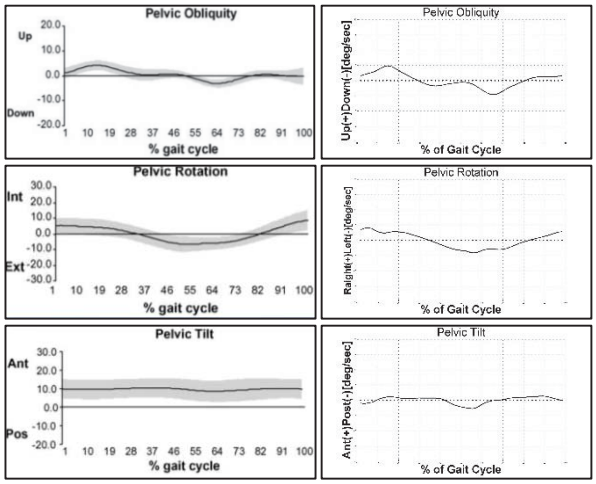

Fig. 8: Comparison of estimates of PK using a GAP (left) and GS (right)

3.5 Processing of Measured Data

To calculate the GP and inclination angles (PK) with GS the acceleration/gyroscopic signals, data refereed to few steps of a walking subject are taken into account.

Data originated from the GS are sent in real time to a computer using a Bluetooth 4.0 LE chipset, integrated into the device, and elaborated by codes written in Matlab (Mathworks, USA). To validate the system, gaits of some healthy subjects (males and females from 29 to 42 years, with weight ranging between 58 to 80 kg and height from 165 to 182 cm) were analysed. After the acquisition of data, GP of interest were

extracted. Table 2 shows the results compared with the mean values of anthropometric that are found in the literature.

Gait Paramiter	Stride length [m]	Velocity [m/min]	Cadence [step/min]	Gait Cycle [sec]	Stance Phase [%]	Swing Phase [%]	Double Support [%]	Single Support [%]
Mean Normal Values	1,46(±0,130)	77,4(±9,48)	52,8(±3,8)	1,14(±0,08)	60,31(±1,7)	39,6(±1,9)	9,4(±2,3)	41(±2)
#1	1,34	71,91	53,81	1,12	60,99	39,01	10,99	39,01
#2	0,96	53,55	55,81	1,08	61,33	38,37	11,54	38,41
#3	1,01	55,35	54,55	1,10	60,61	39,39	10,61	39,39
#4	1,52	78,74	51,95	1,16	64,94	34,85	15,15	34,85
#5	1,42	74,28	52,26	1,15	65,16	34,93	15,07	34,76
#6	1,47	77,46	52,86	1,14	64,98	35,02	14,98	35,02
#7	1,44	76,66	53,33	1,13	65,40	35,27	14,31	36,04
#8	1,43	75,60	52,86	1,14	66,22	34,63	15,42	34,57
#9	1,43	73,75	51,72	1,16	65,15	34,85	15,21	35,04
#10	1,57	81,69	52,02	1,15	63,87	36,13	13,87	36,13
#11	1,54	77,17	50,21	1,20	64,02	35,36	14,64	35,36
#12	1,36	72,48	53,25	1,13	62,13	36,69	13,31	36,69
Mean	1,37	72,39	52,89	1,14	63,73	36,21	13,76	36,27
Standard Deviation	0,1941161	8,8156373	1,447313865	0,030699	1,94801686	1,75060942	1,753178067	1,736255768

Table 2: Comparison of estimates of GP using GS on different subjects

4 Conclusions

In this paper, a low-cost waist worn IMU is developed. The results are encouraging and comparable to other handheld systems and waist mounted motion systems [15], [21]. Furthermore, the spatial-temporal GP and PK are reliable despite the simple and cheap instrumentation, so the GS can be exploited in various fields of human movement. In addition, because of its portability, GS can be used in other settings than a gait laboratory and therefore provides information that is more likely to reflect the actual performance of the subjects. The automatic and easy calculation of important spatial-temporal parameters, together with information about the pelvis kinematics make the GS system a clinical tool which allows a complete gait analysis without challenging clinical interpretation and expensive instrumentations. However, a further validation work will be performed, by comparing the GS system with a stereophotogrammetric unit and dynamometric platforms.

5 Acknowledgments

This work was developed thank to the financial support of the POSING project (CUP: G75C13000720007) of the Sicilia Region, Italy. The authors thank Dr. Marco Di Gesù and Dr. Angelo Vetro of the Centro Medico Mantia (Palermo, Italy) who have contributed to the acquisition and analysis of the data.

6 References

[1] Perry J. "Gait Analysis: Normal and pathological function". Thorofare, NJ SLACK Inc. 1, 1992.

[2] Nanhoe-Mahabier W, Snijders AH, Delval A, Weerdesteyn V, Duysens J, Overeem S, Bloem BR. "Walking patterns in Parkinson's disease with and without freezing of gait". Neuroscience 182:217-224, 2011

[3] Allen JL, Kautz SA, Neptune RR. "Step length asymmetry is representative of compensatory mechanisms used in post-stroke hemiparetic walking". Gait Posture, 33:538-543, 2011.

[4] Morris JRW. "Accelerometry- a technique for the measurement of human body movements". J Biomech; 6:729 - 36, 1973.

[5] Hayes WC, Gran JD, Nagurka ML, Feldman JM, Oatis C. "Leg motion analysis during gait by multi-axial

accelerometry: theoretical foundations and preliminary validations". J Biomech Eng; 105:283-9, 1983.

[6] Moe-Nilssen R. "A new method for evaluating motor control in gait under real-life environmental conditions". Part 2: gait analysis. Clin Biomech 1998; 13:32-35.

[7] Hirokawa S., Matsumara K. "Gait analysis using a measuring walkway for temporal and distance factors". Medical and Biological Engineering and Computing 25, 577–582, 1987.

[8] Abu-Faraj, Z.O., Harris, G.F., Abler, J.H., Wertsch, J.J. "A holter-type, microprocessor-based, rehabilitation instrument for acquisition and storage of plantar pressure data". Journal of Rehabilitation Research and Development 34, 187–194, 1997.

[9] Sparks D.R., Huang X., Higdon W., Johnson J.D., "Angular rate sensor and accelerometer combined on the same micromachined CMOS chip". In: Microsystem Technologies 4. Springer, Berlin, pp. 139–142, 1998.

[10] Yun X, Bachmann ER, Moore H, Calusdian J. "Self-contained position tracking of human movement using small inertial/magnetic sensor modules". IEEE International Conference on Robotics and Automation, 2526-2533, 2007.

[11] Aminian K., Robert Ph., Jequier E., Schutz Y. " Incline, speed, and distance assessment during unconstrained walking". Medicine and Science in Sports and Exercise 27, 226–234, 1995.

[12] Aminian K., Rezakhanlou K., De Andres E., Fritsch C., Leyvraz P.-F., Robert Ph., "Temporal features estimation during walking using miniature accelerometers: an analysis of gait improvement after hip arthroplasty". Medical and Biological Engineering and Computing 37, 686–691. 1999.

[13] Allen JL, Kautz SA, Neptune RR. "Step length asymmetry is representative of compensatory mechanisms used in post-stroke hemiparetic walking". Gait Posture, 33:538-543, 2011.

[14] van Dam MS, Kok GJ, Munneke M, Vogelaar FJ, Vliet Vlieland TP, Taminiau AHJ. "Measuring physical activity in patients after surgery for a malignant tumour in the leg. The reliability and validity of a continuous ambulatory activity monitor". Bone & Joint Surgery [Br], 83:1015-1019, 2001.

[15] F. Bugané, M.G. Benedetti, G. Casadio, S. Attala, F. Biagi, M. Manca, A. "Estimation of spatial-temporal gait parameters in level walking based on a single accelerometer: Validation on normal subjects by standard gait analysis". Computer Methods and programs in Biomedicine, Volume 108, Issue 1, Pages 129–137. October 2012.

[16] Zijlstra W, Hof AL. "Displacement of the pelvis during human walking: experimental data and model predictions". Gait Posture; 6:249 -62, 1997.

[17] Köse A., Cereatti A., Della Croce U.. "Bilateral step length estimation using a single". Journal of NeuroEngineering and Rehabilitation 9:9, 2012.

[18] Leardini A., Sawacha Z., Paolini G., Ingrosso S., Nativo R., Benedetti M.G.. "A new anatomically based protocol for gait analysis in children". Gait Posture. 26 (4), 560-71, 2007.

[19] Zijlstra W., Hof A. "Assessment of spatio-temporal gait parameters from trunk accelerations during human walking". Gait Posture 18, 1–10, 2003.

[20] Abdulrahim K., Chris Hide T., Hill C.. "Understanding the Performance of Zero Velocity Updates in MEMS-based Pedestrian Navigation". International Journal of Advancements in Technology, Vol. 5. N° 2, IJoAT 53-60, 2014.

[21] Tao W, Liu T, Zheng R, Feng H: "Gait analysis using wearable sensors. Sensors" 12:2255–2283, 2012.

[22] Buganè F., Benedetti M.G., D'Angeli V., Leardini A. "Estimation of pelvis kinematics in level walking based on a single inertial sensor positioned close to the sacrum: validation on healthy subjects with stereophotogrammetric system". Biomed Eng Online, V.13; 2014.

Algorithm Detecting Point Microcalcifications Using Matlab for Breast Cancer

Md. Shafiul Islam
Department of Electrical Engineering
University of North Dakota
Grand Forks, ND 58202
Email: md.s.islam@my.und.edu

Abstract- Goal of this research is to improve the capability of ultrasound images for detecting breast microcalcifications (MCs) and remove the major barriers of ultrasound for early breast cancer detection. The low detection rate of MCs with ultrasound is due to the low spatial resolution of the ultrasound images and to the presence of speckle noise, which masks the tiny microcalcifications. The first objective of this project is to investigate the efficiency of time reversal multiple signal classification (TR-MUSIC), algorithm in detecting breast microcalcifications and we did our experiments on numerical phantoms for detecting point microcalcifications and got the simulated results.

I. INTRODUCTION

Breast cancer is the most common nonskin malignancy in women and the second leading cause of female cancer mortality after lung cancer. Women in the United States have one of the highest incidence rates of breast cancer in the world, with about 1,665,540 new cases of breast cancer diagnosed in 2014 and 585,720 deaths happened in US [1]. Men are also affected by this disease. In 2014 about 2,360 new cases of invasive breast cancer was diagnosed among men in the United States [2]. Early detection is the major key to surviving this disease. The earliest indication of potential breast cancer detectable by current screening methods is the presence of microcalcifications (MCS). They are small crystal calcium apatite's that form in human tissue through a number of mechanisms, and that range in size up to several mm. They are the first sign of breast cancer in more than half of all breast cancer cases and they are sometimes the only indication of malignancy, making their detection critical. Ultrasound imaging is a non-ionizing technique and is a safer method for breast microcalcifications detection. However, current state-of-the-art clinical ultrasound imaging systems can only reliably detect tumors of at least several millimeters in size . This limitation is due mainly to their low-resolution, the presence of speckle noise in their images, phase aberration, and attenuation. Ultrasound has played a very important role for detecting microcalcifications for dense tissue and it has greater impact because non ionizing radiation, low cost, available and portability. Microcalcifications detection is affected by spatial resolution of the imaging system, speckle noise in the image and phase aberration. Proper arrangements of transducer elements are very important to get ultrasound images. To detect microcalcifications numbers of transducer elements have to be greater than the number of microcalcifications. For low number of transducer elements image artifact will appear which will increase the cost for adding filters to reduce these kind of artifacts like anti-aliasing image filters. To build the algorithm for microcalcifications detection we have to set proper value for transducer width, kerfs, pitch and element length. Without proper setting of this elements value we will get poor image resolution. Many techniques such as artificial neural networks (ANN) [3], linear discriminant analysis (LDA) [3], and support vector machine [4], [5] and Bayesian neural can be used for mass detection and classification [6]. These computer aided systems uses large amount of samples to construct models [7]. Using artificial neural network for mass detection and classification a multilayer feed-forward neural network can be used for classifier, extendibility, heftiness and consistency of the proposed computer aided algorithm. Multilayer neural network used for variance contrast and auto correlation contrast depending on input features corrected by back propagation error. Fuzzy logic also can be used for global and local information enhancement by avoiding noise amplification [8]. Using this technique edge and textural information can be extracted from ultrasound image and contrast ratio can be modified, computed and enhanced using this technique [8]. To enhance the ultrasound images defuzzification can be used [8]. Support vector machine normally used for differential analysis of breast microcalcifications detection [5]. In this process block difference of local correlation co-efficient, simplistic textural features block variation of converse probabilities and auto-covariance matrix is applied to detect microcalcifications [4]. Support vector machine is also used for image recognition, bioinformatics [4]. In trajectory based deformation rectification for ultrasound images classification of tissue deformation, pixel

dislocation assessment was performed among ultrasound images under different contact forces [9]. Information of contact force and the subsequent pixel displacements permitted the edifice of a trajectory field of subject beneath an ultrasound scan. Depending on the contact force pixel coordinates were plotted. Trajectory field and extrapolation algorithm was applied on each pixel-trajectory for rearranging the pixel to where it would have been without any contact force to get the tissue form [9]. Their apparition is inadequate by a number of factors including speckle noise, phase deviation, the system spatial resolution, attenuation, display parameters, and perception of human on the displayed image. If those limitations can be removed detection of microcalcification can be significantly improved. Depending on acoustic impedance of hydroxyapatite which is the most common element of microcalcification their amplitude reflection can be 0.9 inside tissue. So to get better resolution sub resolution model can be used to get bright reflector point under ultrasound. By increasing the aperture size resolution of the system can be increased. Using synthetic receive aperture imaging large aperture imaging can be reduced and which also reduces the system complexity associated with the imaging technique. Compared to single transmit aperture SRA system transmits into the same region of interest. When the sound wave is transmitted from the transducer echo signals are received in different sub aperture level. This signals are then added to create a large effective receive aperture and more channels are needed to receive signals in sub aperture level. The investigation of MC detectability is restricted by the reduced classification of their acoustic properties based on the theoretical radiation patterns of stiff and resilient spheres and clinically calculated speckle noise levels.

II. METHODOLOGY

To detect Point like targets using ultrasound image processing Multiple Signal Classification (MUSIC) has promising outcome [10]. To derive the equation for multiple signal classification (MUSIC) time reversal matrixes T and inter element transfer matrix can be used. Normally when transducer elements receives the back propagated waves from targets time reversal image is created [10]. In time reversal multiple signal classification coherent point spread function helps to get axial and lateral resolution. Time reversal matrix can be written as T=M*M where M is the multi-static response matrix [11]. Where Green function vector is orthogonal to noise subspace and eigen value is zero.

$$<\alpha_{m0},g^*_m>=<\alpha_{m0},g^*_m>0 \qquad 1$$

Here, m=1,2,3,...,M and m0=M+1,...,N, and α_{m0} is the eigen vector having zero eigenvalue [11].

Algorithm of pseudo-spectrum can be written as,

$$E(Y_p)= 1/\sum_{m0=M+1}^{n} | < \alpha m0 *, gp > |2$$

Where α_{m0} is the m_0'th eigenvector with zero eigen value.

$$g_p(\omega)=\{G(R_l,Y_p)\}=[G(R_1,Y_p), G(R_2,Y_p),...., G(R_N,Y_p)]^T \quad 3$$

Where $g_p(\omega)$ is the steering vector. For a test location Y_p steering vector can be found from green function vector. Because here signal subspace is orthogonal to the noise subspace and will disappear for test location Y_p becomes equal to reallocation of targets Y_m for non resolved as well as resolved targets. So pseudo spectrum E will rise towards infinity (theoretically) for each target location when $Y_p=Y_m$, m=1, 2, 3...M. Here equation (2) is multiple signal classification for time reversal imaging [11]. After defining variables for getting ultrasound images we have to do trace shaping for the desired images. For that we have to set image specification and process the ultrasound images for each element. After setting variables and other parameters for numerical phantoms we have to save the data in matrix to do further image processing for microcalcification detection.

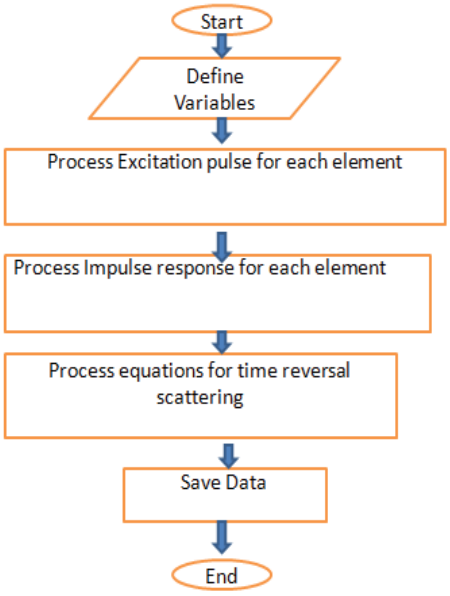

Fig.1. Flow chart for detection of microcalcifications.

Ultrasound images can be low in contrast. Preprocessing of the image reduces the noise and increases the contrast between the apprehensive areas and breast tissue background. We changed different parameters of ultrasound images to increase the image contrast to detect microcalcifications of numerical phantoms of the simulations. We used multiple signal classification algorithms for classifying the numerical phantoms for miocrocalcification detection [12]. Depending on the parameters selected in preprocessing level accuracy, sensitivity, specificity, positive predictive value, and negative predictive value are used to evaluate the classification results for

microcalcification for a specific region of interest for numerical phantoms. The higher the five measurements are, the more reliable and valid detection will be. We also experimented the receiver operating characteristic and parameter to evaluate the performances of the proposed approach.

III. RESULTS

We did our experiments on numerical phantoms to get simulated results. We did experiments for different sampling frequencies and sound speeds. For higher sampling frequencies point microcalcifications are more detectable than lower frequencies. We did our experiments for sampling frequencies 25MHz, 30MHzz, 35Mhz, 39MHz and 41MHz. It was found for sampling frequency 41MHz point microcalcifications are more detectable than other sampling frequencies.

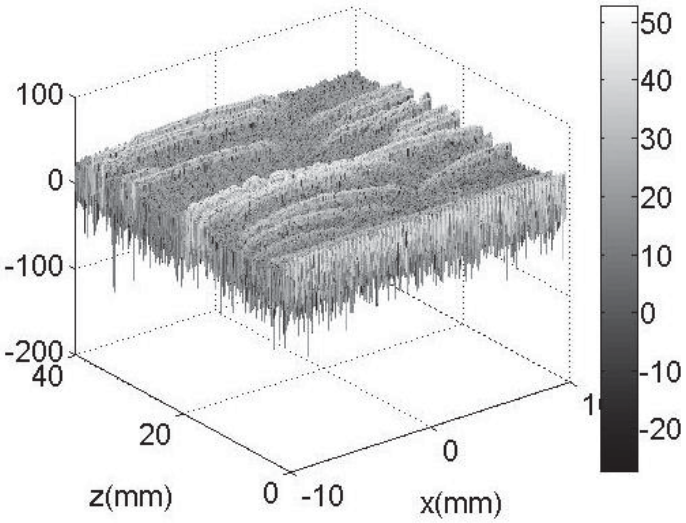

Fig.2 Detection of microcalcifications at 25MHz.

We gradually increased our sampling frequency from 25MHz to 41MHz to observe point microcalcifications become more detectable or not and to increase the precision level. For higher sampling frequencies we get less penetration but image resolution increases so point microcalcifications become more distinguishable. We can also vary the lateral and axial distance between the point scatters to change the wave length between them. In fig.4. sharp spikes of the reflected ultrasound waves distinguishes point microcalcifications more clearly.

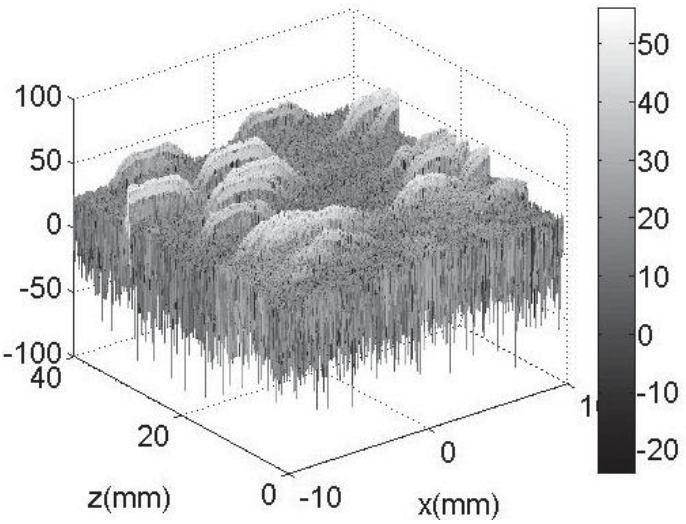

Fig.3. Detection of microcalcifications at 35MHz.

Distances between point scatters were decided depending on the wave length of the ultrasound frequency. When doing our simulated experiments using MATLAB we considered all the scatters is in one single plane.

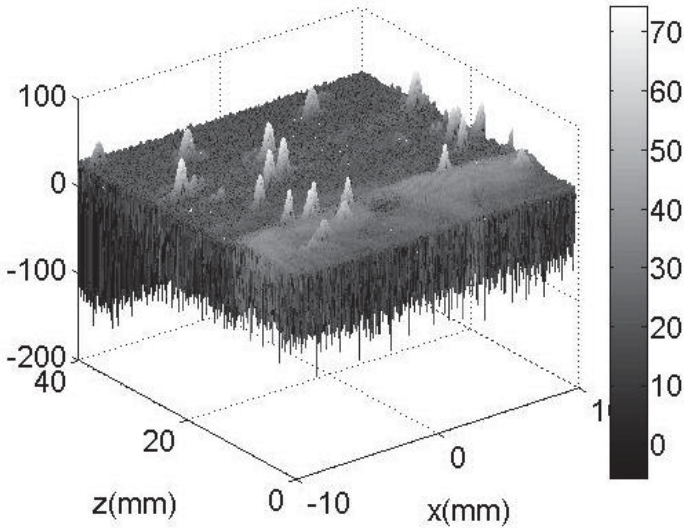

Fig.4. Detection of microcalcifications at 41MHz.

To get and measure ultrasound scatters signal Foldy-Lax [10] model was used. After processing the saved data for numerical phantoms we got the simulated results. Proper selection of sampling rate is very important when working with ultrasound images and without proper selection of sampling rate we will get poor image resolution. As our main purpose is to detect point microcalcifications of mm size, dimensions of simulated results in MATLAB is multiplied by 10^{-6}.

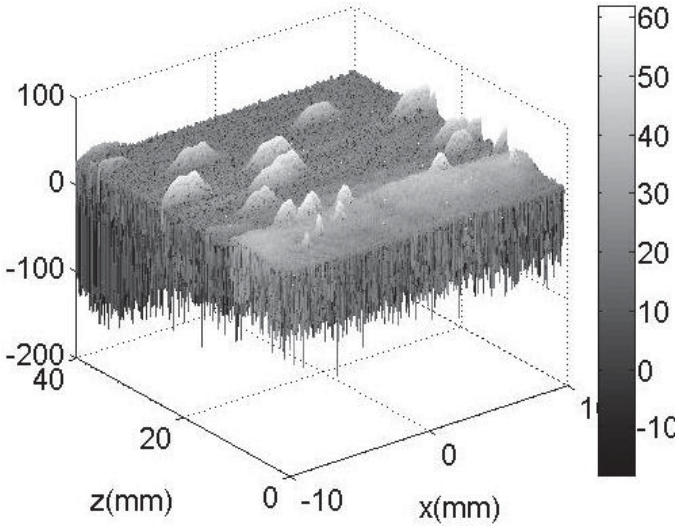

Fig.5. Detection of microcalcifications at 1380m/s.

In fig.4. we can see point microcalcifications are more distinguishable for sampling rate of 41MHz. But for sampling frequency 25MHz in fig.2. these point microcalcifications were more scattered. Without proper selection of sampling rate aliasing distortions occurs for frequency 25 and 35 MHz .When we increased and properly selected our sampling frequency that gives us the opportunity to detect point microcalcifications more precisely. Then we set out sampling frequency at 41MHz and varied the sound speed from 1380m/s to 1540 m/s. Because as we know inside human body velocity of sound wave varies from 1380m/s to 1540 m/s. Point microcalcifications were more scattered for sound speed 1380 m/s in fig.5. but in fig.6. those point microcalcifications were more distinguishable for sound speed 1540 m/s. After doing couple of experiments for different sampling rate and sound speed we found that best microcalcifications detection occurs at sampling rate 41MHz and sound speed 1540 m/s.

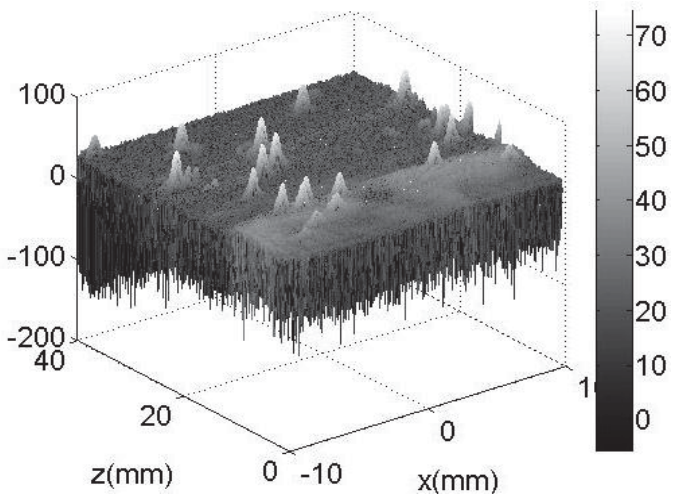

Fig.6. Detection of microcalcifications at 1540m/s.

When we were working with the numerical phantoms we observed that sound wave scattering from different microcalcifications sent from transducer elements also depends on proper selection of sound speed. Because when sound wave propagates through human body it's characteristics changes due human body tissue. In our experiments we observed when we selected sound speed at 1380m/s the image resolution of the simulated ultrasound images were poor. But when we gradually increased our sound speed from 1380m/s to 1540m/s then the image resolution got better.

IV. DISCUSSION

Proper selections of ultrasound parameters are very important to get better image resolution. Slight variations of these variables will cause poor image. Because of that we will not be able to detect microcalcifications which are very tiny in size. Proper selection of equations in algorithms is also very important when working with sound wave. In our experiments we were more concerned about the wave equation to characterize the sound wave property when moving through the human body. More transducer element will increase the image resolution but that will also increase the cost. More sampling rate also gives better image resolution but is also increases the complexity and cost of the system. So we have to make a trade of between the demand and requirement. Otherwise one of the main reasons for using ultrasound to detect breast microcalcifications will have no meaning.

V. CONCLUSION

We had some positive as well as negative outcomes when trying to develop our algorithm for numerical phantoms. We tried to analyze the negative results and also tried to find out possible reasons and solution for that. Such as depending on variation of sound speed ultrasound image resolution changes due change of characteristic of sound wave when interacts with body tissue. We also observed that for not choosing the proper sampling rate aliasing distortion occurs. Other factors like pulse width duration, excitation pulse, attenuation co-efficient and impulse response also creates changes on ultrasound image resolution of B-mode scanning. We tried to set proper value of these parameters to get better result for detection of microcalcifications in breast cancer. Finally, wave equation reflection imaging and factorizing method have outstanding impact for increasing the image resolution of ultrasound images for microcalcifications detection to detect early breast cancer. Image speckles can be reduced effectively by using wave equation for further image processing when analyzing the

received reflected or diffracted sound wave from different microcalcifications.

References

[1] *Breast Cancer Facts & Figures | American Cancer Society*.

[2] *U.S. Breast Cancer Statistics*.

[3] H. D. Cheng, J. Shan, W. Ju, Y. Guo and L. Zhang. Automated breast cancer detection and classification using ultrasound images: A survey. *Pattern Recognit 43(1),* pp. 299-317. 2010. . DOI: 10.1016/j.patcog.2009.05.012.

[4] N. Piliouras, I. Kalatzis, N. Dimitropoulos and D. Cavouras. Development of the cubic least squares mapping linear-kernel support vector machine classifier for improving the characterization of breast lesions on ultrasound. *Comput. Med. Imaging Graph. 28(5),* pp. 247-255. 2004. . DOI: 10.1016/j.compmedimag.2004.04.003.

[5] Y. Huang and D. Chen. Support vector machines in sonography: Application to decision making in the diagnosis of breast cancer. *Clin. Imaging 29(3),* pp. 179-184. 2005.

[6] D. Chen, R. Chang, C. Chen, M. Ho, S. Kuo, S. Chen, S. Hung and W. K. Moon. Classification of breast ultrasound images using fractal feature. *Clin. Imaging 29(4),* pp. 235-245. 2005.

[7] D. Chen, R. Chang and Y. Huang. Breast cancer diagnosis using self-organizing map for sonography. *Ultrasound Med. Biol. 26(3),* pp. 405-411. 2000.

[8] Y. Guo, H. Cheng, J. Huang, J. Tian, W. Zhao, L. Sun and Y. Su. Breast ultrasound image enhancement using fuzzy logic. *Ultrasound Med. Biol. 32(2),* pp. 237-247. 2006.

[9] S. Sun, B. W. Anthony and M. W. Gilbertson. Trajectory-based deformation correction in ultrasound images. Presented at SPIE Medical Imaging. 2010, .

[10] A. J. Devaney, E. A. Marengo and F. K. Gruber. Time-reversal-based imaging and inverse scattering of multiply scattering point targets. *J. Acoust. Soc. Am. 118*pp. 3129. 2005.

[11] A. J. Devaney. Super-resolution processing of multi-static data using time reversal and MUSIC. *J. Acoust. Soc. Am.* 2000.

[12] F. K. Gruber, E. A. Marengo and A. J. Devaney. Time-reversal imaging with multiple signal classification considering multiple scattering between the targets. *J. Acoust. Soc. Am. 115*pp. 3042. 2004.

[13] M. E. Anderson. The detection of breast microcalcifications with medical ultrasound *J. Acoust. Soc. Am. 101(1),* pp. 29. 1997. . DOI: 10.1121/1.417973.

[14] D. Chen, R. Chang, W. Kuo, M. Chen and Y. Huang. Diagnosis of breast tumors with sonographic texture analysis using wavelet transform and neural networks. *Ultrasound Med. Biol. 28(10),* pp. 1301-1310. 2002.

[15] L. Chen, Y. Chen, X. Diao, L. Fang, Y. Pang, A. Cheng, W. Li and Y. Wang. Comparative study of automated breast 3-D ultrasound and handheld B-mode ultrasound for differentiation of benign and malignant breast masses. *Ultrasound Med. Biol.* 2013.

[16] G. Clement, J. Huttunen and K. Hynynen. Superresolution ultrasound imaging using back-projected reconstruction. *J. Acoust. Soc. Am. 118*pp. 3953. 2005.

[17] B. E. Hashimoto. Sonography of ductal carcinoma in situ. *Ultrasound Clinics 1(4),* pp. 631-643. 2006.

[18] L. Huang, Y. Labyed, F. Simonetti, M. Williamson, R. Rosenberg, P. Heintz and D. Sandoval. High-resolution imaging with a real-time synthetic aperture ultrasound system: A phantom study. Presented at SPIE Medical Imaging. 2011.

[19] J. A. Jensen, S. I. Nikolov, K. L. Gammelmark and M. H. Pedersen. Synthetic aperture ultrasound imaging. *Ultrasonics 44*pp. e5-e15. 2006.

[20] B. Liu, H. D. Cheng, J. Huang, J. Tian, X. Tang and J. Liu. Fully automatic and segmentation-robust classification of breast tumors based on local texture analysis of ultrasound images *Pattern Recognit 43(1),* pp. 280-298. 2010. . DOI: 10.1016/j.patcog.2009.06.002.

[21] E. A. Marengo, F. K. Gruber and F. Simonetti. Time-reversal MUSIC imaging of extended targets. *Image Processing, IEEE Transactions on 16(8),* pp. 1967-1984. 2007.

[22] P. M. Morse and K. U. Ingard. *Theoretical Acoustics* 1968.

[23] I. Reiser, R. Nishikawa, A. Edwards, D. Kopans, R. Schmidt, J. Papaioannou and R. Moore. Automated detection of microcalcification clusters for digital breast tomosynthesis using projection data only: A preliminary study. *Med. Phys. 35(4),* pp. 1486-1493. 2008.

[24] A. P. Sarvazyan, M. W. Urban and J. F. Greenleaf. Acoustic waves in medical imaging and diagnostics. *Ultrasound Med. Biol.* 2013.

[25] C. M. Sehgal, S. P. Weinstein, P. H. Arger and E. F. Conant. A review of breast ultrasound. *J. Mammary Gland Biol. Neoplasia 11(2),* pp. 113-123. 2006.

[26] Y. Su, H. Wang, Y. Wang, Y. Guo, H. Cheng, Y. Zhang and J. Tian. Speckle reduction approach for breast ultrasound image and its application to breast cancer diagnosis. *Eur. J. Radiol. 75(1),* pp. e136-e141. 2010.

[27] C. J. Vyborny, M. L. Giger and R. M. Nishikawa. Computer-aided detection and diagnosis of breast cancer *Radiol. Clin. North Am. 38(4),* pp. 725-740. 2000. . DOI: 10.1016/S0033-8389(05)70197-4.

ERP analysis of emotional stimuli from brain EEG signal

Raja Majid Mehmood[1] and Hyo Jong Lee[1, 2, *]

[1] Division of Computer Science and Engineering
[2] Center for Advanced Image and Information Technology
[*]Corresponding author
Chonbuk National University, Jeonju, SOUTH KOREA
rmeex07@gmail.com, hlee@chonbuk.ac.kr

Abstract - *The main objective of our study is to analyze the event related potential (ERP) of EEG brain signal from different emotional responses. An affective picture simulation was designed to find out neurophysiological characteristics of EEG brain signal. Event oriented EEG dynamics in ERP were analyzed statistically by using the one-way ANOVA method ($p<0.01$). Twenty one healthy college students were employed in this experiment. We used the standard IAPS database for picture's simulation. These affective pictures were further classified in four emotional classes. They are happy, calm, sad, and scared. The results shown that, there were the differences of stimulus response at the frontal region of the brain between the 1000ms and 1200ms. However, we also found the early ERP which is P300 at occipital and parietal regions of the brain.*

Keywords: *ERP, LPP, EEG, Emotion Recognition*

1 Introduction

Emotion is the result of mental activity in the brain [1]. It has become a significant in neuroscience due to comprehension of human cognition and neural processes associated with psychopathology [2]. However, many researchers have investigated various kinds of physiological phenomena. Therefore, EEG is considered to be an interesting study area for the detection of the affective state. In recent years, increasing interest has been focused on the brain computer interface (BCI) application, which combined with emotion perception and regulation of humans. In the emotion recognition researches, Event Related Potential (ERP) analysis is the useful way to investigate the emotional information from EEG signals.

In this paper, four emotions were examined by ERP analysis. Emotions were induced in subjects by presentation of different affective stimuli. ERP analysis used in many studies about emotion recognition [3]. These researches were focused on the brain dynamics elicited while subjects were watching the emotional stimuli. There has been extensive research is going on using early ERPs to study the emotion recognition of the brain EEG signals. Mostly, ERP studies focused on mean amplitude differences. It is an activity of interest, which is evoked by the stimulus in every trial.

There are two different kinds of concepts in ERP analysis. The first kind of ERP affects produced in early processing, which is about the 300 milliseconds timeframe. It is also known as P300 which reflects the initial attention captured by an emotional stimulus. The other type of ERP is a late processing that is driven by the motivational relevance of stimulus, and it could be induced with memory encoding and elaboration of affective stimulus [4]. The late positive potential (LPP) is a key component of any ERP analysis. It is modulated by the emotional stimulus. The modulation is identified after 400ms and continue for up to one second following the stimulus [5]. The study of LPP has become more and more popular in the emotion recognition research.

Schupp et al. explored that the high and low valence stimulus can induce a high LPP than middle-valence stimulus [5]. Keil et al. [6] proved similar results as found mentioned by Cuthbert. Weinberg et al. also proposed that the arousal stimulus elicit a higher LPP than low arousal stimulus [7]. LPP was applied in many research areas [8, 9], which used to index the abnormal emotional behavior. For example, LPP was used to explore the meditation [10], searching the social biases for in-group or out-group classification [11], and lie-detector testing [12]. Schupp et al. found the higher LPP amplitude that shows the significance of emotional stimuli [5]. Furthermore, the LPP is very reliable over time within individuals [13]. In this paper, we aimed to find out the P300 and LPP for the emotion recognition with visual stimuli. We would expect the obvious response of different emotional changes in the specific time range for the visual stimuli. Further, we explained the Material and Methods in Section-2. Section-3 contained the Result and Discussion of our experiment. Finally, we presented the conclusion of this paper in Section-4.

2 Material and Methods

The purpose of this experiment is to induce the emotional reaction in human subject during the visual simulation. We adopted the International Affective Picture System (IAPS) in this research. IAPS is a two dimensional picture database in arousal and valence domain [14, 15]. We selected the four emotional states in our analysis such as, happy, scared, calm and sad. We chose 180 stimuli (45 stimulus x 4 states) from equally distributed groups along the arousal-valence axes in IAPS database.

The EEG signals were recorded through Emotiv-EPOC headset. It included 14 EEG channels with 2 reference channels. These channels were placed according to the international 10/20 electrode placement. The sampling rate of this device is 128 samples per seconds (SPS). The following Fig. 1 shows the EEG electrodes placement in our experiment.

In this paper, we are presenting the results of 21 subjects which are divided by 09 male and 12 female subjects. All subjects were students of the same middle school, and their average age was 13 years. The brief introduction and presentation were given to them which include the stages of experiment. We also took the consent forms after the presentation of our experiment

We recorded the EEG signal data of each subject. The emotional picture was presented randomly for 1500ms following another 500ms with a blank image. This procedure continued for whole session. The blank image was useful to release the emotional activity of a subject which was elicited due to previous picture. We presented a cross window for four seconds at start and end each training session. The duration of this training session is about 368 seconds for every subject.

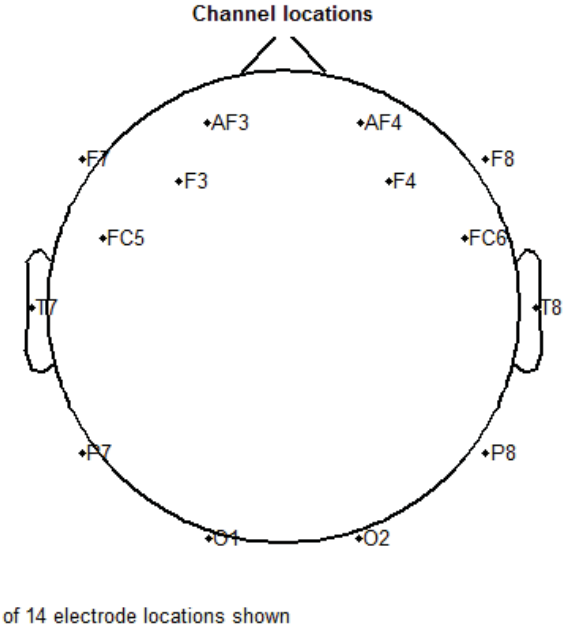

Fig. 1. Emotiv-EPOC headset 14 channel placement

The recorded EEG brain signal were processed in EEGLAB toolbox which belongs to SCCN Lab [16]. This toolbox is running on the Matlab platform. We preprocess the brain EEG data of each subject with help of Independent Component Analysis (ICA). We also performed a manual rejection of artifacts such as, eye blinks, eye movement, muscle movement, and bad channel, etc. Furthermore, we processed the EEG signal through band pass filtering with low and high filters which are 0.5 and 30 Hz, respectively.

We used 14 electrodes for recoding our experiment such as, AF3, F7, F3, FC5, T7, P7, O1, O2, P8, T8, FC6, F4, F8, and AF4. We adopted the brain region's oriented approach to analyze the ERP. Therefore, we were named the EEG channels according to their spatial location. We defined total of six brain regions, which are anterior-frontal (AF3 and AF4), frontal (F7, F3, F4, F8), frontal-central (FC5 and FC6), temporal (T7 and T8), parietal (P7 and P8) and occipital (O1 and O2). We employed the One-way repeated measures ANOVA for ERP analysis of selected emotional classes. The ANOVA method indicated the discriminative emotional classes at given timeline, where it satisfies the condition of p-value (0.01).

3 Result and Discussion

For ERP analysis, the continuous brain EEG data was segmented for epochs of 2000ms. This timeline contained the baseline that was starting from 500ms prior to stimulus onset. The vertical and horizontal axes in the graph stand for the values of potential and the time of the specified latencies respectively. Here, we are interested to analyze the whole timeline to see the P300 and LPP. The amplitude of the ERP is computed through the averaging of all subjects for each channel. The mean amplitude values of ERP were calculated for the four emotional states, separately. The grand average ERP elicited from four emotional stimuli is presented on the Fig. 2. As these figures can be shown, differences in the four emotion waveforms started around the timeline after stimulus onset. Fig. 2 (b) shows the ERP analysis under the frontal brain region. Furthermore, statistical analysis revealed the significant time range between 1000ms and 1200ms. However, Fig. 2 (a), (b) and (c) shown the LPP between 800ms and 1000ms under the anterior-frontal, frontal and frontal-central regions, respectively. We also presented the P300 in Fig. 2 (d) and (e) under the occipital and parietal regions, respectively. Fig. 2 (f), we can see the N200 and LPP under the temporal region of the brain.

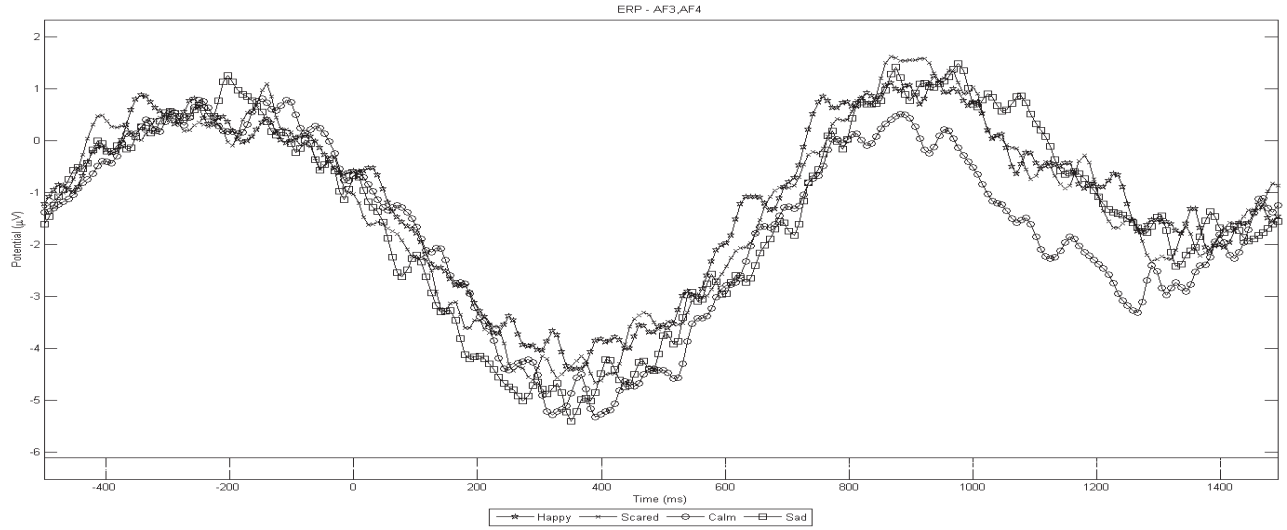
ERP - AF3,AF4
Potential (μV)
Time (ms)
Happy
Scared
Calm
Sad

(a)

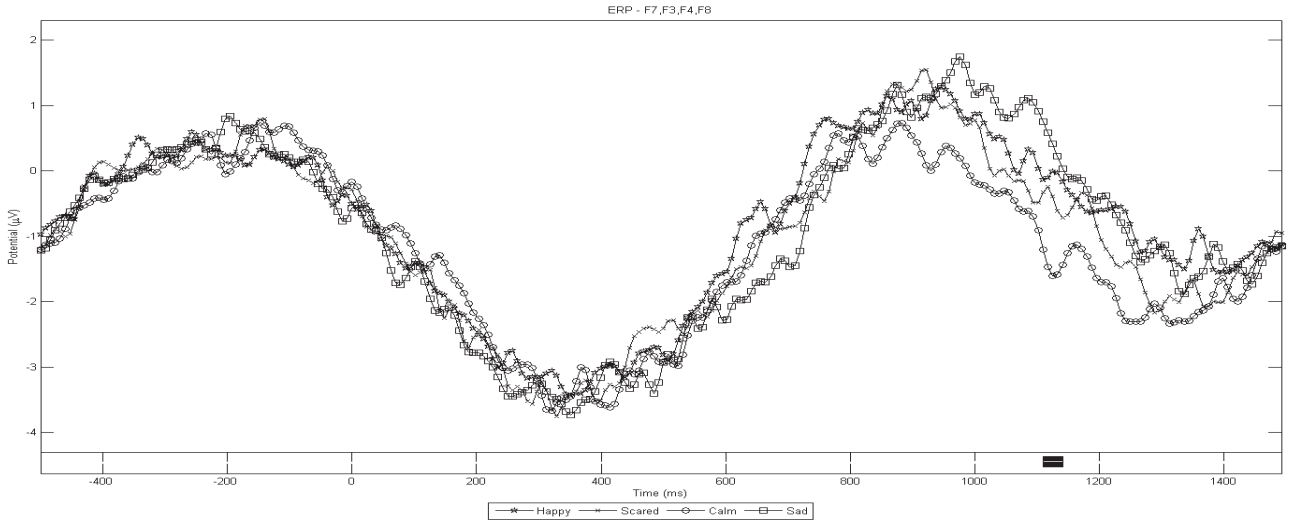
ERP - F7,F3,F4,F8
Potential (μV)
Time (ms)
Happy
Scared
Calm
Sad

(b)

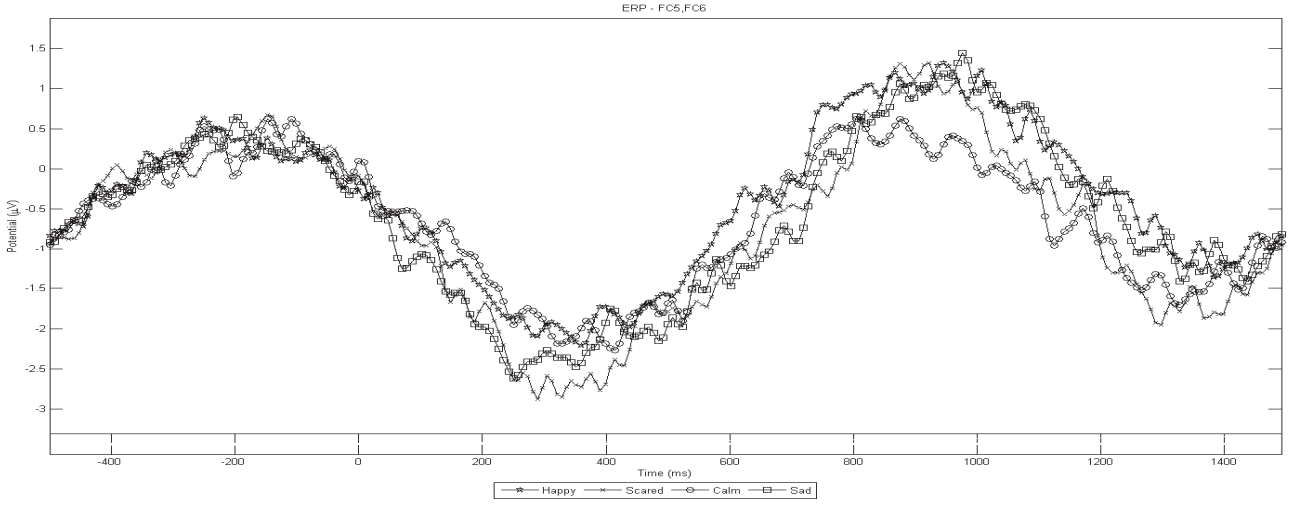
ERP - FC5,FC6
Potential (μV)
Time (ms)
Happy
Scared
Calm
Sad

(c)

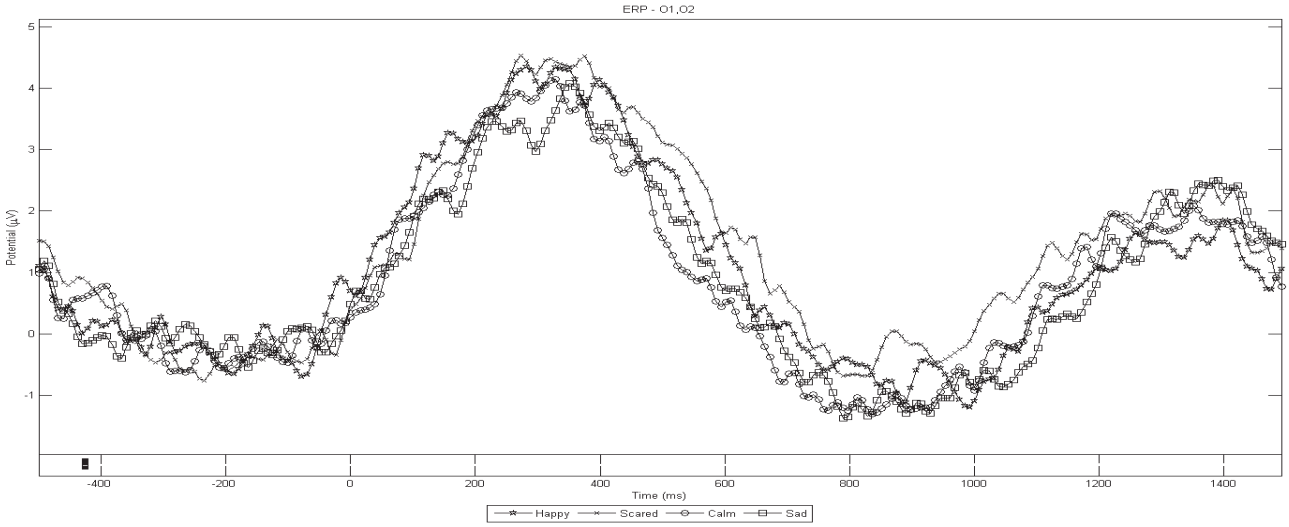

(d)

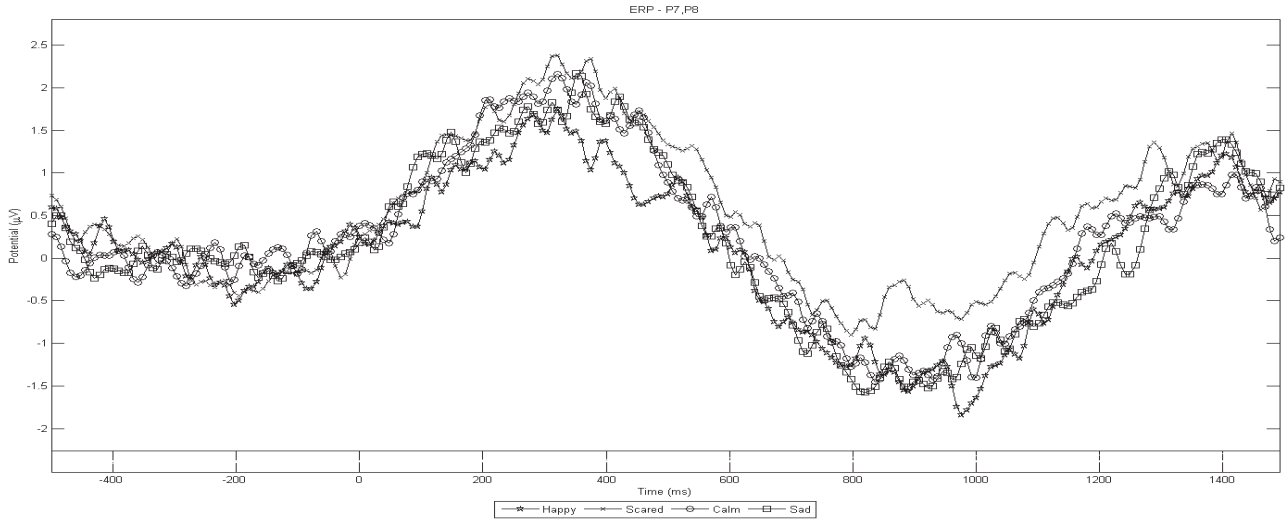

(e)

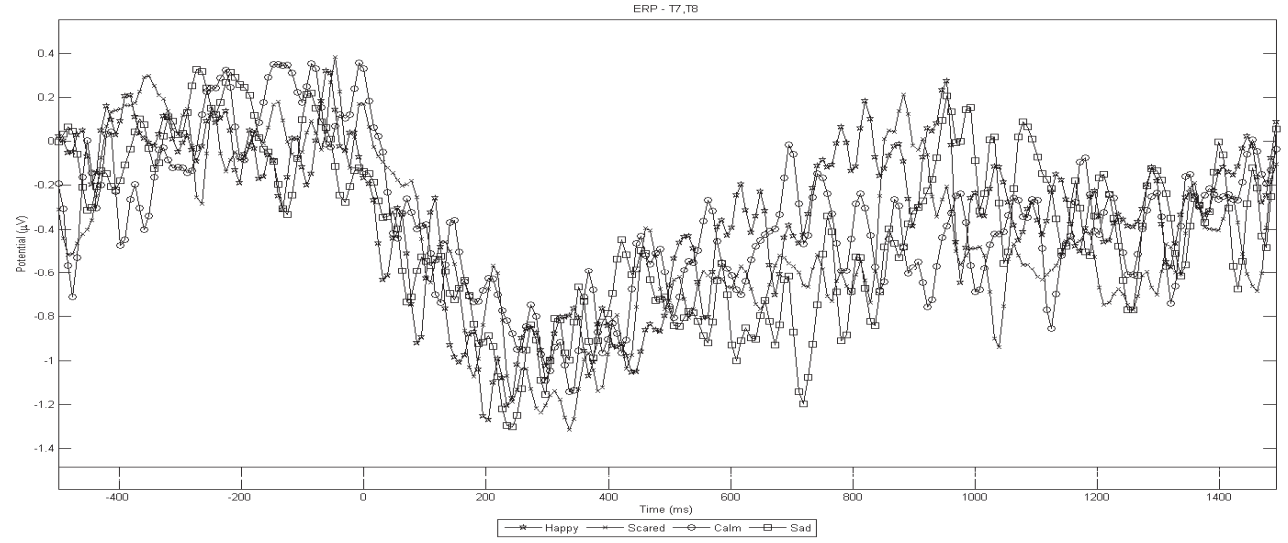

(f)

Fig. 2. ERP analysis in six brain regions

4 Conclusions

In this paper, we investigated activity changes according to various emotional stimuli. Four affective states (happy, scared, calm, and sad) were simulated with the IAPS picture database. ERP were calculated and revealed over the whole brain region. However, every region shows either P300 or LPP on changing of emotional stimulus. The potential difference was found in the different regions, where emotional changes were dominant. The strong response of LPP was occurred in the anterior-frontal, frontal, and frontal-central regions. Furthermore, parietal and occipital regions were indicated the P300 for all emotions. In addition, there were the N200 and LPP at the temporal region of this brain. In the future, the more subjects will be added to experiment to enhance the statistical results.

Acknowledgement

This work was supported by the National Research Foundation of Korea (NRF) grant funded by the Korea government (MEST) (No. 2012R1A2A2A03).

References

[1] J. Panksepp, *Affective neuroscience: The foundations of human and animal emotions*: Oxford university press, 1998.

[2] J. M. Spielberg, J. L. Stewart, R. L. Levin, G. A. Miller, and W. Heller, "Prefrontal cortex, emotion, and approach/withdrawal motivation," *Social and personality psychology compass,* vol. 2, pp. 135-153, 2008.

[3] J. K. Olofsson, S. Nordin, H. Sequeira, and J. Polich, "Affective picture processing: an integrative review of ERP findings," *Biological psychology,* vol. 77, pp. 247-265, 2008.

[4] M. Codispoti, V. Ferrari, and M. M. Bradley, "Repetition and event-related potentials: distinguishing early and late processes in affective picture perception," *Journal of Cognitive Neuroscience,* vol. 19, pp. 577-586, 2007.

[5] H. T. Schupp, T. Flaisch, J. Stockburger, and M. Junghöfer, "Emotion and attention: event-related brain potential studies," *Progress in brain research,* vol. 156, pp. 31-51, 2006.

[6] A. Keil, M. M. Bradley, O. Hauk, B. Rockstroh, T. Elbert, and P. J. Lang, "Large-scale neural correlates of affective picture processing," *Psychophysiology,* vol. 39, pp. 641-649, 2002.

[7] A. Weinberg and G. Hajcak, "Beyond good and evil: the time-course of neural activity elicited by specific picture content," *Emotion,* vol. 10, p. 767, 2010.

[8] T. A. Dennis and G. Hajcak, "The late positive potential: a neurophysiological marker for emotion regulation in children," *Journal of Child Psychology and Psychiatry,* vol. 50, pp. 1373-1383, 2009.

[9] W. P. Horan, J. K. Wynn, A. M. Kring, R. F. Simons, and M. F. Green, "Electrophysiological correlates of emotional responding in schizophrenia," *Journal of abnormal psychology,* vol. 119, p. 18, 2010.

[10] A. Sobolewski, E. Holt, E. Kublik, and A. Wróbel, "Impact of meditation on emotional processing—a visual ERP study," *Neuroscience research,* vol. 71, pp. 44-48, 2011.

[11] E. Hurtado, A. Haye, R. González, F. Manes, and A. Ibáñez, "Contextual blending of ingroup/outgroup face stimuli and word valence: LPP modulation and convergence of measures," *BMC neuroscience,* vol. 10, p. 69, 2009.

[12] I. Matsuda, H. Nittono, A. Hirota, T. Ogawa, and N. Takasawa, "Event-related brain potentials during the standard autonomic-based concealed information test," *International Journal of Psychophysiology,* vol. 74, pp. 58-68, 2009.

[13] M. Codispoti and A. De Cesarei, "Arousal and attention: Picture size and emotional reactions," *Psychophysiology,* vol. 44, pp. 680-686, 2007.

[14] P. J. Lang, M. M. Bradley, and B. N. Cuthbert, "International affective picture system (IAPS): Instruction manual and affective ratings," *The center for research in psychophysiology, University of Florida,* 1999.

[15] M. Bradley and P. J. Lang, *The International affective digitized sounds (IADS)[: stimuli, instruction manual and affective ratings*: NIMH Center for the Study of Emotion and Attention, 1999.

[16] A. Delorme and S. Makeig, "EEGLAB: an open source toolbox for analysis of single-trial EEG dynamics including independent component analysis," *Journal of neuroscience methods,* vol. 134, pp. 9-21, 2004.

Cardiovascular Authentication: Fusion of Electrocardiogram and Ejection Fraction

Rabita Alamgir[a], Obaidul Malek[a], Laila Alamgir[b], and Mohammad Matin[c]

Center for Biometrics and Biomedical Research[a], Howard University[b], and University of Denver[c]

Abstract

The most advanced scientific development of biometrics will be to uniquely identify an individual based on their clinically used cardiac physiological and anatomical attributes. Research studies have demonstrated in particular the potential of cardiovascular activity as a biometric marker. Electrocardiogram (ECG) signals and left ventricular Ejection Fraction (EF) measured via echocardiography are relatively unique to an individual. But, the viability of left ventricular ejection fraction hasn't yet been demonstrated as a biometric marker. This paper proposed a novel method to authenticate a human identity based on the analysis of data received from these two modalities of cardiovascular activities. In this method, the fusion of ECG and EF as a biomedical marker has been used to authenticate an individual. The performance of this method has been tested based on the Equal Error Rate (EER). Experimentation demonstrated the superiority of this fusion method in comparison to the monomodal EGC system.

Keywords: *Biometric authentication, correlation, ECG, ejection fraction, and fusion.*

1. Introduction

Biometric approaches have been researched extensively due to the need for reliable security systems in modern facilities. For example, one of the most important healthcare delivery issues that can jeopardize patient privacy, safety, and quality of care is the correct identification of patients and healthcare providers. In modern society, there is a greater need for biometric recognition – the use of a personal feature to determine human identity.

Traditional monomodal biometric modalities have been previously employed with varying degrees of success, including fingerprints, face, iris, voice, and gait. According to Riera et al. [1], an ideal biometric feature should be applicable to every individual. Furthermore, it should be quantitatively measurable, highly efficient, reliable, and invariable over a long period of time. Although many biometric modalities meet several of these criteria, there are drawbacks to their use, especially since they are vulnerable to falsification. Medical biometrics, in contrast, consists of recognition methods that incorporate signals used in clinical diagnostics and is more robust to circumvention and spoofing attacks. In addition, medical biometrics can provide continuous recognition, which is the case with cardiac biometrics.

Previous research [2], however, has demonstrated the viability of using cardiovascular function to identify individuals. Naturally, cardiac signals measure vitality and are less vulnerable to forgery, given that they are unique to individuals. Cardiac activity generates signals in many energy forms, and each signal can be quantified by a particular measurement technique. The method proposed in this paper aims to combine two noninvasive modalities of cardiodynamics for use in biometric recognition: electrocardiogram (ECG), and ejection fraction (EF). The performance of the proposed method has been evaluated using the Equal Error Rate (EER). Experimentation demonstrates that the fusion of these modalities can yield better authentication performance.

2. Electrocardiogram

As an electrical modality, the electrocardiogram (ECG) is a representation of signals from the activity of the heart over time. The ECG is recorded by attaching electrodes to an individual and measuring the electrical voltage between a pair of leads [3]. Depolarization spreads from the atria down through the interventricular septum and to the ventricles. When the wave of depolarization travels toward a recording lead, it results in a positive or upward deflection. When the wave travels away from the lead, it results in a negative or downward deflection.

In clinical practice, the ECG uses 12 different recording leads, though only 10 recording electrodes on the skin are required to determine the direction of the leads. In fact, previous ECG studies have employed single-channel ECG signals, given that Biel et al. [2] showed that a single channel contains adequate data to support biometric recognition. The proposed study utilizes one-channel signals recorded from the palms; a methodology for data collection that was demonstrated to be comparatively efficient and capable of collecting biometric features to uniquely verify an individual [4].

Biometric authentication involves preprocessing, feature extraction, and classification. The preprocessed ECG trace would then be segmented into non-overlapping windows. Many feature extraction and reduction methods have been suggested for use in ECG recognition. A typical ECG waveform is shown in Fig. 1, which consists of a P-wave, a QRS-complex, and a T-wave. Even with this general form, ECG signals vary across individuals and contain highly personalized information.

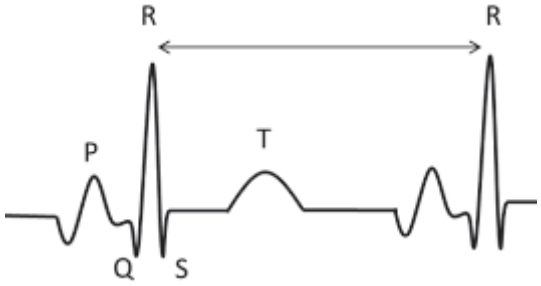

Figure-1: Complete cycle of a cardiac signal.

In data collection, there are various artifacts that may corrupt these signals. Due to the time dependent nature of ECG, noise with frequency content often overlaps with ECG signals and must be preprocessed. Digital filters, particularly Finite Impulse Response (FIR) filters based on several windows, can remove artifacts such as power line interference, electrode contact noise, baseline drift, and electromyography noise. According to Chandrakar et al. [5], when compared with Infinite Impulse Response (IIR) filters, FIR filters are more stable and efficient.

The proposed method employed preprocessing in a filtering step using the FIR filter of order 300 with the Kaiser Window. Mbachu et al. [5] previously designed the Kaiser Window high-pass filter for removal of low frequency noise like baseline wander and the notch filter for removing power line frequency noise. In a similar way, the current study's first step would employ FIR with a high pass filter cutoff frequency of 0.5 Hz based on the window [6]. The step would remove baseline drift noise, caused by variations in the position of the heart and electrodes, and by changes in the propagation medium. The second step would remove 60-Hz power line interference by band stop. Muscle contractions may also generate noise in the form of detectable depolarization and repolarization waves. For this reason, in the third step, the electromyography noise would be removed by applying a low pass filter with a cutoff frequency of 100Hz [7]. The first and last heartbeats of the noise-reduced records are deleted to get full heartbeat signals. Then, temporal and amplitude distance measurement methodologies between

fiducial points are implemented [8]. Finally, the amplitude of two consecutive R waves (Fig. 1), the time interval, and the heartbeat rate within that interval are calculated and recorded as a biometric feature.

3. Determination of EF

The recognition performance of other monomodal cardiac biometric systems has been comparable to those from many ECG recognition studies [9]. Measurement of cardiac output has not received sufficient attention in biometric research due to the relative ease of acquiring other electrophysiological information on cardiac activity and the inability to define a noninvasive, accurate measure of cardiac function.

A measurement that clinicians use is ejection fraction (EF), which has not been previously investigated as a biometric marker. In clinical practice, EF serves as a mechanical measurement for cardiac output and left ventricular (LV) contractility. EF is a simple and familiar measurement that can repeatedly determine the cardiac output pattern and is relatively constant over time [10].

Fundamentally, EF is the percentage of blood that is ejected from the ventricle during systole, obtained by dividing the volume ejected by the left ventricle (stroke volume) by the volume of the filled heart (total end-diastolic volume). Normal ejection fraction is above 50% and does not tend to vary across the same individual, assuming he or she does not have cardiac irregularities. If the individual did have an abnormal EF, they would have had uncharacteristic results during the ECG step as well. Most healthy individuals should have an ejection fraction between 50 and 70%, but this ratio depends on Stroke Volume (SV) and Diastolic Volume (DV). Both of these quantities are expected to be unique to an individual. The EF system is shown in Fig.-2.

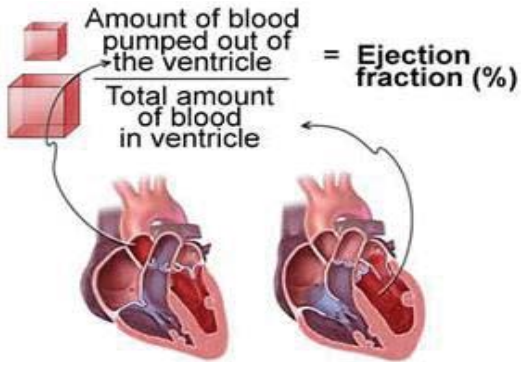

Figure-2: Left ventricular ejection fraction.

A 2-D echo is used to visualize real-time motion of the heart structures, while a Doppler echo is used to measure and assess the flow of blood through the heart's chambers and valves. First, the left ventricular outflow tract (LVOT) diameter would need to be measured on a parasternal long axis view of the heart to find the LVOT cross sectional area (CSA) in cm^2. Then, the LVOT Velocity Time Integral (VTI) can be calculated by the machine through an apical 5-chamber view of the heart. These measurements would be taken repeatedly to reduce sampling bias. The stroke volume (SV) at the LVOT is obtained by multiplying the LVOT VTI with the LVOT CSA. The end-diastolic volume (EDV) can be calculated using the LV end-diastolic diameter. Lastly, EF can be calculated when dividing SV by EDV as stated in Eq. 1 [10].

$$\frac{SV}{DV} .100 \quad \text{.....(1)}$$

4. ECG and EF Correlation

A heart's pumping process is an electro-mechanical system. Electrical activity measured by the ECG causes relaxation or contraction of the heart. Mechanical activity measured by echo directly impacts the electrical activity of the heart with changes in blood pressure and volume [9-10]. Though ECG and EF via echo utilize different signal types, they both measure heart efficiency. With ECG, the focus is on whether the heartbeat pattern is normal, too fast, or too slow, or determining whether the heart has physical abnormalities; even in clinical practice, it is usually the initial test. Nevertheless, an ECG cannot assess the pumping ability of the heart, so an echo is used to measure the shape and size and evaluate valvular functioning, along with hemodynamics. ECG combined with echo can raise the accuracy of diagnostic tests into the 80th percentile, so the combined system may have applications in identifying individuals.

The systems are proportional and related mathematically. Ejection fraction is a measure of cardiac output, which is the volume ejected by the ventricle per minute and is the product of stroke volume and heart rate. While one might calculate cardiac output, heart rate, and EF through echo, heart rate can also be determined from the R-R interval (or cycle length) in the ECG signal [9-11]. This interval denotes the time elapsed from one R-wave to the next, which indicates the electrical activation of the ventricles [3]. Thus, the results of an EF calculation from echo should reinforce the R-wave observation in the ECG and be sufficient to uniquely identify an individual.

5. Fusion of ECG and EF

In this paper, two measures of cardiovascular activity, ECG and EF, have been investigated individually for their utility as biometrics and when combined. Although the performance of ECG as a biometric is well-established based on previous studies [2], no study has yet demonstrated the viability of left ventricular ejection fraction via echocardiography as a biometric feature. Combining electrical (ECG) and mechanical (echo) features for cardiovascular activity would enhance authentication performance and is thus expected to be an improvement over an individual biometric system. Consequently, this is a unique and novel method for implementing EF as a biometric trait, especially fusing the ECG signal with the EF in order to enhance the authentication accuracy.

In this method, the authentication performance of each system has been evaluated separately. Then, the performance of the multibiometrics system (i.e. fusion of ECG and EF) has been evaluated using equal error rate. Since ECG and echocardiography have different morphologies, it may be a challenge to complete fusion at the decision level. Therefore, fusing the two biometric modalities at the score-level has been used as a cardio multibiometrics authentication system [9-12].

6. Results and Discussion

In this paper, fusion of ECG and EF cardiac biometric features at the score level has been implemented. The ECG (signals) features have been taken from the "MIT-BIH" database [13], and a simulated database has been created for the EF cardiac features. Therefore, there is no relationship between the individual used to create the database of ECG signals and the data in the EF database. In this case, a set of simulated EF data has been assigned to a specific individual in the ECG database, and the fusion of ECG and EF at the score level (matching process) has been implemented to authenticate an individual's identity. The performance of the verification has been evaluated based on the False Acceptance Rate (FAR), False Rejection Rate (FRR), and Equal Error Rate (EER). The results are recorded and the performance evaluation curve is presented in Table-1 and Fig.-3 respectively. In this experiment, an EER of 6.80% and FAR of 5.45% at the cost of an FRR of 6.5% have been achieved using the proposed fusion method.

Table-1:

Methods	FAR (%)	FRR (%)	EER (%)
ECG Signals	8.90	9.25	8.75
Fusion of ECG and EF	5.45	6.50	6.80

7. Conclusions

It is common for ECG to be accompanied by echocardiograms in healthcare settings. Reading the ECG graph while observing the motion of the heart via echo gives clinicians a complete picture of heart activity. Previous studies have demonstrated the utility of ECG as a biometric [2] but not the potential of echocardiography and ejection fraction. This paper investigated the fusion of two cardiovascular signal types based on the distinct but correlated features at the score level. It is found that the performance of the proposed mutibiometrics cardiac method (fusion of ECG and EF) outperforms its monomodal ECG counterpart..

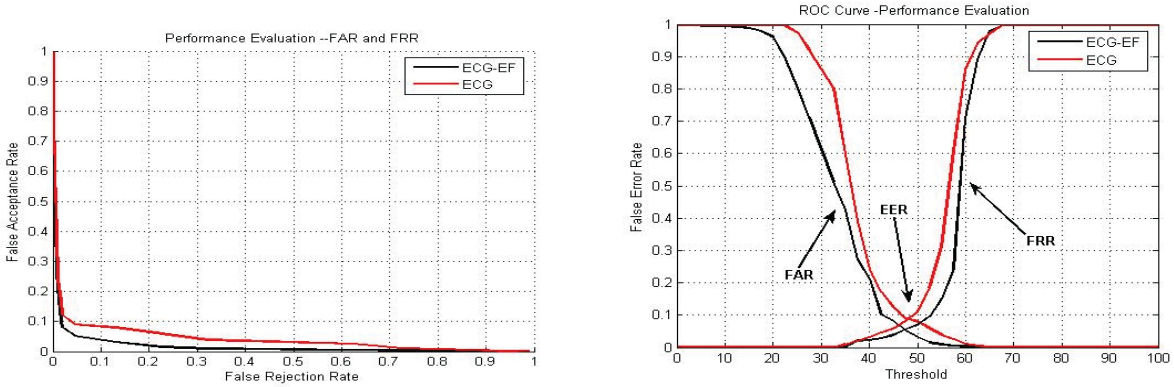

(a) FAR and FRR (b) ROC curve

Figure-3: Verification process -performance evaluation.

References

[1] A. Riera, A. Soria-Frisch, M. Caparrini, I. Cester, and G. Ruffini, "Multimodal physiological biometrics authentication. b*iometrics: Theory, Methods, and Applications"*, pp. 461-482, 2009.

[2] L. Biel, O. Petterson, L. Phillipson, and P. Wide, "ECG analysis: a new approach in human identification", *IEEE Transactions on Instrumentation and Measurement*, vol. 50(3), pp. 808–812, 2011.

[3] M. Gertsch, *The ECG manual: an evidence-based approach,* Springer Science and Business Media, 2008.

[4] W. Shen, J. Tompkins, and H. Hu, "One-lead ECG for identity verification", IEEE-Conference on Engineering in Medicine and Biology, vol. 1, 2002.

[5] B. Chandrakar, O. Yadav, and K. Chandra, "A survey of noise removal techniques for ECG signals", *International Journal of Advanced Research in Computer and Communication Engineering*, vol. 2(3), pp. 1354-1357, 2013.

[6] B. Mbachu, N. Onoh, E. Idigo, N. Ifeagwu, and U. Nnebe, "Processing ECG signal with Kaiser Window-based FIR digital filters", *International Journal of Engineering Science and Technology*, 3(8), pp. 6775-6783, 2011.

[7] J. Rao and A. Usharani, "Enhancement of ECG signal by using digital FIR Filter", *International Journal of Science and Research,* 2013.

[8] M. Tantawi, K. Revett, A. Salem, and F. Tolba, "Fiducial feature reduction analysis for electrocardiogram (ECG) based biometric recognition", *Journal of Intelligent Information Systems*, *40*(1), pp. 17-39, 2013.

[9] A. O'Sullivan, J. Sirevaag, and W. Rohrbaugh, "Cardiovascular biometrics: combining mechanical and electrical signals", IEEE Transactions on Information Forensics and Security, vol. 10(1), pp. 16-27, 2014.

[10] S. Solomon, *Essential echocardiography* , Totowa, NJ: Humana Press, pp. 98-106, 2007.

[11] K. Pichamuthu, Tutorial 5 (2009) - Assessment of LV systolic function, Retrieved May 21, 2015, from http://www.criticalecho.com/content/tutorial-5-assessment-lv-systolic-function.

[12] EKG vs. Echo - Heart health can depend on both. (n.d.), Retrieved May 23, 2015, from http://wuphysicians.wustl.edu/page.aspx?pageID=1301.

[13] Moody GB and Mark RB, The impact of the MIT-BIH Arrhythmia Database, IEEE Eng in Med and Biol 20(3): 45-50 (PMID: 11446209), 2011.

SESSION

BIOMEDICAL ENGINEERING AND IMAGING SCIENCE

Chair(s)

TBA

Spatial Fuzzy C-Means Algorithm for Bias Correction and Segmentation of Brain MRI Data

Wedad S. Salem
Dept. of Computers and Systems
Electronics Research Institute,
Giza, Egypt
wedad@eri.sci.eg

Hesham F. Ali
Dept. of Computers and Systems
Electronics Research Institute,
Giza, Egypt
hesham@eri.sci.eg

Ahmed F. Seddik
Dept. of Biomedical Engineering
Faculty of Engineering, Helwan
University, Cairo, Egypt
ahmed_sadik@h-eng.helwan.edu.eg

***Abstract*—Accurate brain Magnetic Resonance Imaging (MRI) segmentation is a challenging task due to the complex anatomical structure of brain tissues in addition to the existence of intensity non-uniformity, partial volume effects, and noise. Segmentation methods based on fuzzy c-means approaches have been developed to overcome the uncertainty caused by these effects. In this study, a novel spatial modified bias correction FCM algorithm is applied to brain MRI for the purpose of segmentation where neighborhood effect is taken into consideration. The key contribution of this model is the use of the spatial information term to handle the potential sources of artifacts in the MRI data efficiently. Experiments performed on both simulated and real brain MRI datasets have shown that the proposed algorithm, called SBCFCM, has satisfactory outputs when compared with several state of the art algorithms.**

***Index Terms*—Magnetic resonance imaging (MRI), Medical image processing, FCM, Image segmentation, Bias field, Spatial information.**

I. Introduction

Image segmentation is necessary for performing quantitative and qualitative analysis and is defined as the simplify or changing of the representation of an image into something that is more feasible and easier to analyze [1]. Brain MRI segmentation is an important processing step in many medical and clinical applications where decision-making is critical. It plays critical and important role in the study of various abnormalities disease structurally, such as multiple sclerosis, epilepsy, Parkinson's disease (PD), and Alzheimer's disease (AD) [1-4]. Segmentation of the brain structure from magnetic resonance imaging (MRI) has received paramount importance as MRI distinguishes itself from other modalities. Not all the techniques are suitable for medical image analysis because of complexity and inaccuracy. Brain MRI is a collection of images that contain large volumes of information, and, therefore, manual brain MRI segmentation is a time-consuming task [5, 6]. Based on this imaging technique, segmentation of three major cerebral tissues (namely GM, WM and CSF) will facilitate computer-aided diagnosis and patient follow-up.

When dealing with MRI brain images, there are potential sources of artifacts affecting the image during the imaging process. The main artifacts in MRI are noise, partial volume effect (PVE) and intensity non-uniformity (INU). The main sources of noise are categorized as biological, and scanner noises introduced in [7, 8]. PVE is recognized as a mixture of intensities due to the presence of more than one tissue type in the same voxel. Increasing the image resolution results in lower PVE, but it may lead to a higher level of system noise and a reduced signal-to-noise ratio [9]. INU, also known as bias field or spatial intensity inhomogeneity, is a low frequency smoothed artifact induced by the radio-frequency coil in magnetic resonance imaging (MRI) during the scanning process [10-12]. INU causes the intensities of the same tissue vary with voxel locations and can cause segmentation inaccuracies. Therefore, intensity inhomogeneities correction and segmentation can be viewed as an intertwined procedure to enhance the performance of MRI segmentation [13]. Segmentation based methods are the most popular types of methods for bias field correction [14].

Many researchers have introduced methods to overcome the challenges of brain MRI segmentation. Such methods are mainly classified into three categories including region-based methods, boundary-based methods and pixel classification-based methods [2, 3]. The region-based methods use the homogeneity feature representing one of the corresponding brain tissues. The main sub-categories of this method are thresholding, region growing, and region splitting & merging [15, 16]. Boundary-based methods where the gradient features close to an object boundary are used as a measure of discontinuity to guide segmentation decisions. The approach is to planning region boundaries by using closed curves or surfaces that deform under the influence of internal and external forces. Active Contours (Snakes) and Level Set are examples of methods in this category [17-21].

The pixel classification-based methods are pattern recognition techniques that attempt to partition a feature space obtained from the MRI image using data with known labels (WM, GM, CSF and air for brain MRI). Also, it can be divided into two groups: parametric and non- parametric algorithms [9]. In the parametric methods, MRI data follows a Gaussian distribution, and the bias field is constructed as various smooth functions representing its smooth spatial effect [20]. In this case, the statistical model parameters are usually estimated by a Maximum Likelihood (ML) or Maximum A Posteriori (MAP)

approach [22, 23]. The Expectation-Maximization (EM) algorithm is used for the optimization process [24].

The unsupervised non-parametric algorithm has been recently proposed for adult brain MRI segmentation and does not require any prior knowledge on the intensity probability distribution. The bias field is usually integrated into energy functional, and ML or MAP can also be used for this method.

Many researchers have proposed bias field correction methods that are combined with tissue classification methods typically within the domain of brain MRI analysis. Among them, methods based on the expectation-maximization (EM) algorithm [25-28] and Fuzzy C-mean (FCM) clustering [9, 10, 29-39] are the most popular ones.

Finite mixture and more frequently finite Gaussian mixture models (GMM) are used and modified to incorporate intensity inhomogeneity [26]. Displaros et al. [25] proposed a novel spatially constrained generative model and an EM algorithm for Markov-based image segmentation (SCGM-EM). To overcome the shortcoming of the spatially variant finite mixture model, Nikou et al. [28] proposed a class-adaptive spatially variant mixture model (CA-SVFMM). However, the EM algorithm is highly computationally intensive, especially for large problems, in addition, the EM algorithm requires a good initial guess for the bias field and the classification estimate.

The brain MRI data can be segmented by using different fuzzy clustering algorithms, such as the FCM approaches, where the objective function is modified to adapt to intensity inhomogeneity. The principle of these clustering techniques is to estimate three clusters being considered (GM, WM, and CSF) by iteratively computing a mean intensity for each class. So this is consistent with the partial volume effect observed in MRI images and thus eliminates the explicit modeling of mixed classes. Ahmed et al. [10] proposed adaptive FCM algorithm incorporate a spatial penalty term into the objective function to estimate the bias field by modifying the objective function of FCM and developed the BCFCM algorithm. To continue to improve the robustness to noise and reduce the computational complexity, (Liew and Yan. [36], Chuang, K.-S.[29]) developed a spatially constrained algorithms, which could overcome the disadvantages of the conventional FCM algorithm. Siyal et al. [39], present a modified FCM algorithm for bias estimation and segmentation of MRI. By adapt the objective function of the standard FCM that deal with the intensity inhomogeneities and Gaussian noise effectively.

A new algorithm called fuzzy local information c-means (FLICM) [34] was proposed by Krinidis and Chatzis, which could overcome the disadvantages of conventional FCM algorithm. The major characteristic of this algorithm is the use of a fuzzy local (both spatial and intensity level) similarity measure aiming to guarantee noise insensitiveness. Zexuan Ji et al. [33], incorporated the global information into the CLIC model to enhance its robustness to the involved control parameters. In [31] A robust spatially constrained fuzzy c-means (RSCFCM)algorithm was proposed where, the spatial factor is constructed depending on the posterior probabilities and prior probabilities.

In this paper, a novel combination of the modified FCM based method and the spatial information was developed to reduce the noise impact, obtain a smooth and slowly varying bias field, and produce satisfying segmentation results. The results obtained are compared to some other methods on both simulated and real brain MRI images.

The review is organized as: In Section II, Related work is presented. The proposed model is described in Section III. In Section IV, Experimental Results are presented. Conclusions are given in Section V.

II. Related Work

A. Fuzzy C-Means

The Fuzzy C-Means (FCM) algorithm was first proposed by Dunn [40] and later was extended by Bezdek [41]. FCM allows objects to belong to more than one cluster with the associated probability for each class [9]. Let X=(x1, x2...xN) denotes an observed image with N pixels to be partitioned into c clusters, where xi represents the gray value of the ith pixel. The algorithm is an iterative optimization that minimizes the objective function defined as follows:

$$J_{FCM} = \sum_{k=1}^{N}\sum_{i=1}^{c}(u_{ik})^m \, d^2(x_k, v_i) \quad (1)$$

where c is the number of clusters with $2 \le c < N$, u_{ik} represents the membership of pixel x_k in the i^{th} cluster, m is a weighting exponent controls the index of fuzziness, v_i is the prototype of the center of cluster i, $d^2(x_k, v_i)$ is a distance measure between object x_k and cluster center v_i. $d^2(x_k, v_i) = \|x_k - v_i\|^2$, where $\|.\|$ is a norm metric.

By minimizing (1) using the first derivatives with respect to u_{ik} and v_i then setting them to zero, membership functions and cluster centers are updated by the following:

$$u_{ik} = \frac{1}{\sum_{j=1}^{c}\left(\frac{d(x_k, v_i)}{d(x_k, v_j)}\right)^{\frac{2}{(m-1)}}} \quad (2)$$

$$v_i = \frac{\sum_{k=1}^{N}(u_{ik})^m \; xk}{\sum_{k=1}^{N}(u_{ik})^m} \quad (3)$$

B. Bias Field Formulation

The bias field in an observed MRI image can be modeled as a multiplicative component of an observed image [10, 42], shown as follows:

$$Y_k = B_k X_k + n \quad (4)$$

where Y_k is the observed image at voxel k, X_k is the true image to be restored , B_k is an unknown gain field, and n is the additive zero-mean Gaussian noise. Modelled (4) as an additive component by applying a logarithmic transformation [43] we obtain a more meaningful equation as shown below:

$$y_k = x_k + b_k \quad (5)$$

Where x_k and y_k are the true and observed log transformed intensities at the kth voxel, respectively, and b_k is the bias field at the kth voxel.

C. Spatial Fuzzy C-Means

In [29], Chuang et al. proposed spatial FCM algorithm in which spatial information can be incorporated into fuzzy membership functions directly using a spatial function be defined as

$$h_{ik} = \sum_{l \in NB(x_k)} u_{il} \quad (6)$$

Where $NB(x_k)$ denotes a local window centered on the image pixel x_k, the spatial function is incorporated into membership function as follows:

$$\tilde{u}_{ik} = \frac{u_{ik}^p \, h_{ik}^q}{\sum_{l=1}^c u_{lk}^p \, h_{lk}^q} \quad (7)$$

where p and q are two parameters to control the relative importance of membership and spatial functions respectively.

D. Bias Corrected Fuzzy C-Means

In [10], Ahmed et al. introduced a modified fuzzy c-means algorithm (BCFCM) for bias field segmentation of MRI image in the presence of intensity inhomogeneity. The modified objective function is expressed as

$$J_m = \sum_{k=1}^{N} \sum_{i=1}^{c} {u_{ik}}^m \, d^2(x_k, v_i) + \frac{\alpha}{N_R} \sum_{k=1}^{N} \sum_{i=1}^{c} {u_{ik}}^m \sum_{x_r \in N_k} d^2(x_r, v_i) \quad (8)$$

Where N_k represents a set of neighbors that exist in a window around x_k and N_R is the cardinality of N_k . The parameter α controls the penalty effect of the neighbors term. The second term acts as a regularizer and biases the solution toward piecewise-homogeneous labeling.

III. Proposed Model

In the following, we will introduce some modifications to the parameter of Ahmed et al. algorithm then uses the spatial function (6) for the modified membership function of bias corrected fuzzy C-Means (BCFCM).

Substituting (5) into (8), we have

$$J_m = \sum_{k=1}^{N} \sum_{i=1}^{c} {u_{ik}}^m \, d^2(y_k - b_k, v_i) + \beta \sum_{k=1}^{N} \sum_{i=1}^{c} {u_{ik}}^m \sum_{x_r \in N_k} d^2(y_r - b_r, v_i) \quad (9)$$

Where β is a control parameter, $0 < \beta < 1$ and $\sum_{i=1}^c u_{ik} = 1 \ \forall k$. So, by using Lagrange multiplier in (9) the optimization problem is estimated

$$F = \sum_{k=1}^{N} \sum_{i=1}^{c} u_{ik}^m \, d^2(y_k - b_k, v_i) + \beta \sum_{k=1}^{N} \sum_{i=1}^{c} u_{ik}^m \sum_{x_r \in N_k} d^2(y_r - b_r, v_i) + \lambda\left(1 - \sum_{i=1}^{c} u_{ik}\right) \quad (10)$$

By taking the first derivative of F with respect to u_{ik} , v_i and b_k then setting them to zero results, the membership function estimator u^*_{ik} , cluster prototype $v_i{}^*$, and bias field estimator $b_k{}^*$ are given as follows

$$u^*_{ik} = \frac{1}{\sum_{j=1}^c \left(\frac{(D_{ik} + \beta\gamma_i)}{(D_{jk} + \beta\gamma_j)} \right)^{\frac{1}{(m-1)}}} \quad (11)$$

$$v_i{}^* = \frac{\sum_{k=1}^N {u_{ik}}^m . S_k}{(1+\alpha) \sum_{k=1}^N {u_{ik}}^m} \quad (12)$$

Where, $D_{ik} = d^2(y_k - b_k, v_i)$, $\gamma_i = \sum_{x_r \in N_k} d^2(y_r - b_r, v_i)$,and $S_k = (y_k - b_k) + \beta(y_r - b_r)$

$$b_k{}^* = y_k - \frac{\sum_{i=1}^c {u_{ik}}^m . v_i}{\sum_{i=1}^c {u_{ik}}^m} \quad (13)$$

By using the spatial function $h_{ik} = \sum_{l \in NB(x_k)} u_{il}$ for membership function estimator u^*_{ik} and substituting into (11), the update membership function is given as follows

$$\widetilde{u^*_{ik}} = \frac{u^{*p}_{ik} \, h^q_{ik}}{\sum_{l=1}^c u^{*p}_{lk} \, h^q_{lk}} \quad (14)$$

Solving for u^*_{ik} , we have the updated membership function as follows

$$\widetilde{u^*_{ik}} = \frac{h_{ik}^{q}.\left(\frac{1}{(D_{ik}+\beta\gamma_i)}\right)^{\frac{p}{(m-1)}}}{\sum_{l=1}^{c} h_{lk}^{q}.\left(\frac{1}{(D_{lk}+\beta\gamma_l)}\right)^{\frac{p}{(m-1)}}} \quad (15)$$

Especially, when p=1, q=0, and $\beta = \frac{\alpha}{N_R}$,the $\widetilde{u^*_{ik}}$ is BCFCM membership function proposed by Ahmed [10].

The proposed SBCFCM algorithm for estimating the bias field and segmenting the MRI images into different clusters can be summarized as follow:

step1: Select parameters p,q, β and ε(termination criterion).

step2: Set the number of cluster c, initialize class prototypes $\{v_i\}_{i=1}^{c}$ by choosing centroid vector of standard FCM, set $\{b_k\}_{k=1}^{N}$ equal to very small values.

step3: Compute the partition matrix using (11).

step4: Update the prototypes of clusters using (12).

step5: The bias term is obtained using (13).

step6: Repeat steps 3-5 till termination satisfies$\|V_{new} - V_{old}\| < \varepsilon$.

step7: Compute the spatial modify partition matrix using (15).

IV. Experiment and Results

In this section, the proposed method has been applied to two publicly available databases, simulated and real MRI data. BrainWeb dataset, containing simulated MR images provided from the Brain web (http://www.bic.mni.mcgill.ca/brainweb). The IBSR dataset (http://www.cma.mgh.harvard.edu/ibsr) containing real brain MR image data and segmentation results contributed and utilized by the trained experts.

A. Evaluation Quantitative Comparison

For comparison purpose, all segmentation results are quantitatively evaluated by using a set of standard measures for the evaluation of brain MRI segmentation algorithms. Some of these indices are presented in [44] like Jaccard similarity index, Dice coefficient, Accuracy coefficient [45].

$$Dice = \frac{2\,|Igt \cap Iseg|}{|Igt| + |Iseg|} = \frac{2 \times Tp}{(2.\times Tp) + Fp + Fn} \quad (16)$$

$$\text{Jaccard} = \frac{|Igt \cap Iseg|}{|Igt \cup Iseg|} = \frac{Tp}{Tp + Fp + Fn} \quad (17)$$

$$\text{Accuracy} = \frac{Tp + Tn}{Tp + Tn + Fp + Fn} \quad (18)$$

Where Igt and Iseg are the ground truth, and the result segmented pixels 'set respectively. |Igt| is the number of Igt pixels. In the Eq.(16)-(18) TP, TN, FP, and FN are True Positive, True Negative, False Positive and False Negative respectively [24, 30]. A higher value of the criteria indicates more accurate segmentation [35].

B. Segmentation of simulated brain MRI

T1-weighted brain MR images with 1 mm cubic voxels, volume size of 217×181 × 181 are employed to investigate the

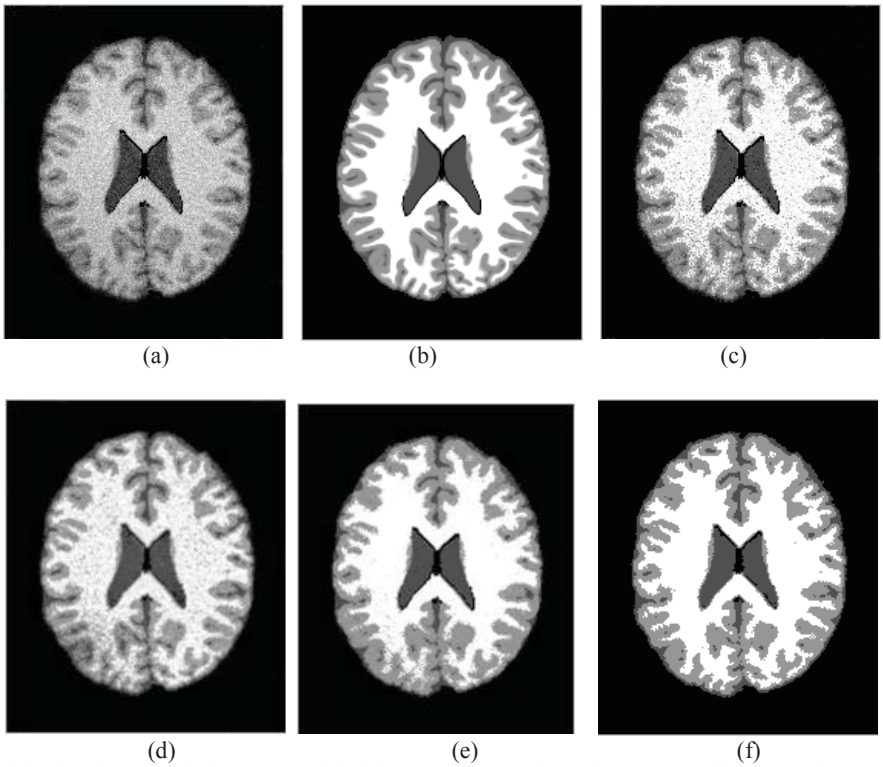

(a) (b) (c)

(d) (e) (f)

Fig.1. segmentation of simulated MRI brain image: (a) original image with 9% noise and 40% INU (slice = 96); (b) ground truth; (c) FCM; (d) BCFCM; (e) SCFCM and (f) SBCFCM segmentation results.

proposed method. These images are obtained from the BrainWeb Simulated Brain Database at the McConnell Brain Imaging Centre of the Montreal Neurological Institute (MNI), McGill University. In this section, the proposed algorithm would be compared with fuzzy methods of FCM, BCFCM [10] and SCFCM [29]. In the FCM algorithm, the intensity of pixels is used as a feature and the Norm index FCM objective function is selected two. In BCFCM, all parameters are selected as reported in [10]. The parameters of SCFCM are set as follows: the spatial information parameters are p=1& q=1, a window size of the neighborhood is 5, and the weighting exponent is 2 [29]. In our model, we set the SBCFCM parameter as: p=1,q=2, β=0.18, ε=0.0001 and 5x5 window.

Fig.1a shows a slice of the simulated 3D volume of MRI (slice = 96) with 9% noise and 40% INU. The ground truth of this image is presented in Fig.1b. Segmentation results of FCM, BCFCM and SCFCM are shown at Fig.1c-e, respectively. The result of the proposed method SBCFCM is shown in Fig.1f.

According to Fig.1, the visual evaluation of the images shows that the standard FCM technique is not adapted to intensity inhomogeneity as well as the effect of noise causes the misclassification of GM and WM at numerous places. Also, BCFCM algorithm is severely influenced by the artifact. On the other hand, by comparison of the results shown in Fig.1e and Fig.1f. It can be verified that the segmentation results by SCFCM can be robust to the noise and obtain better results than FCM and BCFCM, but some wrong results by overmuch the GM diameter than ground truth. However, the proposed method can reduce the effects of the image noise and INU.

The quantitative evaluation Dice's similarity, Accuracy indices and Jaccard similarity of Fig.1 are listed in Tables 1.

According to Table 1 and Fig.1, the proposed method leads to a satisfactory performance among the mentioned strategies. Note that to evaluate the effectiveness of segmentation method in each tissue, the main quantitative criteria should be considered along with the associated image.

Slice130 with 7% noise and 20% INU is selected for evaluation purpose. The results of segmentation using FCM, BCFCM, SCFCM and the proposed algorithm are presented in Fig.2. Fig.2 (g-l) shows the enlarged partial views of the marked rectangles regions in Fig.2 (a-f). By comparing these different methods, we find that the proposed algorithm can produce better structures and more accurate segmentation results, especially in the area with abundant image details. Mean Dice, Accuracy and Jaccard similarity index of simulated

TABLE I.

COMPARISON OF THE EVALUATION CRITERIA DICE, ACCURACY (ACC.) & JACCARD (JS) FOR DIFFERENT METHODS IN FIG.1

	Dice			Acc.			JS		
	WM	GM	CSF	WM	GM	CSF	WM	GM	CSF
FCM	0.8920	0.8044	0.8122	0.9044	0.8658	0.9455	0.8051	0.6728	0.6837
BCFCM	0.9137	0.8151	0.8121	0.9235	0.8795	0.9446	0.8410	0.6879	0.6836
SCFCM	0.9250	0.8651	0.8555	0.9316	0.9054	0.9598	0.8605	0.7622	0.7475
SBCFCM	0.9561	0.9065	0.8704	0.9590	0.9364	0.9630	0.9159	0.8291	0.7706

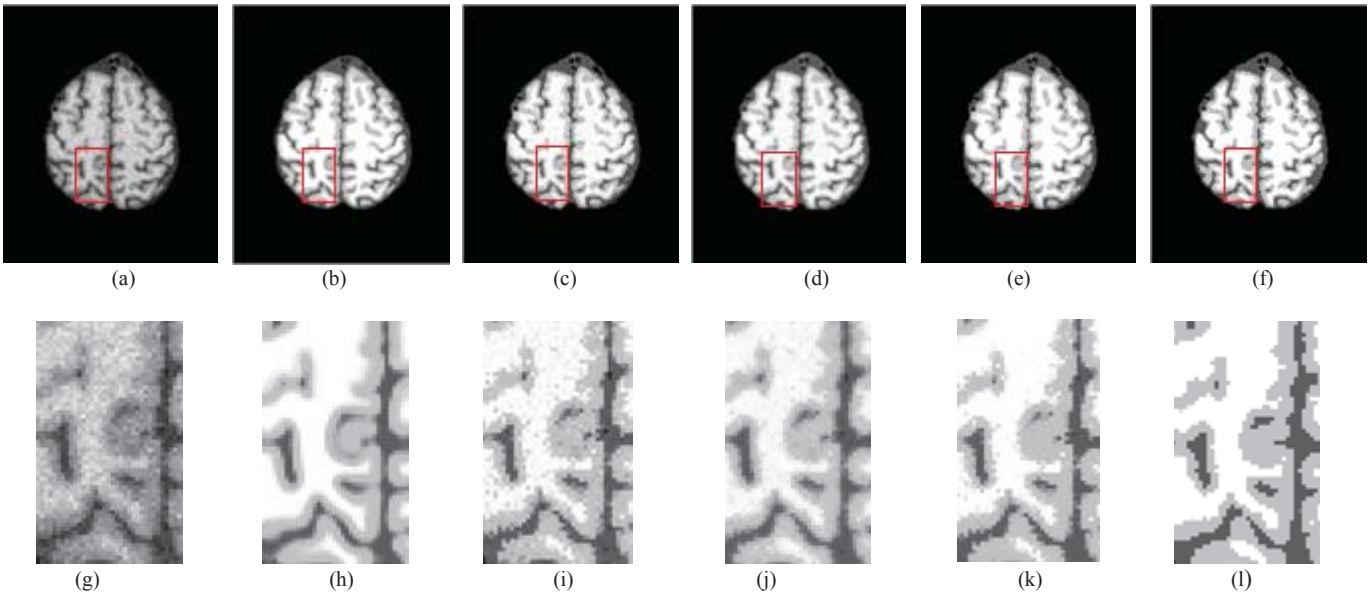

(a) (b) (c) (d) (e) (f)

(g) (h) (i) (j) (k) (l)

Fig.2. Comparison of the segmentation results on a simulated MRI brain image with 7% and 20% INU (slice = 130): (a) original image; (b) Ground truth; (c) FCM; (d) BCFCM; (e) LNLFCM and (f) proposed algorithm results; (g-l) zoom in segmentation regions of (a-f) .

TABLE II

MEAN DICE, ACCURACY AND JACCARD INDICES FOR DIFFERENT METHODS SHOWN IN FIG.2 WITH 7% NOISE AND (20% & 40% INU) RESPECTIVELY.

	Dice		Acc.		JS	
	20% INU	40% INU	20% INU	40% INU	20% INU	40% INU
FCM	0.8787	0.8699	0.9246	0.9109	0.7842	0.7746
BCFCM	0.8997	0.8986	0.9387	0.9384	0.8185	0.8171
SCFCM	0.8969	0.8814	0.9385	0.9265	0.8138	0.7918
SBCFCM	0.9101	0.9091	0.9448	0.9425	0.8358	0.8323

T1 image with 7% noise, 20% and 40% INU (slice 130) are reported in Table 2.

As shown in table 2, by comparing the quantitative analysis of the segmented results on MRI image with the same noise and different intensity inhomogeneity. The change rate of the evaluation criteria is more in the case of FCM and SCFCM than in the case of BCFCM and Proposed algorithm. The reason of that is the first case does not take into consideration the bias field. Finally, according to Fig.2 f, l and Table 2, the proposed algorithm shows the acceptable results on the critical slices in the human brain MRI.

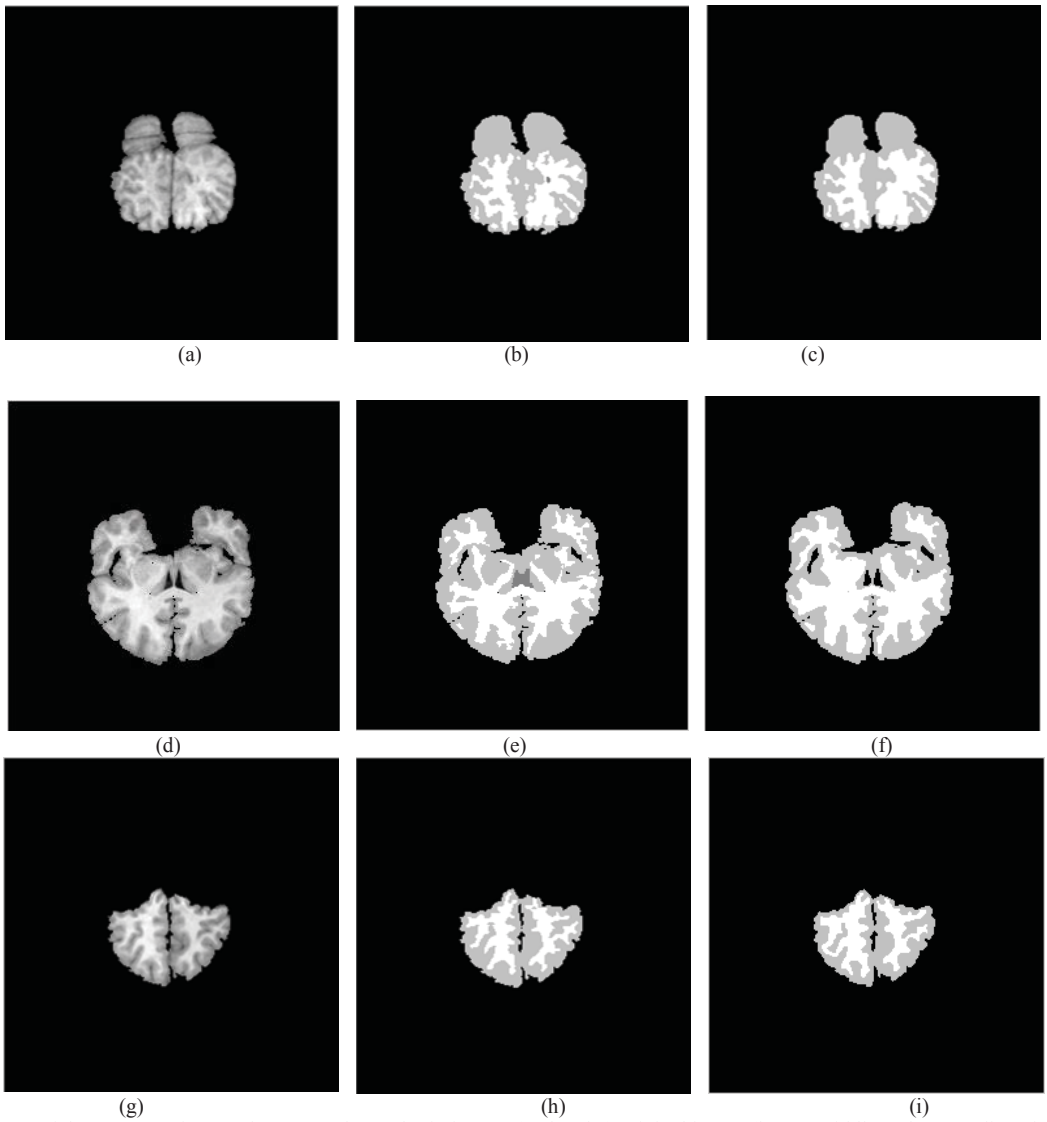

Fig.3. Comparison of the segmentation results on a real MRI brain image: (a, d and g) original image (lower, middle and upper slices from IBSR 13_3, respectively); (b, e and h) manual segmented by expert; (c, f and i) Proposed algorithm results.

C. Segmentation of real brain MRI

The 20 normal real MR brain data sets and their manual segmentation results were provided by the Center for Morphometric Analysis at Massachusetts Hospital and are available at http://www.cma.mgh.harvard.edu/ibsr is one the relevant dataset of IBSR. The MR images with the following parameter :slice thickness 3.1 mm, 8-bit scaled 3D MRI data files, matrix= 256 ×256. For visual evaluation, three lower, middle and upper slices are selected from one file of the dataset (IBSR 13_3), and our algorithm was applied to them. Fig. 3a, d, and g are three originally selected slices. The manual segmented results are shown in Fig.3b, e and h respectively . The corresponding segmentation results achieved by our algorithm are shown in Fig. 3c, f and, i respectively.

Table 3 gives the Jaccard similarity of the Adaptive MAP, FCM, Tree Structure K-Means (TSKM) and Maximum Likelihood (ML) which are provided by the IBSR. Also, CSWTSOM [46] and the results of the proposed method. From Table 3 it can be observed that our method has significantly better performance than those with no INU correction methods.

For more analysis, SBCFCM is applied on all slices of IBSR 13_3 and the Dice coefficients of WM and GM are shown in Fig. 4. The average percent of Dice similarities of WM and GM achieved by SBCFCM in this volume are 85.8% and 89%.

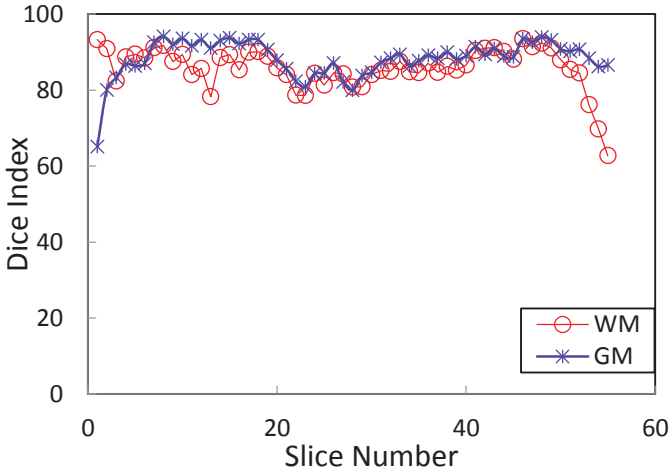

Fig. 4. Dice Similarity coefficients (%) of all slice of IBSR13_3

TABLE III

MEAN JACCARD SIMILARITY FOR DIFFERENT METHODS ON IBSR DATASET.

	AMAP		FCM		ML		TSKM		CSWTSOM		Our method	
	GM	WM	GM	WM	GM	WM	GM	WM	GM	WM	GM	WM
Image 2-4	0.36	0.28	0.31	0.29	0.31	0.29	0.31	0.29	0.45	0.30	0.69	0.51
Image 5-8	0.27	0.13	0.20	0.08	0.20	0.08	0.18	0.07	0.69	0.56	0.75	0.62
Image 7-8	0.62	0.64	0.53	0.65	0.53	0.65	0.52	0.66	0.54	0.35	0.74	0.66
Image 11-3	0.66	0.71	0.58	0.72	0.58	0.72	0.59	0.72	0.70	0.63	0.78	0.69
Image 13-3	0.65	0.68	0.52	0.71	0.52	0.71	0.53	0.72	0.71	0.60	0.83	0.79
Image 16-3	0.58	0.57	0.46	0.55	0.46	0.55	0.48	0.56	0.69	0.55	0.52	0.39
Image 100-23	0.66	0.66	0.55	0.67	0.55	0.67	0.55	0.67	0.72	0.59	0.53	0.47
Image 111-2	0.57	0.65	0.48	0.64	0.48	0.64	0.50	0.65	0.68	0.65	0.74	0.65
Image 191-3	0.66	0.69	0.57	0.72	0.57	0.72	0.57	0.72	0.66	0.60	0.70	0.66
Image 205-3	0.67	0.70	0.59	0.71	0.59	0.71	0.58	0.71	0.71	0.63	0.71	0.72
Average	**0.57**	**0.571**	**0.48**	**0.57**	**0.48**	**0.57**	**0.48**	**0.58**	**0.65**	**0.55**	**0.70**	**0.62**

V. Conclusion and Future Work

In this paper, we have integrated a novel spatial modified bias correction FCM algorithm by incorporating the spatial information into the modified membership function to compensate for noise and intensity inhomogeneity that are observed in MRI data. The neighboring pixels have similar feature values, and the probability that they belong to the same cluster is great. Thus, the spatial relationship effect reduces the number of misclassification of tissues classes for noisy images.

The proposed algorithm, called SBCFCM, was tested on two publicly available simulated and real datasets. First experiments performed on several noisy (up to 9% noise) and bias (up to 40% INU) Brainweb MR Images, highlight the usefulness of this spatial consideration. The proposed algorithm can reduce the impact of image noise and INU.

We compared our results with traditional FCM , Ahmed's modified BCFCM [10] and SCFCM[29]. Our results demonstrated that SBCFCM outperformed these methods in many aspects, especially when comparing the quantitative analysis for an image with the same noise and different intensity inhomogeneity. The change rate was more in case of FCM and SCFCM than in the case of BCFCM and Proposed algorithm. The reason of that first case does not take in consideration the bias field.

An additional experiment carried out on the real brain IBSR database. It has shown that this new SBCFCM algorithm reliably extracts brain tissue maps with better performance comparable to state of the art methods (AMAP, FCM, TSKM, ML, and CSWTSOM).

REFERENCES

[1] W. S. Salem, A. F. Seddik, and H. F. Ali, "A Review on Brain MRI Image Segmentation." International Conference on New Paradigms In Electronics &Information Technology PEIT'013,pp.35, 2013.

[2] M. M. Ahmed and D. B. Mohamad, "Segmentation of Brain Magnetic Resonance Images (MRIs): A Review," Int. J. Advance. Soft Comput. Appl, vol. 3, 2011.

[3] M. A. Balafar, A. R. Ramli, M. I. Saripan, and S. Mashohor, "Review of brain MRI image segmentation methods," Artificial Intelligence Review, vol. 33, pp. 261-274, 2010.

[4] R. Agrawal and M. Sharma, "Review of Segmentation Methods for Brain Tissue with Magnetic Resonance Images," International Journal of Computer Network and Information Security (IJCNIS), vol. 6, p. 55, 2014.

[5] T. Logeswari and M. Karnan, "An improved implementation of brain tumor detection using segmentation based on hierarchical self organizing map," International Journal of Computer Theory and Engineering, vol. 2, pp. 1793-8201, 2010.

[6] A. Farag and M. Fakhreldin, "Heart Localization from Magnetic Resonance Images Sequence," Journal of Computer Science, vol. 8, 2012.

[7] S. Prima, N. Ayache, T. Barrick, and N. Roberts, "Maximum likelihood estimation of the bias field in MR brain images: Investigating different modelings of the imaging process," in Medical Image Computing and Computer-Assisted Intervention–MICCAI 2001, 2001, pp. 811-819.

[8] M. Styner, C. Brechbuhler, G. Szckely, and G. Gerig, "Parametric estimate of intensity inhomogeneities applied to MRI," Medical Imaging, IEEE Transactions on, vol. 19, pp. 153-165, 2000.

[9] B. Caldairou, N. Passat, P. A. Habas, C. Studholme, and F. Rousseau, "A non-local fuzzy segmentation method: application to brain MRI," Pattern Recognition, vol. 44, pp. 1916-1927, 2011.

[10] M. N. Ahmed, S. M. Yamany, N. Mohamed, A. A. Farag, and T. Moriarty, "A modified fuzzy c-means algorithm for bias field estimation and segmentation of MRI data," Medical Imaging, IEEE Transactions on, vol. 21, pp. 193-199, 2002.

[11] A. Simmons, P. S. Tofts, G. J. Barker, and S. R. Arridge, "Sources of intensity nonuniformity in spin echo images at 1.5 T," Magnetic Resonance in Medicine, vol. 32, pp. 121-128, 1994.

[12] J. G. Sled, A. P. Zijdenbos, and A. C. Evans, "A nonparametric method for automatic correction of intensity nonuniformity in MRI data," Medical Imaging, IEEE Transactions on, vol. 17, pp. 87-97, 1998.

[13] C. T. Larsen, J. E. Iglesias, and K. Van Leemput, "N3 Bias Field Correction Explained as a Bayesian Modeling Method," in Bayesian and grAphical Models for Biomedical Imaging, ed: Springer, 2014, pp. 1-12.

[14] U. Vovk, F. Pernus, and B. Likar, "A review of methods for correction of intensity inhomogeneity in MRI," Medical Imaging, IEEE Transactions on, vol. 26, pp. 405-421, 2007.

[15] M. Cabezas, A. Oliver, E. Roura, J. Freixenet, J. C. Vilanova, L. Ramió-Torrentà, et al., "Automatic multiple sclerosis lesion detection in brain MRI by FLAIR thresholding," Computer methods and programs in biomedicine, vol. 115, pp. 147-161, 2014.

[16] Q. Ge, L. Xiao, J. Zhang, and Z. H. Wei, "An improved region-based model with local statistical features for image segmentation," Pattern Recognition, vol. 45, pp. 1578-1590, 2012.

[17] F. Lecellier, S. Jehan-Besson, and J. Fadili, "Statistical region-based active contours for segmentation: an overview," IRBM, vol. 35, pp. 3-10, 2014.

[18] H. Min, W. Jia, X.-F. Wang, Y. Zhao, R.-X. Hu, Y.-T. Luo, et al., "An Intensity-Texture model based level set method for image segmentation," Pattern Recognition, vol. 48, pp. 1543-1558, 2015.

[19] J. C. Moreno, V. S. Prasath, H. Proenca, and K. Palaniappan, "Brain MRI segmentation with fast and globally convex multiphase active contours," arXiv preprint arXiv:1308.6056, 2013.

[20] Q. Zheng, E. Dong, Z. Cao, W. Sun, and Z. Li, "Active contour model driven by linear speed function for local segmentation with robust initialization and applications in MR brain images," Signal Processing, vol. 97, pp. 117-133, 2014.

[21] F. Alhadi, W. Fakhr, and A. F. Seddik, "Hidden Markov Models for Face Recognition," in Computational Intelligence, 2005, pp. 409-413.

[22] K. Van Leemput, F. Maes, D. Vandermeulen, and P. Suetens, "Automated model-based bias field correction of MR images of the brain," Medical Imaging, IEEE Transactions on, vol. 18, pp. 885-896, 1999.

[23] J. D. Gispert, S. Reig, J. Pascau, J. J. Vaquero, P. García- Barreno, and M. Desco, "Method for bias field correction of brain T1- weighted magnetic resonance images minimizing segmentation error," Human brain mapping, vol. 22, pp. 133-144, 2004.

[24] M. M. Hadhoud, M. I. Eladawy, A. Farag, F. M. Montevecchi, and U. Morbiducci, "Left ventricle segmentation in cardiac MRI images," American Journal of Biomedical Engineering, vol. 2, pp. 131-135, 2012.

[25] A. Diplaros, N. Vlassis, and T. Gevers, "A spatially constrained generative model and an EM algorithm for image segmentation," Neural Networks, IEEE Transactions on, vol. 18, pp. 798-808, 2007.

[26] L. Gupta and T. Sortrakul, "A Gaussian-mixture-based image segmentation algorithm," Pattern Recognition, vol. 31, pp. 315-325, 1998.

[27] T. M. Nguyen and Q. J. Wu, "Fast and robust spatially constrained gaussian mixture model for image segmentation," Circuits and Systems for Video Technology, IEEE Transactions on, vol. 23, pp. 621-635, 2013.

[28] C. Nikou, N. P. Galatsanos, and C. Likas, "A class-adaptive spatially variant mixture model for image segmentation," Image Processing, IEEE Transactions on, vol. 16, pp. 1121-1130, 2007.

[29] K.-S. Chuang, H.-L. Tzeng, S. Chen, J. Wu, and T.-J. Chen, "Fuzzy c-means clustering with spatial information for image segmentation," computerized medical imaging and graphics, vol. 30, pp. 9-15, 2006.

[30] F. Dong and J. Peng, "Brain MR image segmentation based on local Gaussian mixture model and nonlocal spatial regularization," Journal of Visual Communication and Image Representation, vol. 25, pp. 827-839, 2014.

[31] Z. Ji, J. Liu, G. Cao, Q. Sun, and Q. Chen, "Robust spatially constrained fuzzy c-means algorithm for brain MR image segmentation," Pattern Recognition, vol. 47, pp. 2454-2466, 2014.

[32] Z. Ji, Y. Xia, Q. Sun, Q. Chen, and D. Feng, "Adaptive scale fuzzy local Gaussian mixture model for brain MR image segmentation," Neurocomputing, vol. 134, pp. 60-69, 2014.

[33] Z.-X. Ji, Q. Chen, Q.-S. Sun, D.-S. Xia, and P.-A. Heng, "MR image segmentation and bias field estimation using coherent local and global intensity clustering," in Fuzzy Systems and Knowledge Discovery (FSKD), 2010 Seventh International Conference on, 2010, pp. 578-582.

[34] S. Krinidis and V. Chatzis, "A robust fuzzy local information C-means clustering algorithm," Image Processing, IEEE Transactions on, vol. 19, pp. 1328-1337, 2010.

[35] C. Li, C. Xu, A. W. Anderson, and J. C. Gore, "MRI tissue classification and bias field estimation based on coherent local intensity clustering: A unified energy minimization framework," in Information Processing in Medical Imaging, 2009, pp. 288-299.

[36] A.-C. Liew and H. Yan, "An adaptive spatial fuzzy clustering algorithm for 3-D MR image segmentation," Medical Imaging, IEEE Transactions on, vol. 22, pp. 1063-1075, 2003.

[37] D. L. Pham and J. L. Prince, "Adaptive fuzzy segmentation of magnetic resonance images," Medical Imaging, IEEE Transactions on, vol. 18, pp. 737-752, 1999.

[38] K. Sikka, N. Sinha, P. K. Singh, and A. K. Mishra, "A fully automated algorithm under modified FCM framework for improved brain MR image segmentation," Magnetic Resonance Imaging, vol. 27, pp. 994-1004, 2009.

[39] M. Y. Siyal and L. Yu, "An intelligent modified fuzzy c-means based algorithm for bias estimation and segmentation of brain MRI," Pattern recognition letters, vol. 26, pp. 2052-2062, 2005.

[40] J. C. Dunn, "A fuzzy relative of the ISODATA process and its use in detecting compact well-separated clusters," 1973.

[41] J. C. Bezdek, "A Convergence Theorem for the Fuzzy ISODATA Clustering Algorithms," IEEE Transactions on Pattern Analysis and Machine Intelligence, vol. 2, pp. 1-8, 1980.

[42] C. Li, C. Gatenby, L. Wang, and J. C. Gore, "A robust parametric method for bias field estimation and segmentation of MR images," in Computer Vision and Pattern Recognition, 2009. CVPR 2009. IEEE Conference on, 2009, pp. 218-223.

[43] W. M. Wells III, W. E. L. Grimson, R. Kikinis, and F. A. Jolesz, "Adaptive segmentation of MRI data," Medical Imaging, IEEE Transactions on, vol. 15, pp. 429-442, 1996.

[44] X. Lladó, A. Oliver, M. Cabezas, J. Freixenet, J. C. Vilanova, A. Quiles, et al., "Segmentation of multiple sclerosis lesions in brain MRI: a review of automated approaches," Information Sciences, vol. 186, pp. 164-185, 2012.

[45] R. Cárdenes, R. de Luis-García, and M. Bach-Cuadra, "A multidimensional segmentation evaluation for medical image data," Computer methods and programs in biomedicine, vol. 96, pp. 108-124, 2009.

[46] A. Demirhan and İ. Güler, "Combining stationary wavelet transform and self-organizing maps for brain MR image segmentation," Engineering Applications of Artificial Intelligence, vol. 24, pp. 358-367, 2011.

V.I.S SYSTEM REVOLUTIONARY TECHNIC OF MEDICAL DIAGNOSIS

Dr. Boucherit Taieb,
BOUCHERIT Laboratory, Yagoubi Abdelkader Oran, Algeria.
07, road kaddour salah houari Delmonte Oran, Algeria
Sponsored by **Dr.Abdelmalek Boudiaf, Minister of Health**, Algeria

Abstract – *The ideal and the dream of any practitioner doctor is to do a medical diagnosis unerringly without hurting the patient, and in record time. This will be a breakthrough in the field of medicine. Typically the patient who suffers from a pathologie or disease presents to the doctor for treatment and be relieved of the pain that hurts him, the doctor performs a physical examination with (interrogatory, palpation, auscultation) request laboratory tests and radiological examinations (scanner, MRI) to ask for a positive diagnosis and treatment process. This entire process is necessary and indispensable to be able to get treatment, and usually the diagnosis is unclear. This process takes a lot of time, money and effort to a patient that already suffering. The* ***VIS System*** *or* ***Vitreous imaging system*** *is a discovery technique that results used to make a patient's diagnostic in record time and without going through all steps described above (publication made in WorldComp'11) practiced since several thousand patients with unparalleled success rate so far, the dream became reality*

1 Introduction

The V.I.S system or Vitreous imaging system is a technique for diagnostic and medical imaging that stems from a discovery in medical field research and imaging, it helps to be a diagnostic in record time imaging without using traditional techniques, all stages of the traditional diagnostic research is blacklisted, and we do not need in this new technique as the photo of the patient's eye, the VIS system is a technique which displays the image, or pathological organs in the vitreous humor, it gives us a self-localization of lesions per organ or images of organs in the vitreous humor. The diagnosis is made in minutes exactly, the error does not exist, and the doctor or practitioner only reads the images he sees in the vitreous humor. (Publication made in WorlComp'11) since that time the technique was perfected and more than two thousand summers have diagnostic fact, the obtained images by the V.I.S system are clearer and more detailed than images obtained by a scanner or MRI

.

2 Material & Methods

2.1 Materials

The material is very simple; it consists of a camera & computer,

2.2 Methods

- Photo of the eye.
- Front view photo of the eye
- Camera without flash
- Environment slightly enlightened without important source of light
- The "*vitreous imagery system*" makes it possible to visualize the images of the patient's organs in the vitreous humor , these images are laid out in bulk, with sometimes the repetition more than one organ same organ with different view.
- We *resize* each image of organs obtained in the humor vitreous to isolate each image.

Please use the styles contained in this document for: Title, Abstract, Keywords, Heading 1, Heading 2, Body Text, Equations, References, Figures, and Captions.
Do not add any page numbers and do not use footers and headers (it is ok to have footnotes).

2.3 Theory & explanation

All images are formed on the retina, which converted it into nerve impulse and transmits it to the brain and since each eye receives an image a little different from the observed object, the brain compares the information coming from each eye and reconstitutes the image in three dimensions.

The human eye is a window open on the outside world, it receives the images from the outside environment and transmits to the brain to be analyzed and treated according to the corresponding answers. The image is formed on the retina, which converted it into nerve impulse and transmits it to the brain and since each eye receives an image a little different from the observed object, the brain compares the information coming from each eye and reconstitutes the image in three dimensions.

2.4 Anatomical composition of the eye

The eyeball of a grow- up measures 2.5 cm this little volume regroups nervous cells, muscles and transparent surroundings.

Muscles: these are the cilliary bodies, which modify the curvature of crystalline lens during accommodation

Cornea: is a transparent membrane made up of several layers which are directly in contact with the ambient air.

Aqueous humor: is a transparent watery fluid that is permanently, filtered and renewed in order to keep the eyeball in proper and good condition.

Iris: is a diaphragm that regulates the amount of light that the enters through the pupil.

Crystalline lens: is a simple convergent lens, that is held by ligaments which are tied to muscles (ciliairy bodies) they modify in this way the curvature of the crystalline lens and make possible focusing.

Vitreous humor: is a transparent gelatinous and translucent substance whose function is to keep the retina against the inner lining of the eye it defines the form the eye and represents 90% of its volume.

Retina: is a nervous membrane forming the inner lining of the posterior wall of the eye, it is a few tens millimeters thick with a global surface of 2.5cm x 2.5cm, it consists of 130 million nerve cells (125 million retinal rods and 5 million retinal cones). It transforms light into electric signals which are conveyed to the brain.

Sclerotic: is the firm that forms the outer covering of the eyeball, its anterior covering is the cornea; the sclera is perceptible from the outside and constitutes the whites of the eyes.

This is the classical theory of today.

this theory is inadequate for it cannot explain the complexity of the eye : you notice that the major part of the eye (90%) is the vitreous humor whose only function is to maintain the shape of the eye , while the retina, a membrane of 2.5 cm² and few ten millimeters thick consists of 130 million nerve cells, each one , has a very precise function, a plant that is so complex and fitted with such technology that only 10% of its volume works, while 90% are for aesthetical reasons.

I looked into the problem and realized that the function of the vitreous humor is actually much more important than it seems.

Chemical composition of the vitreous humor: 99,6% of water, vitamin C, glucose, lactic acid, NA ,CL, hyluronic acid, complete absence of vascularization.

My research enables me to prove that the images are materialized in the vitreous humor; it is its chief function. The functions of maintenance, the nutritious function are of a minor importance.

2.5 The eye has two functions

- **An open window on the outside word**
- **An open window on the inside body**

it is a movie, camera which is recording in both way, the image is recorded and formed in "energetic image" in the vitreous humor, the retina that consists of cone cells and rod cells digitizes the image and transmits it to the brain through the optic nerve, the digitization is carried out in "energetic language"

The numeric language uses a mathematical algorithm whose basis is 0 and1.

Energetic language uses energetic algorithm whose source are colors and shapes.

Numeric image is the resultant between the observed image and the approximate image in the data bank of the computer; actually, numeric image is not a real one.

Energetic image is real, it is itself image data bank, that is to say it contains endless images, that is why the image is multidimensional and not three-dimensional wich is transmitted to the brain.

I am doing my research on this particular field and I noticed that when an organ or several ones are affected, the image of that organ appears in the vitreous humor these enlarged and processed images of organs offer anatomical, histological images with an accuracy defying any radiological, scan graphical, or microscopic equipment.

2.6 Diagram

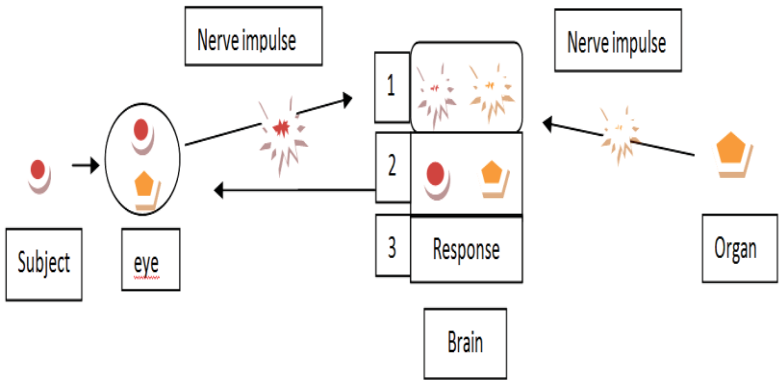

EXPLANATION OF the MECHANISM OF RECEPTION IMAGES BY the BRAIN AND INTERCONNECTION WITH the EYE

2.6 Example patient

Patient No 1

We will see together how to proceed for a diagnostic with the V.I.S system technique.

KH patient aged 40 living in Oran and New York sportives. The patient sent me two pictures by e-mail


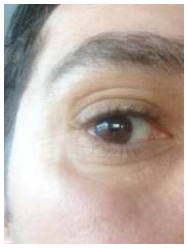

Img001 img002

We proceeds from the photos at first diagnosis by studying the Photo 001



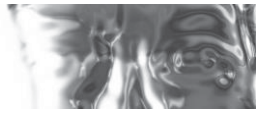

Img001 img003 img004

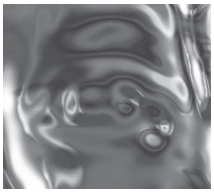
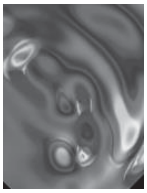


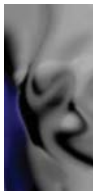

Img005 img006 img007 img008 img009

img001: Photo of face patient sent by e-mail.
img002 : Photo of eye patient
img003 : Image by V.I.S system
img004 : Enlarging of the image003 and one sees appearing images of several bodies in a disorder insulate we them each one, we have image006, image007, image008 and image009, each one of these images corresponds to a precise organ which is the heart in the image006 and 007 and that of the articulation of the knee in image009.


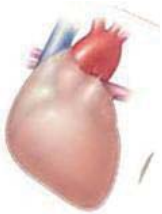
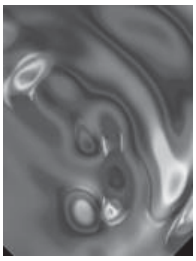
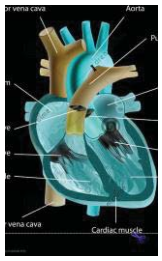

img007 comparative img006 comparative

We have an external preview of the Heart which is corresponds exactly to the heart comparative image therefore in image006 we have heart image detailled with the atrium, the ventricles which is corresponds exactly to the comparative image of the heart. Now let us pass to the other image which appeared in the eye or more precisely in the vitreous humor which is the image 008 and 009

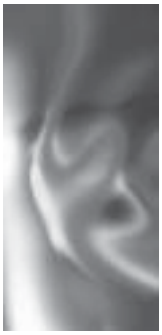

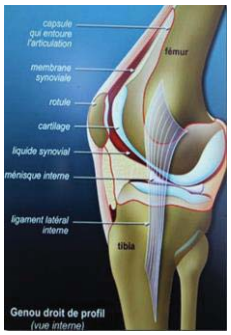

Img008 img009 comparative.

In this same image 008 et 009 we see the articulation image of the knee appears which is corresponds exactly to the comparative image of the knee with an important characteristic which is the visualization of the cross ligaments and the patellar ligament. So we can affirm the image processing of the face patient that the V.I.S System shows us two images which is the from of the heart and of the articulation of the knee, we can already pose diagnostic and say that this patient presents a cardiac pathology as well as traumatic of the articulation of the knee


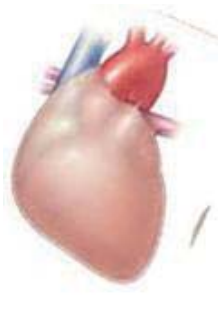
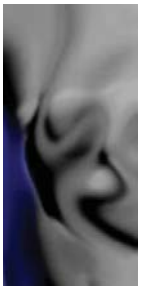


We treat now the second Photo of patient or image002

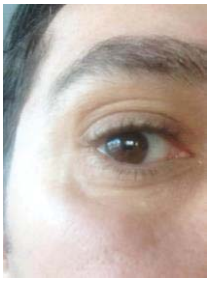
Img001

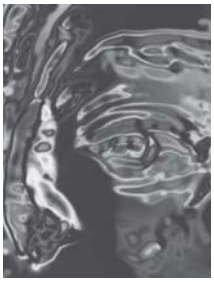
Img002

We will process the image002 by the same system V.I.S we get then the image010; by enlarging the image we see that the system brings up more images indicate.

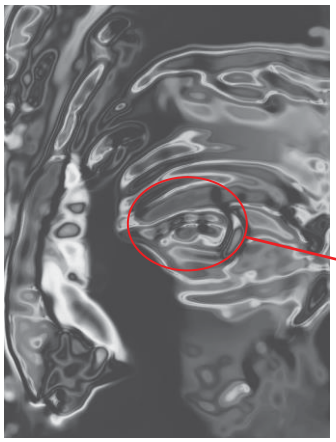
Img010

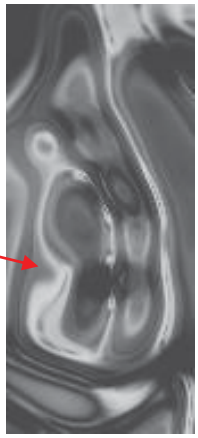
img011

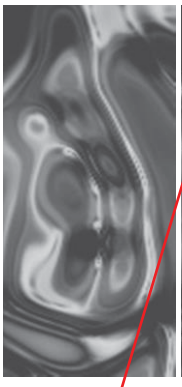
img011

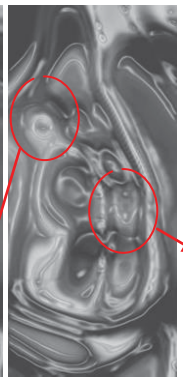
img012


img013


img014

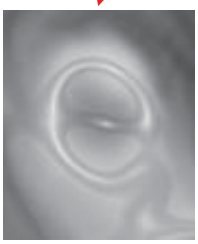
Img015

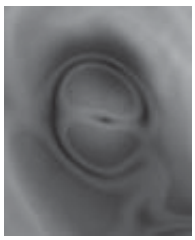
img016

The diagnosis is now more precise, we have a detailed image011 representing the heart anatomically very precisely with the appearance of the image013 and very detailed negative 014 mitral valve, as well as other image015 and its negative 016 represents the mitral valve, the accuracy of the system gives us two images of the location of the pathology that are image013 representing the mitral valve in profile and also representing the mitral valve but image015 front view. we summary we received two photos of a patient by email of New York, the treatment of these two photos by the VIS system allows us to make a positive diagnosis is that the patient suffers from two distinct pathologies, heart and specifically valvular leak the heart valve with the corresponding images of the heart as well as those of the mitral heart valve, and the other of the knee joint with a traumatic lesion of the cross and patellar ligament.

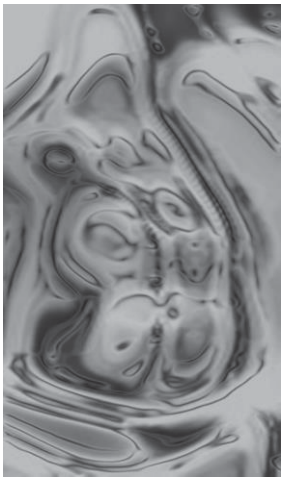
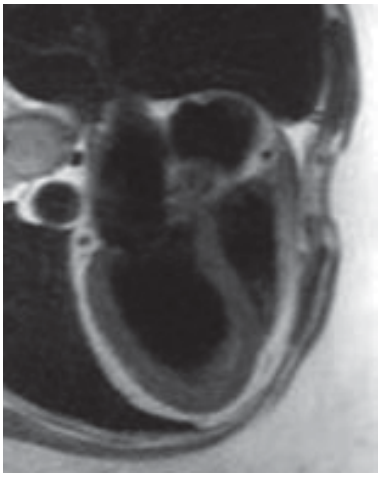

Img012 : V.I.S System Comparative: MRI Heart image

You notice the obtained image by V.I.S system contain more exactness compared with MRI comparative image, we can see clearly the mitral valve, while in MRI comparative we shows nothing**.**


Img014

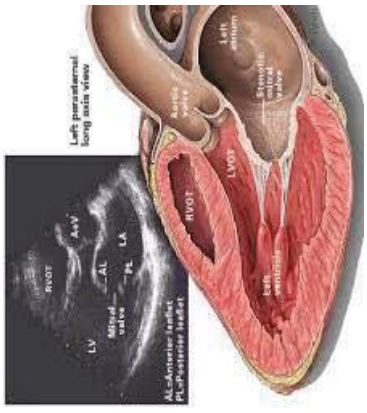
comparative : mitral valve

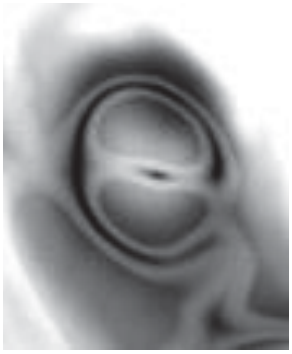

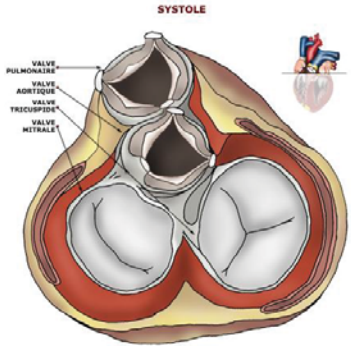

Img016 comparative image : mitral valve

In this case we see the mitral valve image is remarkable which is a real vital image as shown on the comparative diagram, whereas that of the MRI is imprecise, So the V.I.S system is a technique that allows us to get a medical diagnosis in imaging, it gives us self the auto-localization of organs pathological lesions without going through a cumbersome process of diagnostic research, the practitioner only reads the images that appear in the eye and specifically in the vitreous humor, the diagnosis is infallible and error is minimal because it will be only the readings of the images, I let you judge the images result by the VIS system affirming in my humble opinion it's the greatest discovery in the field of current medical imagery.

Patient N°2

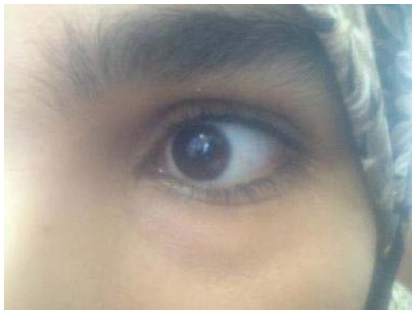

Img017 img018

Img019

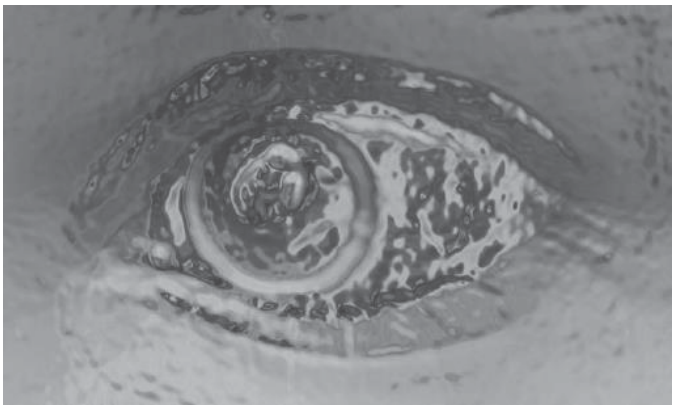

Img020

Img021 img022

Img020 : image obtained by V.I.S system we see appear clearly in central image is img022 and in the lateral pivoted right side img021. The img021 corresponds to the lung image, and image022 corresponds to the fetus.

We can say that the patient has lung disease, the patient was actually suffering from bronchitis while the 022 image corresponds to a 4-week pregnancy.

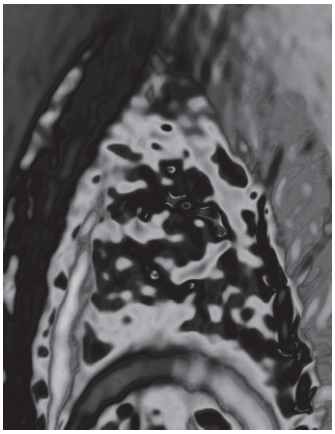

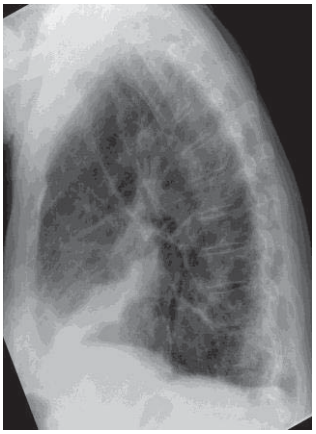

Image V.I.S System : Lung **Lung comparative image**

V.I.S System Image : The fetus

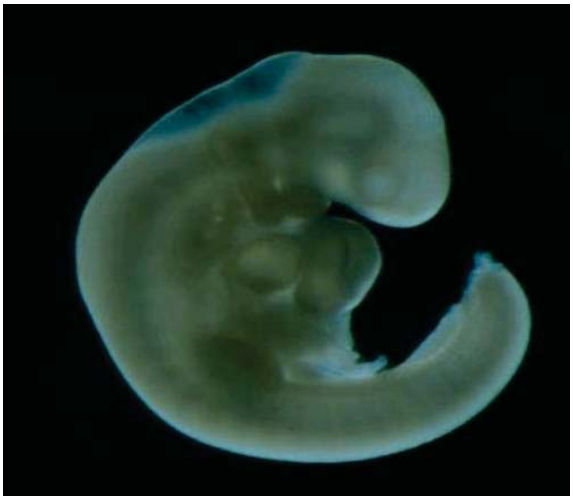

Comparative image of the fœtus (4 weeks)

QUESTION : a pregnancy is not a pathological process, why the system gives the indication of the fetus ?

ANSWER : The system considers the fetus like a foreign body, whereas the fetus DNA is different of mother DNA, So, the VIS system assumes the fetus as a foreign body and for this reason it displays image.

We took these two cases as examples to show that the V.I.S system gives us in these two cases pathologies patient by studying only the photos in the eye of the patient, it obeys specific rules, in both cases, patient had exactly the diagnosis made by the VIS confirmed by conventional diagnostic techniques.

2.7 V.I.S System Images

You will notice, and I draw your attention to the details of obtained images by V.I.S system display the internal exactness structure of the organ, at odds with scanner images or MRI shows us limited information, by multiple aggrandizement of V.I.S images, we can discover more smallest component & details of each organ, that's possible because the V.I.S System images based on a photonic binary algorithm, on the other side all obtained images by the Scanner ou MRI based on numerical binary algorithm (0,1). I have explained that clearly in my previous publications, (in WorldComp'11 & WorlComp'13) the difference between a digital binary algorithm based on (0,1) and a photonic binary algorithm based on (form, color), in the first the images are "bank data " images i.e. each images contains in itself same an infinity of images which correspond of all informations stored in the studied organ, while the obtained images by a numerical binary algorithm the image is unique.

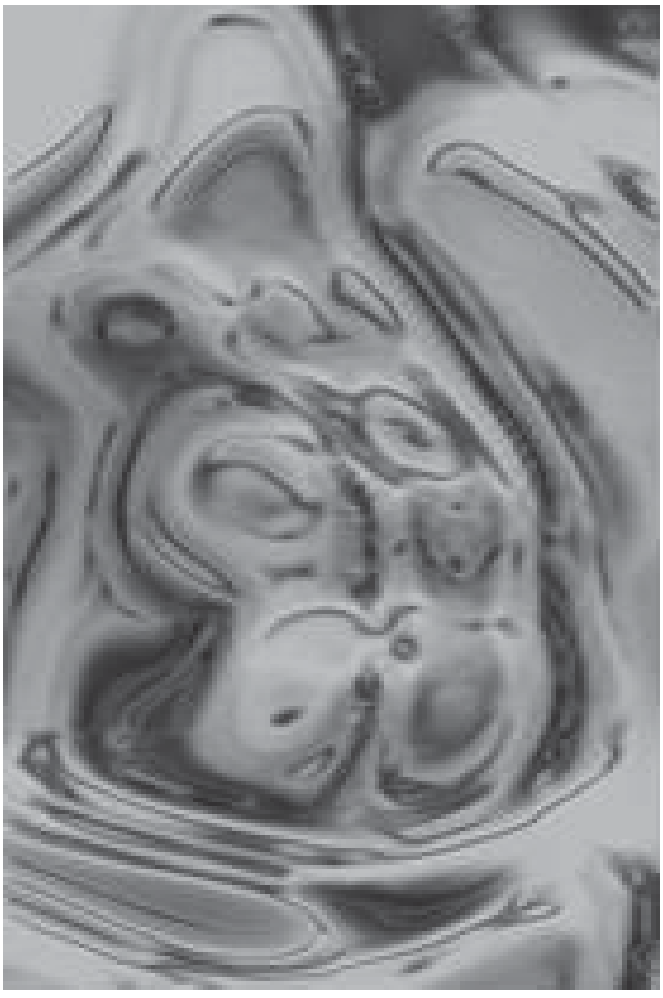

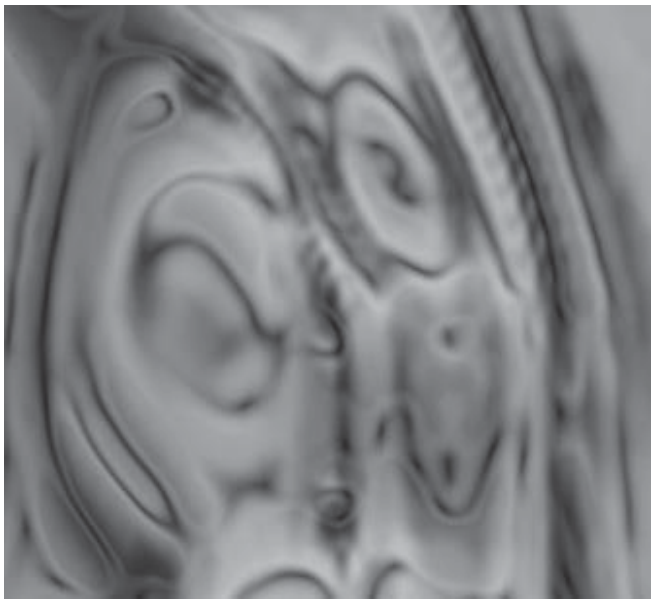

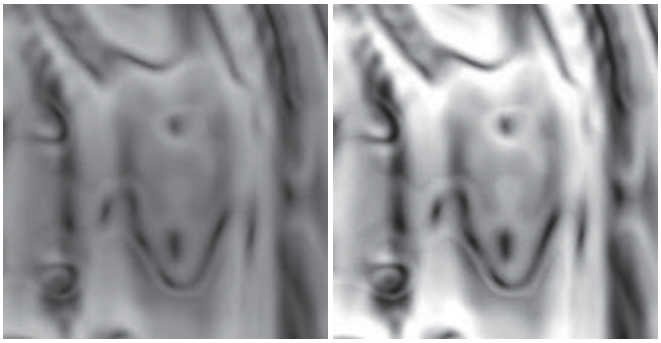

This image shows us the Heart with his internal structure detailed, but if we try to aggrandizement this image we will see the mitral valve in real image, this is impossible by the other radiological traditional techniques. I let you check and judge the quality of the images as well as their precision which is reflects and display the exact pathologies of the patient.

Judge by yourself the enlargements of MRI images.

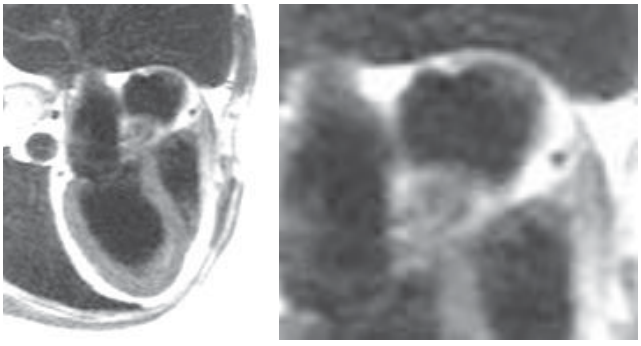

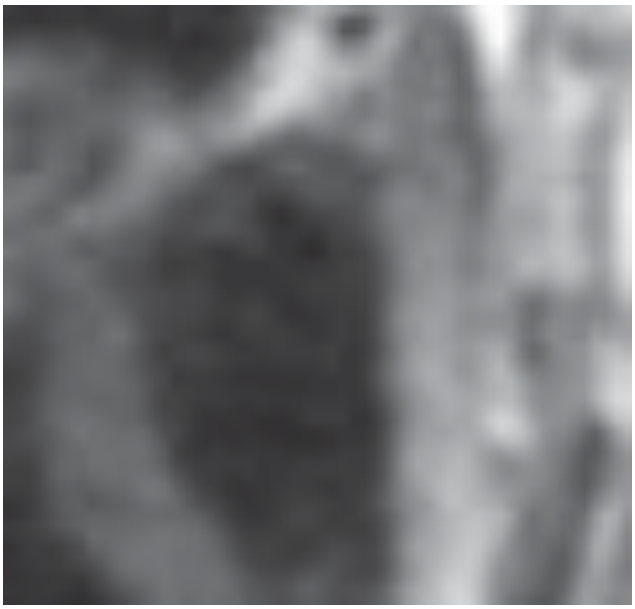

The enlargement & aggrandizement of MRI images shows us nothing more, only pixelization.

3 Conclusion

In conclusion, the V.I.S System is a revolutionary technique in medical diagnosis through imagery, highly reliable, fast and of incomparable and extraordinary quality with high precision.

The VIS can give positive diagnosis of pathologies to one or more organs without resorting to the clinical examination paraclinical, biological or radiological , in the case of VIS system the practitioner reads the displayed images in the eye, or more precisely the vitreous humor, in other side in classical case, the practitioner generally follows clinical examination more popularly known as a check-up and account of the symptoms as experienced by the patient will oriented biological or radiological examination of the body that the practitioner considers pathology.

I humbly think the VIS sytem is a revolutionary technique to put a positive diagnosis while following evolution (as the image is visible pathology exists, but the image disappears pathology has healed) I leave you judge the images obtained by the VIS, the quality of the images and their precisions while comparing to conventional radiological images.

4 References

The Comparative image, was taken from Google images Bank of MRI (heart & others organs)

SESSION

POSTER PAPERS

Chair(s)

TBA

Posture Tracking Study with Custom Wireless 3-D Gait Analysis Sensor (WGAS) and Commercial Posture Sensor

Paul E. Lie[1,2], B.T. Nukala[3], Donald Y.C. Lie[1,3], Jerry Lopez[3,4] and Tam Q. Nguyen[1,3]
[1]Texas Tech University Health Sciences Center (TTUHSC), Lubbock, TX, USA
[2]Lubbock High School, Lubbock, Texas, USA
[3]Dept. of Electrical and Computer Eng., Texas Tech University (TTU), Lubbock, TX, USA
[4]NoiseFigure Research Inc., Lubbock, TX, USA
*Corresponding Author: Donald.Lie@ttu.edu

Abstract - *Keeping good posture is important to prevent potential serious health problems. In this work, we present an original posture tracking study using a latest posture sensor Lumo Lift™, and also compare the results against measurement data obtained from our own custom wireless gait analysis sensor (WGAS). The measured posture data using both sensors indicates that: (1) even though its raw posture data is inaccessible, the Lumo Lift™ is able to track posture in real-time and provide instant feedbacks and this "coaching" appears effective for improving posture; (2) our WGAS can detect slouchy posture reliably in real-time using both its small 3-axis accelerometers and gyroscopes, which achieved good and similar tracking capability compared to the Lumo Lift™. More importantly, WGAS offers raw posture data to enable real-time posture analysis and classification.*

Keywords: *gait analysis, posture tracking, wireless gait sensor, wireless posture sensor, wireless assisted living*

1 Introduction

Poor posture can often cause unhealthy spine/joint stress and muscle strains, and if serious the anatomical characteristics of the spine can eventually change considerably over time, causing blood vessel and nerve constriction and muscle, disc, or joint problems. As an example, the Forward Head Posture (FHP) is commonly associated with poor posture during texting and computer usage, which affects many and can cause considerable neck pain [1]. When constantly in poor FHP, the skull is carried anterior to the body's center of gravity, which puts increased stress on the posterior musculature of the entire spine and in particular the cervical spine [2]. When people slouch, their heads will come forward. Slouching will also force their shoulders to come forward, and these can lead to jaw pains, headaches, and shoulder/back pains. If the spine is not aligned properly due to poor posture, it can affect the rib cage, which might even damage the heart and lungs in serious cases, and also lead to gastrointestinal issues [3]. Therefore, workplace ergonomics is now indispensable for most major companies. Maintaining good posture is a simple and effective way to keep us from those potential serious health problems. If one can utilize a wireless wearable posture sensor that effectively tracks posture continuously with real-time feedbacks to alert poor posture, it should promote good posture/health. Posture tracking and correction may be especially important for teenagers as their bone structures, organs, joints/frames are still in development; also, keeping a "stand taller, sit better" great posture using wearable posture sensors also can increase their self-esteems. Currently, Lumo Lift™ and Lumo Back™ appear to be the only fitness trackers on the market that measure the users' posture ([4]). We have used a Lumo Lift™ sensor to track posture in this study. Since one cannot extract proprietary posture tracking data from Lumo Lift™, we also built a custom 3-D wireless gait analysis sensor (WGAS) to track posture [5]. We will compare measurement of both sensors to detect slouching while standing for validation.

2 Posture Sensors Evaluated

2.1 Commercial Lumo Lift™ Sensor

Fig. 1(a) shows the size of Lumo Lift™ sensor, and it is designed for Apple i-OS. To ensure reliable sensing data, its exact placement on body is important: as in Fig. 1(b), it is recommended Lumo Lift™ should be best worn about 1" below the collarbone on the chest [4]. There is also a larger magnetic clasp to be worn underneath the clothes to hold the sensor. The user is supposed to align the sensor each time he/she repositions it or change clothes. Lumo Lift™ was designed specifically to help address upper back slouching, while it also measures steps/calories, and how much time the user in good posture daily. In the "Coaching session", it can provide discreet vibratory feedback when slouching; if the user does not want to receive vibrations anymore, he/she can switch out of the Coach mode with passive tracking [4].

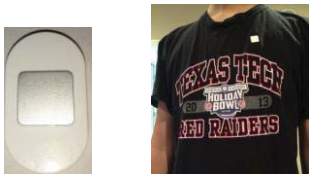

Fig. 1(a) The wireless Lumo Lift™ sensor: 1.75"x1"x0.5" at center (LxWxH); 0.48 oz; (b) how volunteer wears the Lumo Lift™ on chest for reliable posture and activity tracking.

We tested the sensor for many days, with both good and naturally slouchy posture. Some results are shown in Fig 2, where Fig. 2(a) shows the volunteer did not reach the arbitrarily set personal goals of keeping good posture for 4 hours and walks more than 10000 steps daily; so the sensor

gives a score of "Your posture was Slouchy" and "You were At Rest". However 25 days later, when the user kept good posture for 5 hours in a day, Fig. 2(d) shows a score of "Your posture was Remarkable", suggesting one may achieve better posture with coaching and feedbacks.

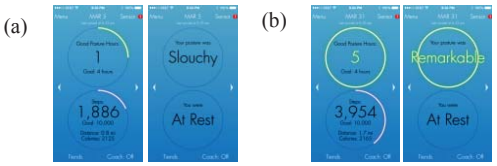

Fig. 2 Test results after wearing Lumo Lift™ for 25 days.

2.2 Wireless Gait Analysis Sensor (WGAS)

Our Texas Tech custom-designed WGAS measures 3-D human body translations and rotations during a gait pattern with the integrated MEMS sensors [5]. The WGAS consists of a 3-axis MEMS linear accelerometer IC, a single axis gyroscope IC, and a dual axis gyroscope IC. This WGAS is supported by a TI MSP430 microcontroller, and a wireless 2.4 GHz USB transceiver using the SimpliciTI™ protocol with a range of ~12 m. It is inside a 3D printed box (2.2'×1.5'×0.8'), weighing 42 g with battery (Fig. 3). The 6-axes gait data is then wirelessly transmitted to a nearby PC, where a LABVIEW™ program is used for GUI [5]. Fig. 3 shows as a user slouches, he will have a "rounded shoulder" where the sternoclavicular joints become unstable [6], and consequently the body recruits the pectoris minor muscles to stabilize the joint, which brings the shoulder forward.

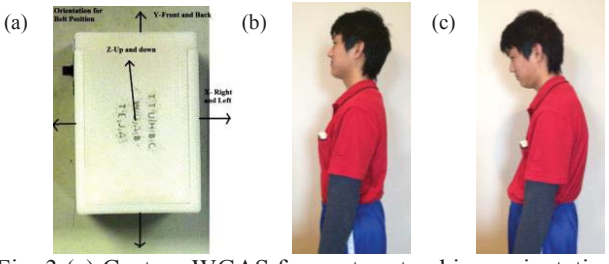

Fig. 3 (a) Custom WGAS for posture tracking: orientation; (b) Good (Left) vs. (c) Bad slouchy posture. Note WGAS is rotated 90° clockwise in the shirt pocket secured with Velcro.

The real-time voltage values from the 3-D gyroscopes (i.e., "Gyro Z", "Gyro X", and "Gyro Y" corresponding to the Z, X, and Y axes, respectively) are plotted on Fig. 4(a), and the data from the 3-D accelerometers (i.e., "ACC Z", "ACC X", and "ACC Y") is shown on Fig. 4(b). One can see the data from the accelerometers is consistent with the bad slouchy posture periods labeled in Fig. 4(b), as the output voltages of all axes of acceleration data decrease significantly. In addition, the 3-D gyroscope data is consistent and also very sensitive to the slouchy periods. For example, the "Gyro Y" data in Fig. 4(a) shows its output voltage increases during slouching, and with spikes every time the user changes from good to slouchy posture, and vice versa. The spikes are most likely due to muscle movements with slouching, and we have observed similar spikes from "Gyro Z" and "Gyro Y" data. Therefore, the raw gyroscope data will be instrumental to help the acceleration data to reliably differentiate good vs. slouchy posture, which has not been reported before using our WGAS. In the end, we need to point out that besides our current study, the use of wearable wireless sensor to continuously track human posture in real-time has been recently reported in literature [7-9]; however, unlike our studies, they all involved multiple sensors, making them somewhat impractical to wear.

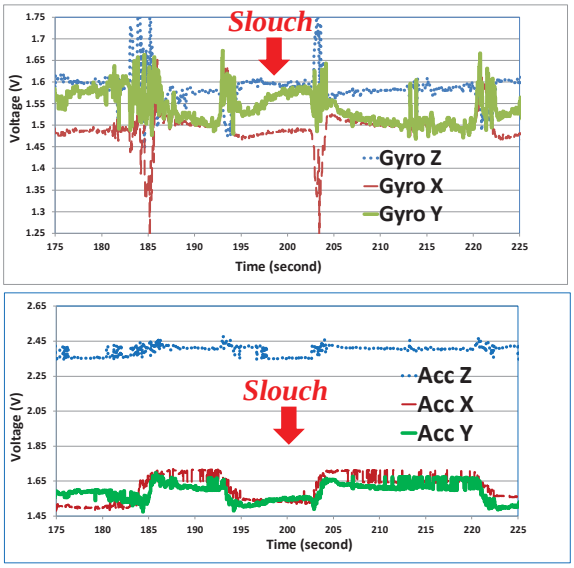

Fig. 4 Real-time measurement of good vs. slouch posture using our custom WGAS: TOP: Gyro; Bottom: Acceleration.

3 Conclusions

Our work indicates that: (1) Lumo Lift™ can track posture in real-time and provide instant feedbacks, appears effective for improving posture; (2) our WGAS can detect bad slouchy posture, and we report here for the 1st time that *both* 3-D accelerometers and gyroscopes data can be used to reliably detect slouch vs. good posture, enabling future real-time posture studies, differentiation and understanding.

4 References

[1] R. Fejer, K. Kyvik, J. Hartvigsen, European Spine Journal, vol. 15, pp. 834-848, 2006.
[2] S. Raine, L. Twomey, Australian Journal of Physiotherapy, vol. 40, pp. 25-25, 1994.
[3] http://www.fitnessmagazine.com/health/7-myths-about-bad-posture-dispelled/
[4] http://www.lumobodytech.com/
[5] B.T. Nukala *et al.*, Open Journal of Applied Biosensor, Vol. 3, pp. 29-39, 2014.
[6] https://www.youtube.com/watch?v=CXAIhJPJVgI
[7] T. Kim, S. Chen and J. Lach, Proc. IEEE Int'l Conf. on Body Sensor Networks (BSN), pp. 125-126, 2011.
[8] L. Atallah *et al.*, Proc. IEEE Int'l Conf. on Body Sensor Networks (BSN), pp. 175-180, 2009
[9] A.B. Crane *et al.*, Proc. 40th Annual Northeast Bioengineering Conference (NEBEC), pp. 1-2, 2014

Classification of alzheimer's disease using combination of each recognition method in MR scans

Saruar Alam[1], Moonsoo Kang[2], Seokjoo Shin[2], Jae-Young Pyun[1], and Goo-Rak Kwon[1]
[1]Department of Info. and comm. eng., Chosun university, Gwangju, South Korea
[2]Department of Computer eng., Chosun university, Gwangju, South Korea

Abstract - *Early accurate detection of Alzheimer disease (AD) and its prognostic stage, i.e., Mild Cognitive Impairment (MCI) is getting more and more vital. A novel approach is applied for the diagnosis of very mild (CDR- 0.5) to mild (CDR-1) Alzheimer disease patients from normal controls combining morphometric features along with MMSE (Mini Mental State Examination) score. The combined features are fed into recently proposed Self Adaptive Resource Allocation Network (SRAN) and Linear SVM classifier after getting rid of curse of dimensionality using principal component analysis.*

Keywords: Alzheimer disease, MMSE Score, and VBM features

1 Introduction

The statistical report depicts that by 2050 over 135 million people worldwide will have dementia, tripling the amount of people who have it now[1].The cost of AD patients care is likely to be yielded up to$220 billion per year in the USA and $605 billion globally. Effective early diagnosis of AD and its prodromal stage is always indispensable, can impair and prevent the disease to progress. Several noninvasive and efficient diagnosis techniques are being used like structural or functional magnetic Resonance Imaging (sMRI or fMRI), Position Emission Tomography (PET), and Single Photon Emission Computerized Tomography (SPECT). Many studies are based on automatic or semi-automatic measurement of various a priori brain Region of Interest (ROI) to compare and discriminate between healthy controls (HC), Mild Cognitive Impairment (MCI), and Alzheimer Disease (AD) patients. M. Chupin at al [2] studied that the AD patients suffer significant cerebral atrophy; several brain ROIs, especially the hippocampus and the entohinal cortex. The researchers unveiled the morphometric difference between subject groups by comparing regional volume of ROIs.P. Padillaet al [3] developed Computer aided design (CAD) tool for SPECT and PET images using NMF and SVM classifier for the diagnosis of AD patients from healthy controls yielding upto 91% accuracy with high sensitivity and specificity rates(above 90%). M. Lópezet al [4] developed tool for the diagnosis of AD patients from normal controls using PCA and Bayesian classification rules, and SPECT and PET image dataset classifying 98.3% accurately for SPECT and 88.6% accurately for PET dataset. RigelMahmood et al [5] developed an automatic detection tool using PCA and Artificial Neural Network to identify the CDR scale of entire 457 MR images in the OASIS dataset, and achieved 89.92% accuracy.

2 Material and methods

2.1 Overview of the experimental Data

All the sMRI imaging data is being taken from OASIS dataset which is an open access collection of cross sectional sMRI of 416 subjects covering the adult life span aged 18 to 96, right handed including both men and women. Longitudinal data consists of 150 subjects aged 60 to 96, right handed including men and women. The feature extraction technique is illustrated elaborately by Darya Chyzhyk et al [6]. Gender may affect morphometric differences and features. Thus 98 women MRI data has been selected to extract vbm features for training and testing strategy, 49 diagnosed patients with very mild to mild AD, and 49 non demented controls among 98 subjects.

2.2 Preprocessing and VBM Feature Extraction

The different steps of feature extraction process are depicted in Fig. 1. The averaged, registered images resampled with 1-mm isotropic image in atlas space and the bias field corrected [5] are already available in OASIS cross sectional data set. VBM toolbox has been used for preprocessing. The MRI images are manually realigned with template image, spatially normalized, segmented to get GM features. The GM segmented images are spatially smoothed with FWHM of the Gaussian kernel to 10mm isotropic prior to analyze voxel base statistics. A GM mask had been generated from the mean of GM segmentation volumes of the 98 subjects. The binary mask was built from thresholding the average GM segmented volumes consisting of all voxels with probability greater than 0.1. The statistical General Linear Model (GLM) created to analyze using two-sample t-test where the groups mapped to very mild to mild AD patients and Normal controls respectively.

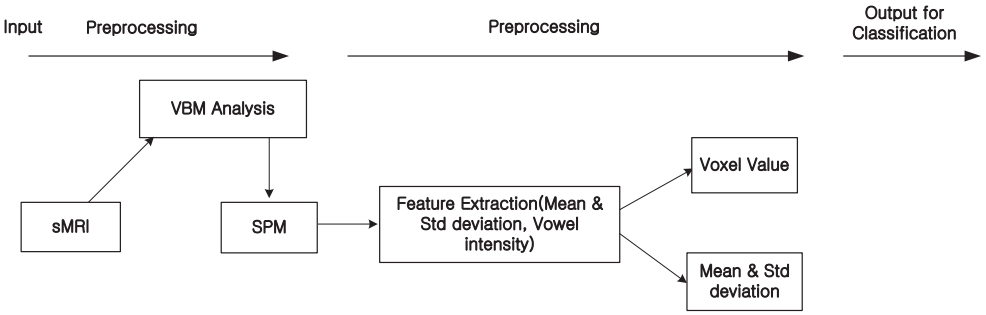

Figure 1. Block diagram of the feature extraction process from the subject s' GM segmentation volumes.

$$x_i = \{NMSE_i, vbmf_{i1}, vbmf_{i2}, \ldots\ldots\ldots vbmf_{iM}\}$$

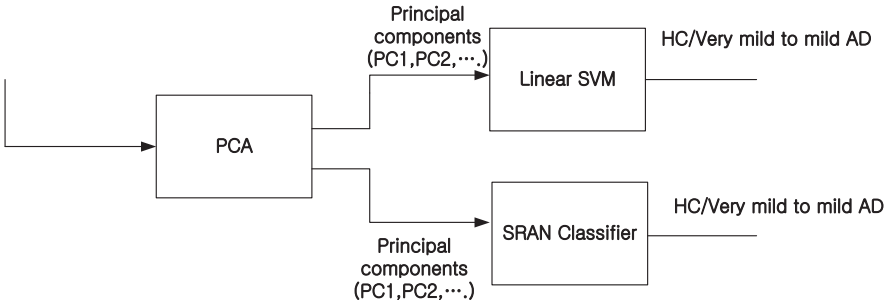

Figure 2. Schematic diagram proposed approach.

In SPM, the several functions have been set as follows: the contrast has been set to [-1 1], a right-tailed (groupN>groupAD), corrected FWE, p-value is 0.05. The feature has extracted from clusters detected by VBM for supervised learning purpose.

2.3 PCA-SRAN Classifier

A noble approach is applied combining VBM feature along, reducing the curse of dimensionality by using PCA, differentiating very mild AD to mild AD from healthy controls with SRAN classifier and linear SVM as shown in Fig. 2. Although linear SVM performs better, SRAN classifier performs efficiently for higher observations and multiclass classification problem in Table 1.

Table 1. Classification result.

Classifier	Accuracy	Sensivity	Specificity
PCA+Linear SVM	83.33%	83.33%	83.33%
PCA+ SRAN	79.17%	79.17%	79.17%

3 Conclusions

A diagnosis method for the early detection of very mild to mild AD is presented. The system was evolved by performing PCA, which drastically reduces the curse of dimensionality of the feature space. The most important components, the three principal components in terms of ability to discriminate are chosen for training and testing of Linear SVM and SRAN classifier for the diagnosis.

4 ACKNOWLEDGMENTS

This research was supported by the Brain Research Program through the National Research Foundation of Korea funded by the Ministry of Science, ICT & Future Planning (NRF-2014M3C7A1046050). Correspondence should be addressed to Prof. Goo-Rak Kwon (grkwon@chosun.ac.kr).

5 REFERENCES

[1] http://www.alzheimers.net/2013-12-11/alzheimers-global-epidemic-by-2050/.

[2] M. Chupin, E. Gerardin, R. Cuingnet, C. Boutet, L. Lemieux, S. Lehericy, H. Benali, L. Garnero, and O. Colliot, "Fully automatic hippocampus segmentation and classification in Alzheimer's disease and mild cognitive impairment applied on data from ADNI, Hippocampus," vol. 19, pp. 579-587, 2009.

[3] P. Padilla, M. Lopez,M. Gorriz , J. Ramirez, D.Salas-Gonzalez, and I. Alvarez, "NMF-SVM Based CAD Tool Applied to Functional Brain Images for the Diagnosis of Alzheimer's Disease," *IEEE Transactions on Medical Imaging*, Vol. 31, Issue 2, pp. 207 – 216, Feb. 2012.

[4] M. López, J. Ramírez, J. M. Górriz, D. Salas Gonzalez, I. Álvarez, F. Segovia, and C. G. Puntonet, "Automatic tool for Alzheimer's disease diagnosis using PCA and Bayesian classification rules, *Electronics Letters*, Vol. 45, Issue 8, pp. 389 – 391, Apr. 2009.

[5] R. Mahmood and B. Ghimire, "Automatic detection and classification of Alzheimer's Disease from MRI scans using principal component analysis and artificial neural networks," *Systems, Signals and Image Processing (IWSSIP)*, 20th IEEE International Conference, pp. 133 – 137, 2013

[6] Darya Chyzhyk and Alexandre Savio, "Feature extraction from structural MRI images based on VBM: data from OASIS database," University of the Basque Country, Internal research publication, Oct. 2010.

SESSION

LATE BREAKING PAPER: CANCER RESEARCH

Chair(s)

TBA

Developing Meta-Analysis Method for Identifying Biomarker of Gastric Cancer

Xiaoya Chen [1], Jinjun Li [1], William Yang [2], Lili Lu [1], Hongyan Jin [3], Zexiong Wei [3], Wei Gu [4], Hamid R. Arabnia [5], Mary Yang [6], and Youping Deng [1,7]

[1] Medical College of Wuhan University of Science and Technology, Wuhan, 430065, China
[2] Texas Advanced Computing Center, University of Texas at Austin,
10100 Burnet Road, Austin, Texas, 78758, U.S.A.
[3] Puren Hospital of Wuhan University of Science and Technology, Wuhan, 430081, China
[4] Department of Respiratory Medicine, Nanjing First Hospital and Third Clinical College of Nanjing Medical University, Nanjing, 210006, China
[5] Department of Computer Science, University of Georgia, Athens, Georgia, 30602, U.S.A.
[6] MidSouth Bioinformatics Center, and Joint Bioinformatics Ph.D. Program, University of Arkansas Little Rock George Washington Donaghey College of Engineering & Information Technology, and University of Arkansas for Medical Sciences, 2801 S. University Ave., Little Rock, Arkansas 72204, U.S.A.
[7] Department of Internal Medicine and Rush University Cancer Center,
Rush University Medical Center, Chicago, Illinois, 60612, U.S.A.
*Corresponding email: Youping_Deng@Rush.edu

Abstract – *Stomach cancer, also called gastric cancer is a malignant cancer developed from the lining of the stomach. More than half of the cancer was caused by bacterium Helicobacter pylori. Epsterin-Barr virus, pickled vegetables and smoking are also known causes. Since genetic variations and causes of the cancer vary significantly, it is important to develop Meta-analysis approaches to gain biological insights of the cancer. Zinc finger protein SNAI1, also known Snail, has been considered as a biomarker. Though knockout models for this gene, previous studies have shown significant reduction in caner invasiveness in breast cancer, hence the measurement of the expression of this gene has been used as a measurement of therapeutic efficacy in breast cancer. We analyzed the expression of the Snail protein in stomach cancer and developed Meta-analysis approaches to evaluate the expression of Snail protein with the malignancy of the cancer. Through the Meta-analysis model, we confirmed that increasing expression of Snail is related to carcinogenesis and metastasis of the cancer. Our study showed new findings and consistent findings in stomach cancer as others have demonstrated in various types of cancer. Our research demonstrated that developing Meta-analysis methods and computational approaches are useful for cancer studies.*

Keywords: Meta-analysis ; gastric cancer ; Snail ; biomarker ; computational and statistical analysis.

1 Introduction

Zinc finger SNAI protein, encoded by the SNAI1gene in the human genome, is a transcription factor, also known as Snail. This protein promotes the repression of the adhesion molecule E-cadherin to regulate epithelial to mesenchymal transition (EMT) during embryonic development. EMT is a process that can cause epithelial cells to loss cell polarity and cell-cell adhesion, and develop migratory and invasive behaviors. Hence EMT has known functions in wound recovery and malignant transformation of metastasis in cancer [1-3]. Snail promotes the EMT activation and suppresses the expression of E-cadherin. Reduced expression of E-cadherin, can thus promote cancer development [5]. High expression of Snail gene has been known in several types of cancers, including non-small cell lung carcinomas, ovarian cancer, urothelial carcinomas, breast cancer, and hepatocellular carcinoma [6-10]. The study of immunohistochemistry analysis suggested that Snail is also highly expressed in gastric cancer and is significantly associated with tumor progression and metastasis [11-13]. We developed a Meta-analysis method utilizing RevMan4.2 software and calculated Odds Ratio (OR) with 95% confidence interval. Heterogeneity between studies was examined using the I2 statistic. We found that upregulation of Snail is

significantly associated with the tumor progression and metastasis.

2 Material and methods

2.1 Information retrieval

Primary search using the keywords such as "snail" combined with "gastric cancer" and synonyms in Pubmed, CNKI, Weipu, and Wanfang database was performed. Automated information was gathered for the study through extended literature and database search as follows:
(1) All publications including theses and reports
(2) Results from immunohistochemistry experiments and quantitative analysis
(3) Overlapped information was automatically selected by the newest or most informative one.
(4) Information on expression of Snail.

We designed a filter to remove the redundant and/or un-reliable information as follows:
(1) Repetitive studies and reports
(2) Animal models and/or studies on cellular level only
(3) Non-peer-reviewed studies and non-verified results
(4) Any study without a control

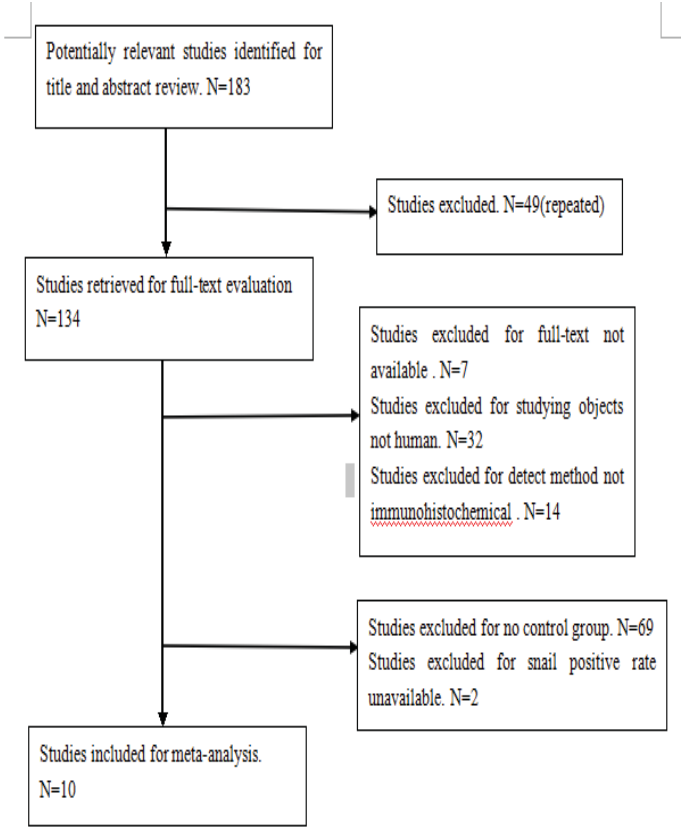

Figure 1. Method of identifying studies for Meta-analysis using the inclusion and exclusion criteria

2.2 Quality control

We performed the quality control based on the follows:
(1) In medicine and statistics, "gold standard test" uses the criteria by which scientific evidence is evaluated. We used the gold standard rules to determine the independency of the evaluation test.
(2) Whether the definition and diagnosis of the case are correct, independent, and standard
(3) Whether the blind method is used
(4) Whether quantitative data is given or calculable
(5) Whether cases and controls are selected and analyzed based on the relevant factors.
(6) Contradicting findings and results from literatures will be removed

2.3 Computational & statistical methods

We designed the Meta-analysis method by utilizing RevMan4.2 software and statistical approaches. Odds Ratio (OR) with 95% confidence interval was calculated. Heterogeneity between studies was examined using the I2 statistic [14, 15]. When I2 value was greater than 50%, we considered that the heterogeneity was significant. Fixed-effect Mantel-Haenszel model was designed as the main analysis method, when the heterogeneities were not statistically significant. Otherwise, Random-effect model was designed. Funnel plots were used to check for the potential of publication bias. All of the *P-values* in our studies were two-sided, and statistically significant difference was defined at the 0.05 level.

3 Meta-analysis and results

3.1 Literature search and study characteristics

Initial search returned for a total of 183 studies. After the procedure described above, only 10 studies were selected for the Meta-analysis. Amongst the 173 excluded studies: 49 studies were considered as repetitive studies; 32 were non-human subjects; 7 studies lack of full scientific contents; 14 studies were non-IHC studies; 69 studies did not have control groups; 2 studies were missing Snail expression data. Eventually, only 10 studies [16-25] satisfied the criteria (Fig1). Detailed characteristics of these 10 studies are summarized in Table 1. These 10 studies involved 756 gastric cancer, 346 para-carcinoma or borderline cancer, and 171 control (normal, no cancer) samples. Eight studies reported the relationship between the Snail expression and clinical outcomes including the degrees of differentiation, lymph node metastasis, Tumor-Node-Metastasis (TNM) stages, and invasion depth.

Table 1 Main characteristics of the studies selected in the Meta-analysis

First author	Year	positive rate										Quality
		cancer tissue	adjacent tissue	normal tissue	low differentiation	highly+moderate	TI+TII	TIII+TIV	superficial	deep	no metastasis	metastasis	
Yingfeng Zhu	2007	80/96	33/80	-	56/62	24/34	21/29	59/67	10/16	70/80	23/32	57/64	D
Zhifeng Tang	2010	159/189	26/54	6/32	82/100	61/89	29/46	114/143	-	-	49/73	94/116	D
Yaqin Hao	2011	41/54	22/54	9/30	20/22	21/32	-	-	4/9	17/19	5/11	16/17	D
Shengxi Wang	2011	92/112	28/79	-	66/75	26/37	-	-	15/23	77/89	29/42	63/70	E
Li Jin	2011	78/87	-	7/24	-	-	-	-	-	-	-	-	E
Lina Wang	2011	32/60	16/60	3/20	26/42	6/18	-	-	2/9	30/51	4/7	28/53	D
Wude Zhang	2012	41/48	15/48	-	32/34	9/14	23/27	18/21	22/29	19/19	24/30	7/18	E
Xiaoli Cao	2013	32/45	5/20	-	24/27	8/18	11/20	21/25	9/19	23/26	10/20	22/25	E
Qianjun Li	2013	38/65	-	0/65	-	-	-	-	-	-	-	-	D
Limin Liu	2014	57/80	24/80	-	-	-	6/14	51/66	6/15	51/65	11/24	46/56	C

3.2 Stratification analysis

Eight studies compared Snail expression in gastric cancer tissues with the adjacent tissues, including 684 gastric cancer and 475 para- carcinoma samples. The I2 values were 0% and less than 50% respectively, thus we designed Fixed-effect Mantel-Haenszel for further analysis. The overall effect was Z = 13.20, the Odds Ratio (OR) = 6.15 with 95% confidence interval 95%CI = (4.70, 8.05), and P<0.001 (Fig.2). Funnel plot analysis was performed as shown in Fig. 3.

Five of the ten studies compared the positive expression of Snail in gastric cancer and normal tissues, including 455 gastric cancer and 171 normal samples. The I2 values were 49.7% and less than 50% respectively, thus we designed Fixed-effect Mantel-Haenszel for further analysis. The overall effect was Z=10.63, OR=17, 95%CI = (10.08, 28.67), and P<0.001 (Fig.4). Funnel plot analysis was performed as shown in Fig. 5.

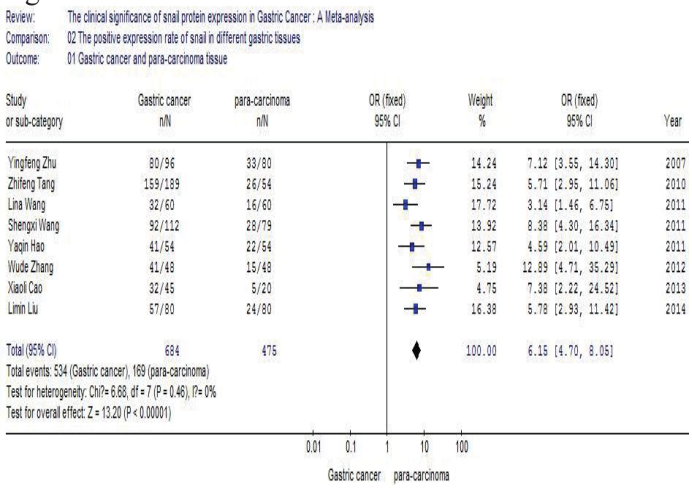

Fig.2. Meta-analysis for the expression of Snail protein in gastric cancer and para-carcinoma samples.

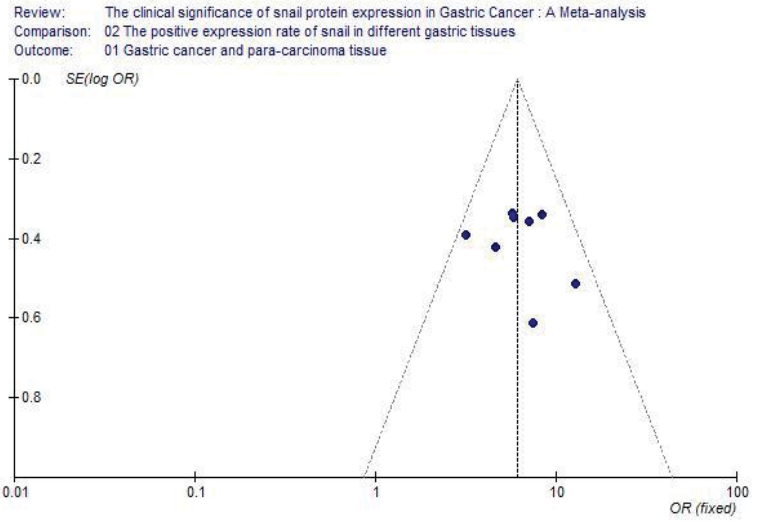

Fig.3. Funnel plot analysis for Snail expression in gastric cancer and para-carcinoma samples.

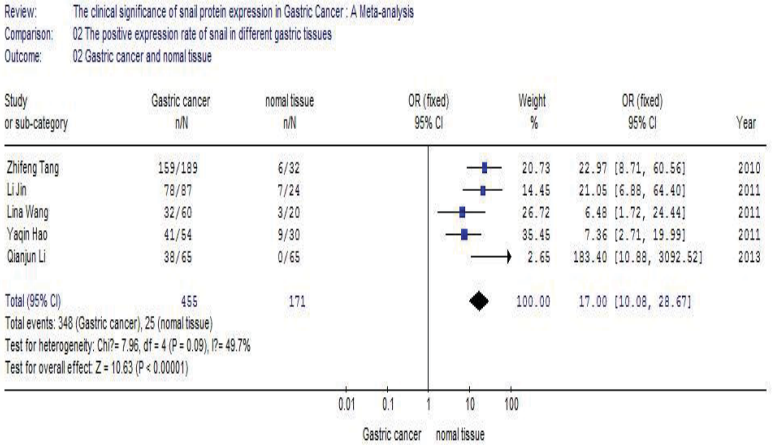

Fig.4. Meta-analysis for Snail expression in gastric cancer and normal samples.

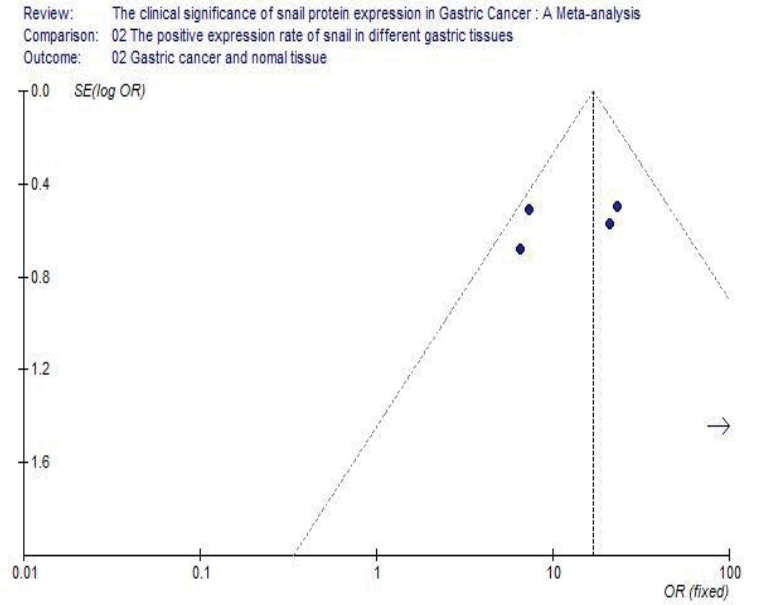

Fig.5. Funnel plot analysis for Snail expression in gastric cancer and normal samples.

3.3 Relationships between Snail expression and clinical features.

(1)Eight studies analyzed the relationship between Snail expression and lymph node metastasis. The results indicated that the I2 values were 74.4% and greater than 50%, thus we designed the Random-effect model for further analysis. The overall effect was Z=2.14, OR=0.40, 95%CI = (0.18, 0.93), and P<0.001 (Fig. 6). Funnel plot analysis was performed as shown in Fig. 7.

(2) Seven studies analyzed the relationship between Snail expression and cell differentiation. The results indicated that the I2 values were 0% and less than 50%, thus we designed Fixed-effect Mantel-Haenszel for further analysis. The overall effect was Z=5.80, OR=3.34, 95%CI = (2.22, 5.03), and P<0.001 (Fig.8). Funnel plot analysis was performed as shown in Fig. 9.

(3) Five studies analyzed the relationship between Snail expression and the TNM stages. The results showed that the I2 values were 0% and less than 50%, thus we designed Fixed-effect Mantel-Haenszel for further analysis. The overall effect was Z=4.02, OR =0.38, 95%CI = (0.23, 0.60), and P<0.001 (Fig.10). Funnel plot analysis was performed as shown in Fig. 11.

(4) Seven studies analyzed the relationship between Snail expression and invasion depth. The results showed that I2 values were 0% and less than 50%, thus we designed Fixed-effect Mantel-Haenszel for further analysis. The overall effect was Z=6.28, OR =0.18, 95%CI = (0.11, 0.31), and P<0.001 (Fig.12). Funnel plot analysis was performed as shown in Fig. 13.

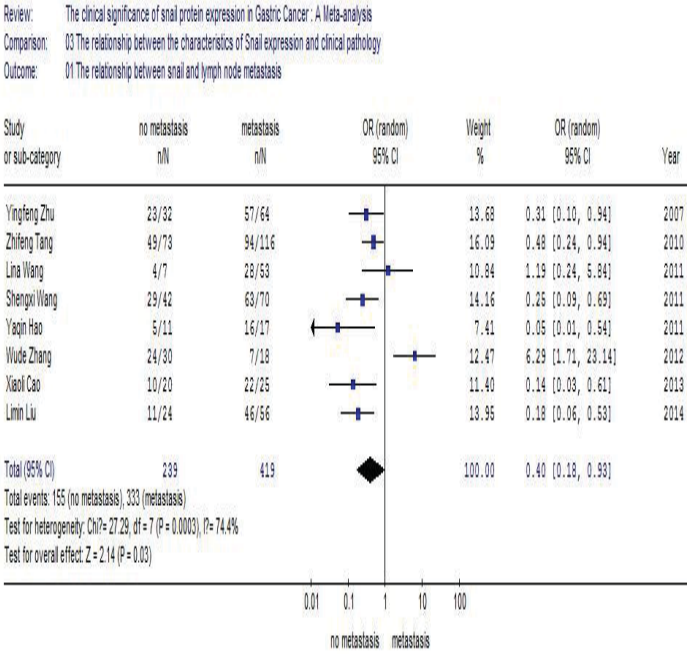

Fig.6. Meta-analysis for relationship between Snail expression and lymph node metastasis.

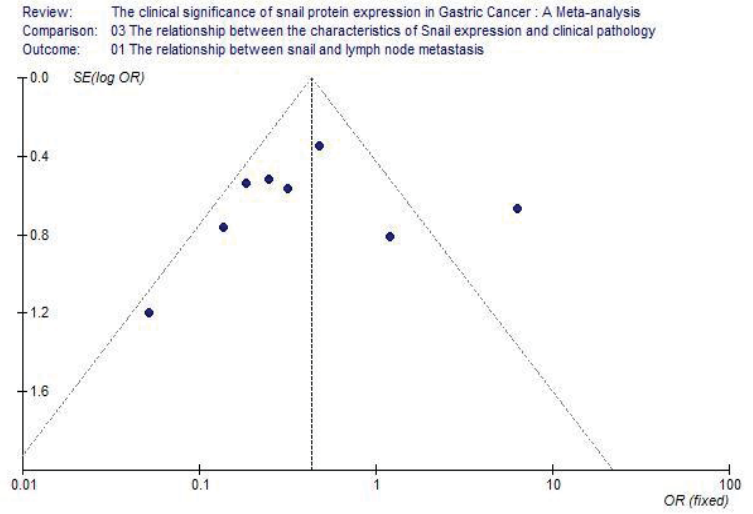

Fig.7. Funnel plot analysis for relationship between Snail expression and lymph node metastasis.

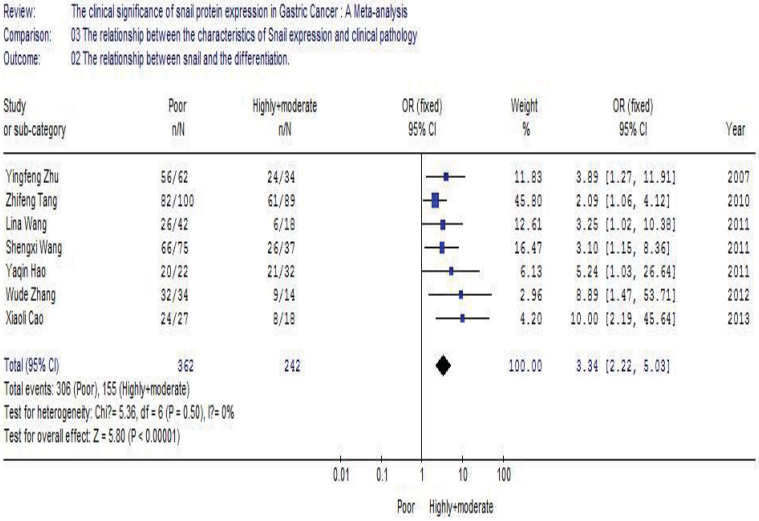

Fig. 8. Meta-analysis for relationship between Snail expression and cell differentiation.

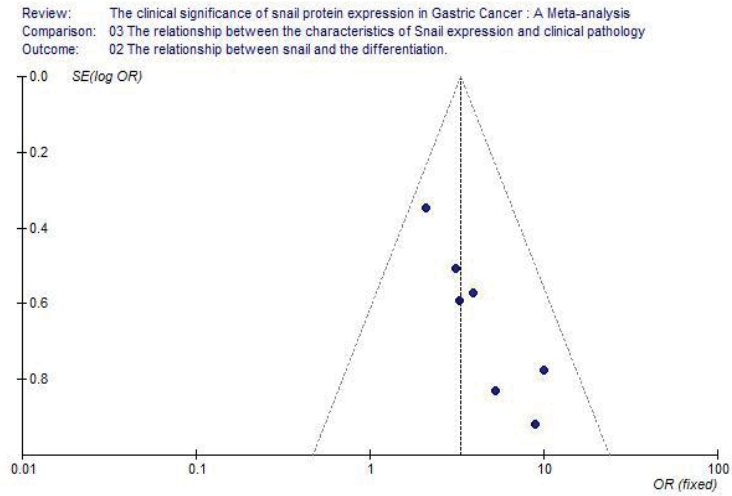

Fig.9. Funnel plot analysis for relationship between Snail expression and cell differentiation.

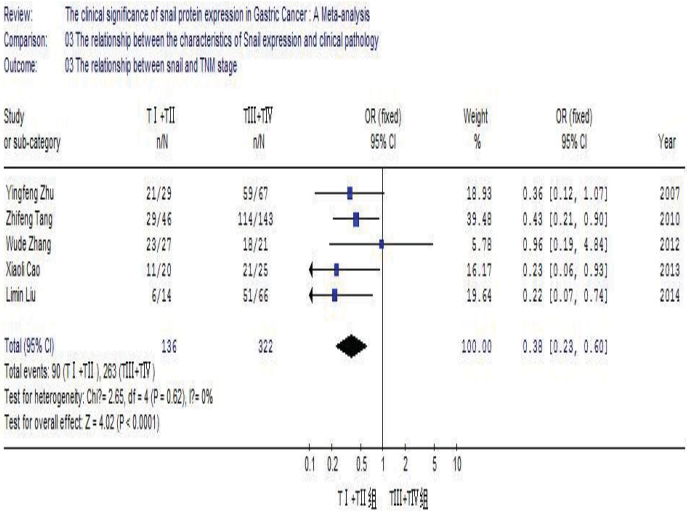

Fig.10. Meta-analysis for relationship between Snail expression and TNM stage.

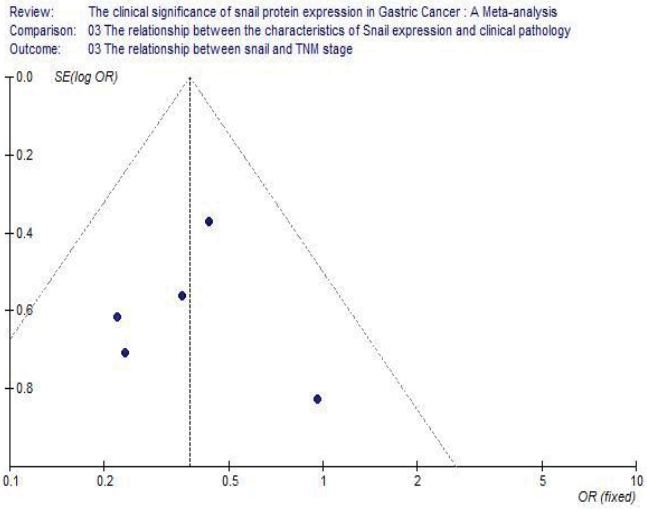

Fig.11. Funnel plot analysis for relationship between Snail expression and TNM stage.

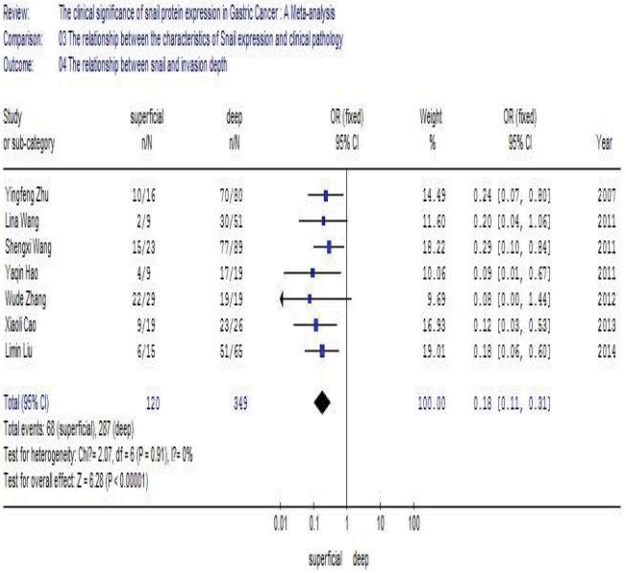

Fig.12. Meta-analysis for the relationship between Snail expression and invasion depth.

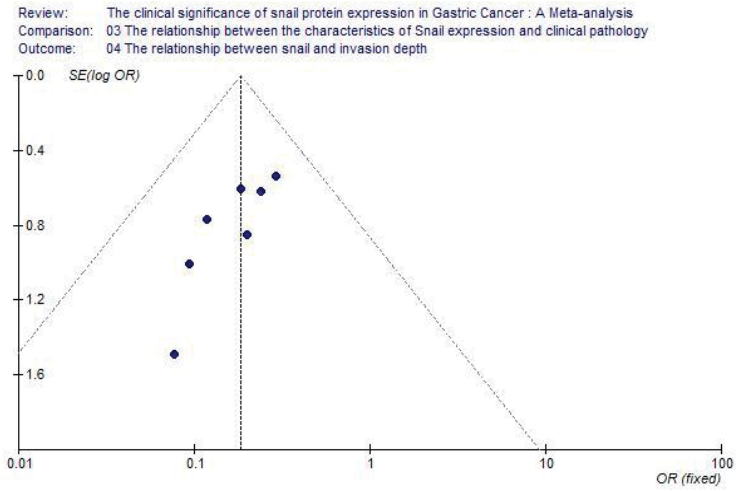

Fig.13. Funnel plot analysis for relationship between Snail expression and invasion depth.

3.4 Bias assessments

Funnel plot analysis for publication bias of these analytical studies, as shown in Figures 3, 5, 7, 9, 11, and 13, indicated low likelihoods of publication bias.

4 Discussion and Conclusion

We developed the Meta-analysis method to examine the expression of transcription factor Snail in different gastric cancer and control samples, and identified the relationship between the Snail expression and clinical features of the cancer. Our Meta-analysis combined 756 gastric cancer, 346 para-carcinoma, and 171 control samples from a cohort of ten different studies. The results indicated that Snail expression is higher in gastric cancer than those in para-carcinoma and normal samples (OR=6.15, 95%CI = 4.70, 8.05; and OR=17, 95%CI = 10.08, 28.67 respectively). Furthermore, closed correlations were observed between Snail expression and clinical characteristics, which included the lymph node metastasis, degrees of cell differentiation, Tumor-Node-Metastasis (TNM) stages, and invasion depth. The positive expression rate of Snail was higher in gastric cancer with lymphatic metastasis, as shown with OR =0.40, 95%CI = (0.18, 0.93). The up-regulation of Snail is connected with the lower differentiation degree with OR=3.34, 95%CI = (2.22, 5.03). The positive expression of Snail was higher at the late clinical stage of the cancer, OR=0.38, 95%CI = (0.23, 0.60). Moreover, it appeared that the deeper the infiltration was, the higher the expression of Snail was, as shown with OR=0.18, 95%CI = (0.11, 0.31).

Although our results from the Funnel plots indicated low likelihood of publication bias, our research now faces several further improvements:

(1) Collected papers for the Meta-analysis were either in Chinese or English. This may generate a bias because of different languages in the literatures.
(2) The majority of collected studies did not use blind methods. This might results in a measurement bias.
(3) Pathway analysis will be needed to gain deeper biological insights and determine the effective drug targets.

In the future, we will examine larger-scale samples with pathway analysis to identify drug targets, and perform double blind statistical tests. In summary, we developed Meta-analysis approaches to investigate publications with availabilities of data. It should be concluded that our Meta-analysis confirmed that Snail is highly expressed in gastric cancer, and the upregulation of Snail is significantly associated with tumor progression and metastasis. This protein can be considered as a biomarker of the cancer, and can be used for pathway analysis for identifying effective drug targets, which will be our continued research.

5 Acknowledgements

This study was partially supported by the NSF China Hubei Province grant 2011CDB236 and United States NIH R21CA164764 to Youping Deng. In addition, William Yang was supported by United States NSF Integrative Computational Education and Research Traineeship at the University of Texas at Austin Life Sciences Computing Division at Texas Advanced Computing Center.

6 References

[1] Polyak K, Weinberg RA: Transitions between epithelial and mesenchymal states: acquisition of malignant and stem cell traits[J]. Nat Rev Cancer 2009, 9: 265–273.
[2] Thompson E et al.: Carcinoma invasion & metastasis: a role epithelial-mesenchymal trans. Cancer R. 2005, 65: 5991-5.
[3] Thiery J, Sleeman J: Complex networks orchestrate epithelial-mesenchymal trans. Nat Rev Mol Cell Biol 2006,7:131-42.
[4] Sanchez-Tillo E et al.: EMT-activating transcription factors in cancer: beyond EMT and tumor invasiveness. Cellular and molecular life sciences, 2012; 69: 3429-3456.
[5] Iwatsuki M, Mimori K, Yokobori T, Ishi H, Beppu T et al. Epithelial-mesenchymal transition in cancer development and its clinical significance. Cancer Science, 2010;101:293-299.
[6] Jin H et al.: Snail is critical for tumor growth and metastasis of ovarian carcinoma. Int J Cancer, 2010, 126: 2102–2111.
[7] Yanagawa J, Walser T et al.: Snail promotes CXCR2 ligand dependent tumor progression in non-small cell lung carcinoma.Clin Cancer Res, 2009, 15: 6820–6829.
[8] Kosaka T et al.: Expression of snail in upper urinary tract urothelial carcinoma: prognostic significance and implications for tumor invasion[J]. Clin Cancer Res, 2010, 16: 5814–5823.
[9] Muenst S, Daester S, Obermann EC et al. Nuclear Expression of Snail Is an Independent Negative Prognostic Factor in Human Breast Cancer. Disease Markers, 2013, 35: 337-334
[10] Yang M et al.: Comprehensive analysis of the independent effect of twist and snail in promoting metastasis of hepatocellular carcinoma. Hepatology, 2009, 50: 1464–1474.
[11] Kim M, Lee HS et al.:. Prognostic importance of epithelial-mesenchymal transition-related protein expression in gastric carcinoma. Histopathol, 2009, 54: 442–451.
[12] Ryu HS, Park J, Kim H, Kim W, Lee HS: Combination of epithelial- mesenchymal transition and cancer stem cell-like phenotypes has independent prognostic value in gastric cancer. Hum Pathol, 2012, 43: 520–528
[13] Shin NR, Jeong EH, Choi CI et al. Overexpression of Snail is associated with lymph node metastasis and poor prognosis in patients with gastric cancer. BMC Cancer, 2012; 12: 521.
[14] Higgins J et al.: Measuring inconsistency in meta-analyses. British Medical Journal, 2003; 327(7414): 557–560.
[15] Ioannidis J et al.:. Uncertainty in heterogeneity estimates in meta-analyses. British Medical J, 2007; 335(7626): 914– 6.
[16] Zhu Y, Wu J et al, Expression of TGF-β1,Snail,E-cadherin and N-cadherin in Gastric Cancer and Its Significance[J]. Chinese Journal of Clinical Oncology. 2007, 4(6): 384-389.
[17] Tang Z, Zhou Y, et al. Expression and clinical significance of transcriptional factor Snail and adhesion factor E-eadherin in gastric cancer[J]. China Journal of Emergency Resuscitation and disaster medicine. 2010, 5(8): 696-699
[18] Hao Y et al.: Combined Detection of Shh,Glil,Snail and E-cadherin Expression in Gastric cancer and Its Significance. Chinese J. Clinical Oncology.2011,38(7): 382-385
[19] Wang S, Jiang R, Song W: The expression and significance of Snail, E-cadherin protein in gastric carcinoma. Shandong Medicine. 2011, 51(38): 48-50
[20] Wang L, et al. Expression and significance of Cox-2,Snail and E-cadherin in gastric cancer. Master degree thesis of Lanzhou University, 2011. 69
[21] Jin L et al. Expression of Snail,CK18 and Fn in gastric carcinoma and their relations with epithelial-mesenchymal transformation. J. Hebei Medical Univ., 2011,32(3): 313-316
[22] Wu De, et al.Expression and clinical significance of Snail in gastric cancer. Henan Journal Of Surgery. 2012, 18(4):26-27
[23] Cao X et al. Expression and significance of Snail and E-cadherin in Gastric cancer. Acta Acad Med Weifang, 2013, 35(1):45-48
[24] Li Q et al. Snail, a zinc-finger transcriptional factor induces gastric carcinoma invasion and metastasis via suppression of E-cadherin expression. Chin J Biomed E., 2013, 19(6): 433-7
[25] Liu L, Li J. Expression and clinical significance of E-cadherin, Snail and Twist in gastric cancer tissue and lymph node metastases. J. Clinical Medicine in Practice, 2014, 18(21): 71-74